January 2014

SYNTHESIS AND CHARACTERIZATION OF NANOSTRUCTURED MATERIALS FOR THERMOELECTRIC ENERGY CONVERSION

Haiyu Fang
Purdue University

Graduate School Form 30
(Revised 08/14)

PURDUE UNIVERSITY
GRADUATE SCHOOL
Thesis/Dissertation Acceptance

This is to certify that the thesis/dissertation prepared

By Haiyu Fang

Entitled SYNTHESIS AND CHARACTERIZATION OF NANOSTRUCTURED MATERIALS FOR THERMOELECTRIC ENERGY CONVERSION

For the degree of Doctor of Philosophy

Is approved by the final examining committee:

Yue Wu

Xiulin Ruan

John Morgan

James Caruthers

You-Yeon Won

To the best of my knowledge and as understood by the student in the Thesis/Dissertation Agreement, Publication Delay, and Certification/Disclaimer (Graduate School Form 32), this thesis/dissertation adheres to the provisions of Purdue University's "Policy on Integrity in Research" and the use of copyrighted material.

Yue Wu

Approved by Major Professor(s): _____

_____

Approved by: John Morgan 11/13/2014

Head of the Department Graduate Program Date

SYNTHESIS AND CHARACTERIZATION OF NANOSTRUCTURED MATERIALS FOR THERMOELECTRIC ENERGY CONVERSION

A Dissertation

Submitted to the Faculty

of

Purdue University

by

Haiyu Fang

In Partial Fulfillment of the

Requirements for the Degree

of

Doctor of Philosophy

December 2014

Purdue University

West Lafayette, Indiana

For my parents, 方其钦&马英

ACKNOWLEDGEMENTS

It is my honor to have so many wonderful people helping me during my graduate research. First, the thesis would not be possible without my advisor, Professor Yue Wu. I appreciate his knowledge, wisdom and patience in instructing my research as well as professional writing and presentation. Especially, his passion for innovative ideals and dedication to cutting edge research always push me to achieve higher-quality research. I am also grateful to Professor James Caruthers, Professor You-Yoen Won, Professor Xiulin Ruan and Professor John Morgan for serving on my advisory committee.

I would like to thank my group members, Dr. Genqiang Zhang, Dr. Daxin Liang, Dr. Gautam Yadav, Dr. Haoran Yang, Scott Finefrock, Kelly Rickey, Jaewon Lee, Jonatan D Albarracin. They not only provide great help in my research but also invaluable friendship that makes the everyday life during my graduate study enjoyable. It is extremely hard for me to make examples here, since their kindness is in every aspects of my graduate life. I would also like to thank the SURF undergraduate researchers working with me, Henka Darsono and Tianyue Gao. Their great assist in the research projects is very important for me.

I am also grateful to my collaborators. Dr. Je-Hyoeng Bahk, Amr Mohammed Shahat Mohammed and Professor Ali Shakouri provided great help in theoretical modeling on electron transport as well as Seebeck coefficient measurement. Tianli Feng and Professor Xiulin Ruan helped me to analyze the thermal transport in our nanocomposites. Luis Jauregui, Ting-Fung Chung and Professor Yong Chen assisted me in electrical conductivity measurement. Dr. Zhiqiang Luo and Professor Bozhi Tian from University of Chicago helped me in taking beautiful elemental mapping images with STEM.

I am also extremely lucky to have my life partner Nan Zhou and her supports pull me through the difficulties in my life. Finally, I am forever indebted to my parents, Qiqin Fang and Ying Ma, and my sister, Qin Fang, who give unconditionally love, encourage and support me throughout every step of my life.

TABLE OF CONTENTS

Page

Page

Page

LIST OF TABLES

LIST OF FIGURES

Figure Page

Figure Page

Figure Page

Figure Page

Figure Page

Figure Page

Figure Page

ABSTRACT

Fang, Haiyu. Ph.D., Purdue University, December 2014. Synthesis and Characterization of Nanostructured Materials for Thermoelectric Energy Conversion Major Professor: Yue Wu.

In 2012, more than 58% of the energy produced in the US was rejected in the form of heat. The rapid development of thermoelectric materials in the past decade has raised new hopes for the possibility of directly converting some of this waste thermal energy back to electricity. However, the large scale deployment of thermoelectric devices is still limited by the mediocre conversion efficiency. Nanostructured materials have been proved to be able to significantly improve conversion efficiency. My research is devoted to developing efficient solution phase reactions to synthesize nanostructured thermoelectric materials in an economical and scalable way. We also aim at exploring the unique applications of solution synthesized nanostructured materials, e.g. developing nanocrystal ink to coat on flexible substrates for applications in wearable thermoelectric devices.

In this thesis, the fundamentals of thermoelectrics and the benefits of nanostructured materials are first discussed in details. Afterwards, our general method to synthesize a variety of telluride nanowires and binary heterostructures with solution phase reaction is introduced in the following chapters. To demonstrate the scalability of our solution phase synthesis, a 1 liter reactor is used to synthesize tens of grams nanowires at low

temperature of 120 °C and within short time of 70 minutes. Meanwhile, we have taken advantage of the flexibility of our method and successfully synthesized different tellurides for applications at different temperature ranges, such as Bi_2Te_3 and PbTe nanowires for near room temperature (300 – 500 K) and medium temperature (500 – 800 K) applications. We even synthesized binary phase nanowire heterostructures with two tellurides in a single nanowire, such as PbTe-Bi_2Te_3 and Ag_2Te-Bi_2Te_3. To investigate the applications of nanoparticle in flexible thermoelectrics, we also developed a method to synthesize extremely stable nanocrystal ink for coating on various substrates.

Furthermore, in order to improve the thermoelectric properties of solution synthesized nanostructured materials and demonstrate their benefits for thermoelectric applications, we applied hot press to consolidate the solution synthesized nanowires and heterostructures into nanocomposites which possess extremely low thermal conductivity, leading to decent *ZT*. Especially, the binary phase nanocomposites made from heterostructures show much lower thermal conductivity than single phase bulk and even nanocomposite. To further improve the thermoelectric performance, we also applied doping to tune the carrier concentration of our materials to gain more thermoelectric performance enhancement. For example, Se was used to dope Bi_2Te_3 nanocomposites, which leads to 60% of power factor enhancement.

In addition, nanocrystal thin films were fabricated with stable nanocrystal ink on different substrates, even flexible ones. Particularly, the effects of size and iodine doping

concentration on the thermoelectric properties on the PbTe nanocrystal thin films are investigated to enhance the understanding of using nanocrystals for thermoelectrics.

CHAPTER 1. INTRODUCTION

In the past 50 years, the human society has been deeply transformed by the fast development of technology. From the first computer that occupied a whole building to personal smart devices in everybody's hands, the fabrication of transistors has advanced enormously and millions of nanoscale transistors can now be integrated on a single centimeter chip. With the benefits brought by the fast development of technology is greater need for energy. In 2011, the U.S. has consumed 97.3 Quads of energy (Figure 1.2) that is over 2 times more than the energy consumed in 1960 (43.9 Quads; Figure 1.1). On the other hand, reservation of fossil fuel, as the dominate source of energy (Figure 1.1 and 1.2), decreases drastically and could be used up in the foreseeable future. Another issue is that burning of fossil fuel produces large amount of carbon dioxide which is thought to be responsible for global warming. Considering the sustainability development of human society, researchers have been pursuing alternative energy sources, such as geothermal, solar, wind and so on, which has contributed around 2 % of the total energy produced in 2011 (Figure 1.2). However, one thing people tend to overlook is the energy rejected each year. Comparing the percentages of rejected energy in 1960 (43.5 %; Figure 1.1) and 2011 (57.1 %; Figure 1.2), surprisingly we even waste more energy than we did 50 years ago although our technology has been through great transformation. Nowadays, as energy becomes more expensive, researchers begin to investigate methods to recover

waste heat that is the majority of the rejected energy. The majority came from power plants, transportation, and manufacturing industries. Most of this waste heat is low-grade, 40 °C to 200 °C, a level that is generally considered economically infeasible for recovering at a high efficiency. In addition, the theoretical Carnot efficiency is quite low from about 5% to 35%. The practical efficiency may range from 2 to 15%. Even with 2% efficiency it may be worthwhile to recover a small fraction of this huge amount of waste energy. Thermoelectric (TE) devices, which can convert thermal energy to electricity, are considered a promising way to reduce energy waste in various areas [Mahan et al, 1997; Bell et al, 2008; Leonov et al, 2009], such as power plants and automobiles [Yang et al, 2006; Kumar et al, 2013]. At the same time, TE devices can be solid-state coolers by pumping heat from cold to hot. They could therefore be used in many applications, such as laser diode cooling, electronic chip cooling and portable coolers; a combined potential market of billions of dollars is expected [DiSalvo, 1999]. Furthermore, compared to traditional heat engines, TE devices use electrons/holes as the “working fluid” so they are more mechanically reliable [DiSalvo, 1999].

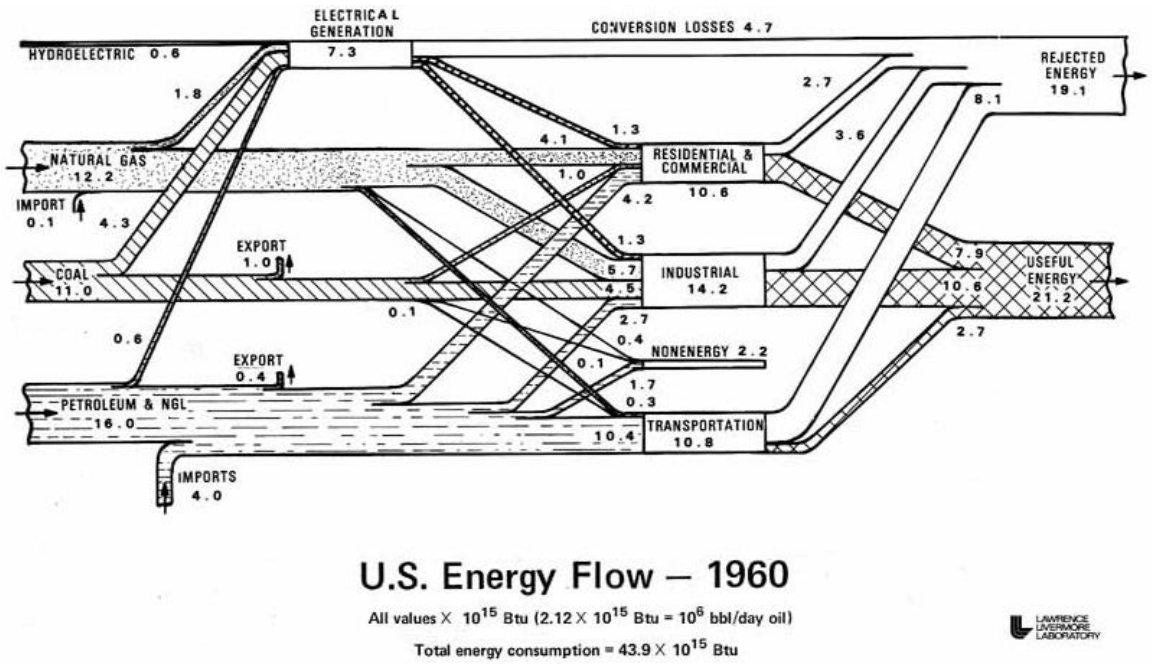

Figure 1.1. Energy flow chart in the United States for the year 1960. [Lawrence Livermore National Laboratory, 1960]

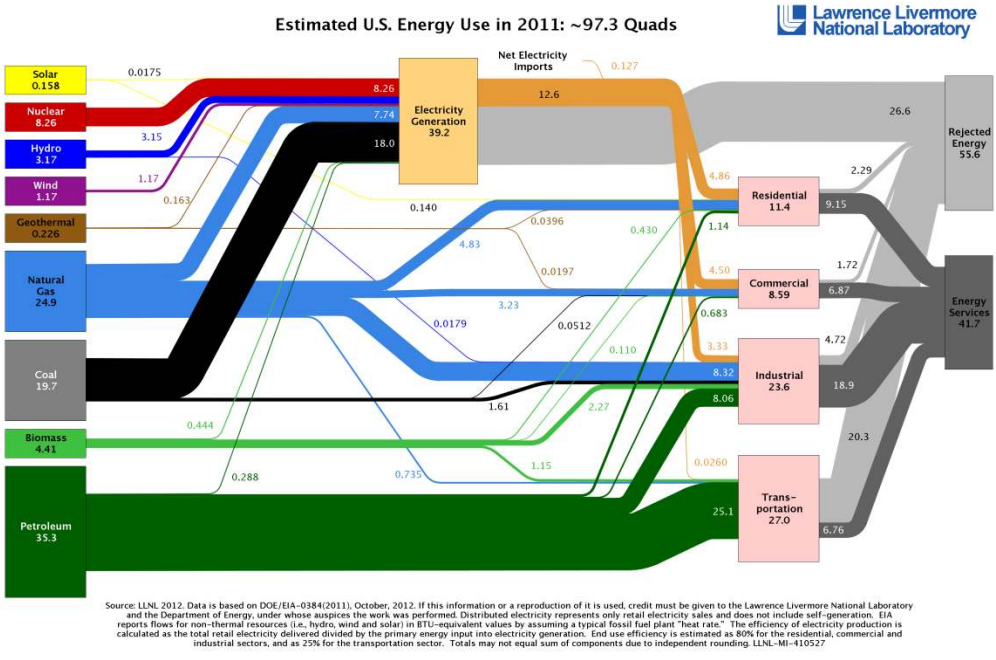

Figure 1.2. Energy flow chart in the United States for the year 2011. [Lawrence Livermore National Laboratory, 2011]

1.1 Thermoelectric Coefficients

Thermoelectrics is based on a series of physical effects discovered in 19th century [Rowe et al, 1983a]. In 1821, Seebeck first reported an experiment result in which a magnetic needle in center of closed circuit composed of two different conductors was deflected when one junction of two different conductors was heated, which is called Seebeck effect. Later on, researchers realized that an electric current was generated because of temperature difference and magnetic field from the circuit current deflected the magnetic needle. Twelve years later, Peltier discovered the complementary effect in which one junction of two different conductors was cooled when an electric current flew in the circuit, which is later called Peltier effect. In 1838, Lenz even demonstrated freezing water and melting ice by changing current direction with Peltier effect. In 1851, Thomson (Lord Kelvin) predicted the Thomson effect in which heating or cooling happens when a current flows through a single homogeneous conductor with a temperature gradient, which was later discovered by experiment.

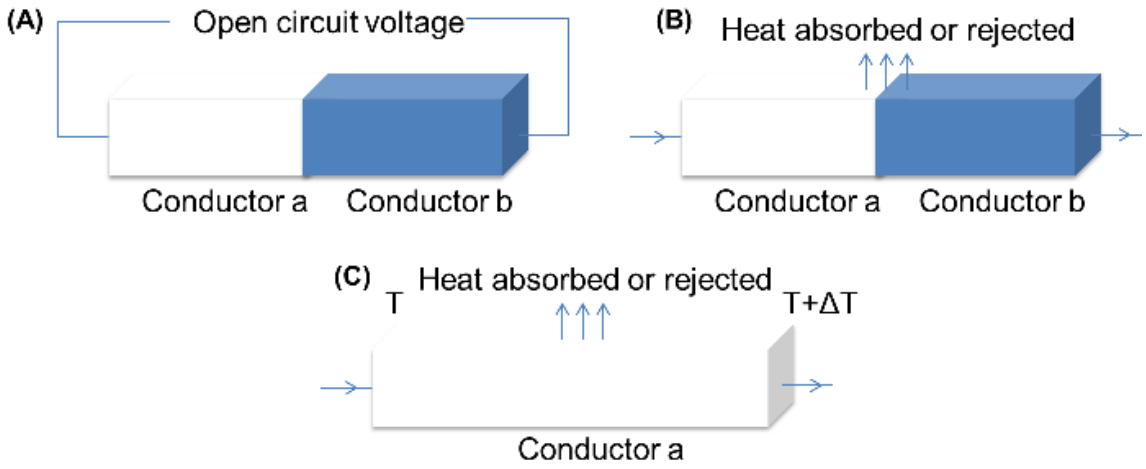

Figure 1.3. A schematic demonstration of (A) Seebeck effect, (B) Peltier effect and (C) Thomson effect.

The physical significance of thermoelectric effects is to connect heat to electricity. In a conductor without temperature gradient, charge carriers distribute uniformly and no voltage is built. When there is a temperature gradient along the conductor, the charge carriers at hot side have more kinetic energy and diffuse to cold side, which builds up a voltage. In the Seebeck effect (Figure 1.3A), two different conductors form a junction that is heated (T_1) and an open circuit voltage (V) can be tested at other sides of both conductors that are assumed to be at the same temperature (T_2). The ratio $S_{ab} = V/(T_1 - T_2)$ is defined as Seebeck coefficient that is a constant for small temperature difference but varies with different materials and temperatures [Rowe et al, 1983a]. Researchers often use micro volt per kelvin (μV/K) as the unit of Seebeck coefficient. In the Peltier effect (Figure 1.3B), when there is a current I flowing through the junction of conductor a and b where heat is absorbed or rejected. The Peltier

coefficient is defined as the ratio of the rate of heat absorption or rejection to the current *I* ($\pi_{ab} = \dot{Q} / I$) and measured in watts per Ampere (W/A) or volts (V) (7). The charge carriers in conductor a and b have different potential energy, so they need to exchange energy with environment to keep conservation of energy when going through the junctions, which leads to the Peltier cooling or heating. In the Thomson effect (Figure 1.3C), when a current *I* flowing through conductor a with a temperature gradient, heat is absorbed or rejected and the rate of heat absorption or rejection ($\dot{Q}$) is calculated by $\dot{Q} = \beta I \Delta T$ where β is defined as the Thomson coefficient [Rowe et al, 1983a]. In fact, the physical origin of the Thomson effect is the same as the Peltier effect except that herein temperature gradient gives charge carriers different potential energy along the conductor. Not only Thomson predicted the Thomson effect, he also unified the three thermoelectric effects with the kelvin relationships [Rowe et al, 1983a]:

$$S_{ab} = \frac{\pi_{ab}}{T} \quad \text{.....(1.1)}$$

and $$\frac{dS_{ab}}{dT} = \frac{\beta_a - \beta_b}{T} \quad \text{.....(1.2)}$$

As discussed above, the Seebeck and Peltier coefficients are defined in a two conductors system with junctions. Herein, the kelvin relationships (Equation 1.2) actually help deriving the definition of the Seebeck coefficient of a single material.

$$S = \int_0^T \frac{\beta}{T} dT \quad \text{.....(1.3)}$$

The previous Seebeck coefficient defined for junctions can be calculated by the difference of the Seebeck coefficient of each conductors: $S_{ab} = S_a - S_b$. The sign of the

Seebeck coefficient is positive for hole transport and negative for electron transport. The derivations in this chapter are not unique; they have been taken from previous work.

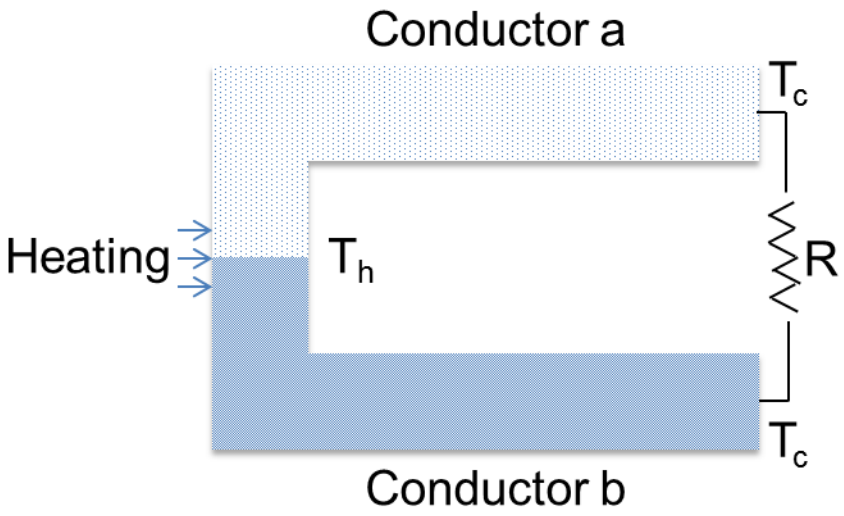

Figure 1.4. A scheme of a real working thermoelectric device for the calculation of power generation efficiency.

1.2 Power Generation Efficiency and Thermoelectric Figure of Merit

As discussed above, thermoelectric device can directly convert heat into electricity, so the next natural and important question is how to evaluate the power generation efficiency of a thermoelectric device. Figure 1.4 is a scheme of a real working thermoelectric device. Two different conductors a and b are connected with one junction heated (T_h) and the other junction left cool (T_c) is connected with a load (R). One approximation and one assumption need to be made before calculating the power generation efficiency of the thermoelectric device. First, the approximation is that the Thomson effect is neglected. Second, the assumption is that half of the Joule heating in the device is conducted back

and reused by the hot junction. An evaluation of error by the approximations and more accurate calculation can be found in reference [Borrego et al, 1958]. The current (I) can be calculated by

$$I = \frac{V}{r_d + R} = \frac{V}{r_d(M+1)} = \frac{S_{ab}(T_h - T_c)}{r_d(M+1)} \quad \text{.....(1.4)}$$

where r_d is device resistivity, V is Seebeck voltage, M is the ratio of R to r_d. So the power output can be calculated by

$$P = I^2 R = \frac{S_{ab}^2 M (T_h - T_c)^2}{r_d (M+1)^2} \quad \text{.....(1.5)}$$

The heat flows into the junction in two ways: external heating and half of the Joule heating. Meanwhile, the heat is removed in two ways: Peltier cooling and heat conduction in the thermoelectric device. In the steady state, the heat flowing into the junction should be equal to the heat removed, so we have

$$Q_{in} + \tfrac{1}{2} Q_J = Q_P + Q_C \quad \text{.....(1.6)}$$

where Q_{in} is external heating, Q_J is device Joule heating, Q_P and Q_C are Peltier cooling and heating conduction. Q_J is calculated by

$$Q_J = I^2 r_D = \frac{S_{ab}^2}{r_D (M+1)^2} (T_h - T_c)^2 \quad \text{.....(1.7)}$$

Q_P is calculated by

$$Q_P = \pi_{ab} I = S_{ab} T_h I = \frac{S_{ab}^2 T_h (T_h - T_c)}{r_D (M+1)} \quad \text{.....(1.8)}$$

Q_C is calculated by

$$Q_C = \kappa_D (T_h - T_c) \quad \text{.....(1.9)}$$

In equation 1.9, κ_D is thermal conductance of the device. In order to make to make the Equation 1.7-1.9 more concise, a term is defined and later called figure of merit by thermoelectric community.

$$Z_D = \frac{S_{ab}^2}{r_D \kappa_D} \quad \text{.....(1.10)}$$

Therefore, by putting Equation 1.7-1.10 into equation 1.6, the expression of Q_{in} can be obtained

$$Q_{in} = Q_P + Q_C - \tfrac{1}{2} Q_J = Z_D \frac{\kappa_D T_h (T_h - T_c)}{(M+1)} + \kappa_D (T_h - T_c) - Z_D \frac{\kappa_D (T_h - T_c)^2}{2(M+1)^2} \quad \text{.....(1.12)}$$

And by putting Equation 1.10 to 1.5, the expression of P can be obtained

$$P = Z_D \frac{\kappa_D M}{(M+1)^2} (T_h - T_c)^2 \quad \text{.....(1.13)}$$

So the power generation efficiency can be calculated from Equation 1.12 and 1.13

$$\eta = \frac{P}{Q_{in}} = \frac{T_h - T_c}{T_h} \frac{M}{(M+1) - \frac{T_h - T_c}{2T_h} + (M+1)^2 \frac{1}{T_h Z_D}} \quad \text{.....(1.14)}$$

Now the maximum power generation efficiency can be obtained by differentiating the Equation 1.14 in respect to M and setting the result to zero.

$$M_{\max} = \frac{R_{\max}}{r_D} = \sqrt{1 + Z_D T_{Ave}} \quad \text{.....(1.15)}$$

Here T_{Ave} is the average temperature of T_h and T_c. Finally, the maximum power generation efficiency is calculated by putting Equation 1.15 to 1.14.

$$\eta_{\max} = \frac{T_h - T_c}{T_h} \frac{\sqrt{1 + Z_D T_{Ave}} - 1}{\sqrt{1 + Z_D T_{Ave}} + T_c / T_h} \quad \text{.....(1.16)}$$

Now we reach the final expression of maximum power generation. A few important points can be summarized. First, in order to obtain the maximum power output, the resistivity of the load has to be optimized in respect to the thermoelectric device internal resistivity, which gives a guideline for thermoelectric device design. Second, by observing Equation 1.16, the device efficiency is determined by two part: Carnot efficiency ($\frac{T_h - T_c}{T_h}$) and $\frac{\sqrt{1+Z_D T_{Ave}}-1}{\sqrt{1+Z_D T_{Ave}}+T_c/T_h}$. Carnot efficiency which depends on the temperature of hot and cold ends that is usually fixed when deploying thermoelectric devices in certain application conditions, so the practical way of improving the efficiency is to increase Z_D (Equation 1.10) that has been defined as figure of merit which can be rewritten as if the geometries of conductor a and b are matched

$$Z_D = \frac{S_{ab}^2}{\left[\left(\frac{\kappa_a}{\sigma_a}\right)^{\frac{1}{2}} + \left(\frac{\kappa_b}{\sigma_b}\right)^{\frac{1}{2}}\right]^2} \quad \text{.....(1.17)}$$

where κ_a and κ_b are the thermal conductivity and σ_a and σ_b are electrical conductivity. In practical application, in condition that the two arms of the junctions have similar material properties, the concept of the figure of merit for a single material can defined as [Rowe et al, 1983b]

$$Z = \frac{S^2 \sigma}{\kappa} \quad \text{.....(1.18)}$$

Basically, the value of Z is determined by three internal material properties: Seebeck coefficient (S), electrical conductivity (σ) and thermal conductivity (κ), so it evaluates

the performance of a material in thermoelectric application and higher value of *Z* is what researchers try to achieve in this field.

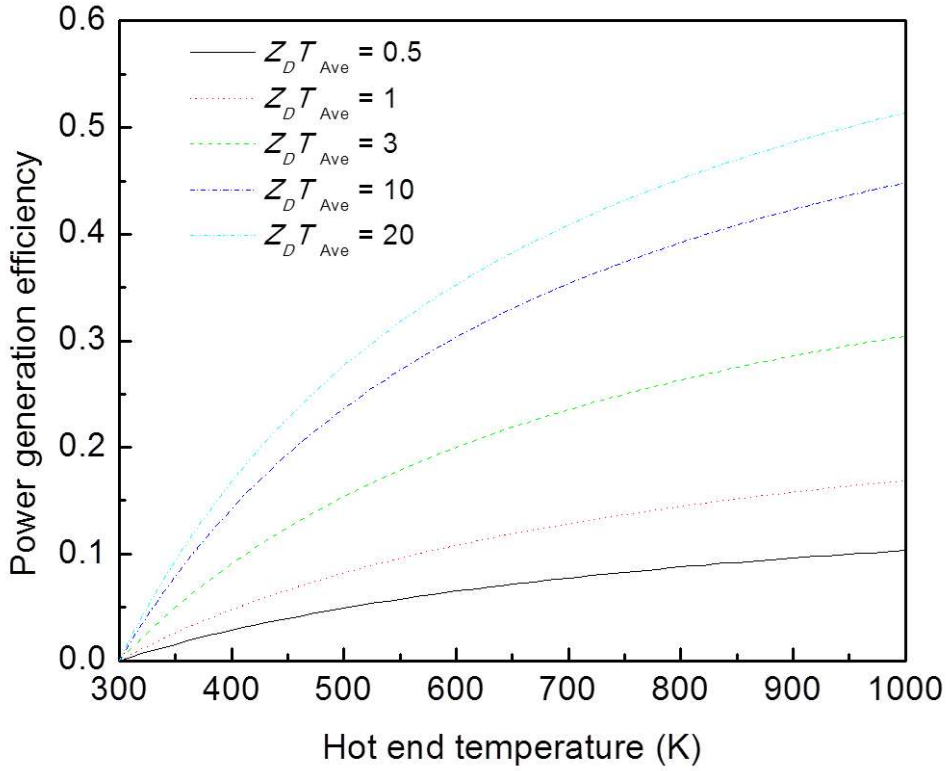

Figure 1.5. The power generation efficiency at cold end temperature of 300 K and variable hot end temperature given different values of $Z_D T_{Ave}$.

Researchers usually use the dimensionless figure of merit: *ZT* that leads to a more direct calculation of efficiency. Assuming the cold end temperature is 300 K, power generation efficiency can be plotted out with the hot end temperature at different *ZT* values (Figure 1.5). The thermodynamic limit of power generation efficiency is the Carnot efficiency, which is to say that infinite large *ZT* is ultimately an ideal Carnot engine. As hot end temperature or temperature difference increases, better efficiency can be reached. More

importantly, the figure displays that better *ZT* will lead to larger power generation efficiency at the same hot end temperature. Of course, Figure 1.5 only shows the ideal relation between *ZT* and power generation efficiency. In real application scenario, other factors need to be taken into consideration, such as thermal radiation, heat conduction loss between device and heat source, decay for radioactive heat source, so the actual efficiency could be smaller than the Figure 1.5. Optimizing the thermoelectric device design, such as thermal interface between device and heat source and area to length ratio of conduction legs, is also a very important task in thermoelectrics [Penn et al, 1974].

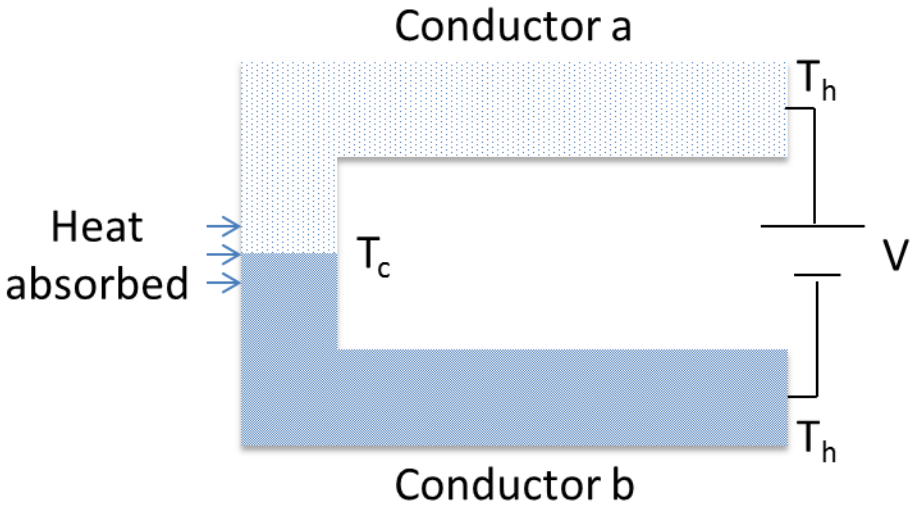

Figure 1.6. A scheme of a real working thermoelectric device for the calculation of coefficient of performance.

1.3 Refrigeration and the Coefficient of Performance

Thermoelectric device can be also used as refrigerator by applying electricity. Figure 1.6 is a scheme of a thermoelectric device with external electrical power. Now the

thermoelectric device behaves like a pump that carries heat from cold (T_c) to hot end (T_h). For the junction of a and b, heat is removed by Peltier effect but brought by Joule heating and heat conduction. As in Chapter 1.2, half of the Joule heat is absorbed by the junction. Therefore, the overall heat removed from the junction can be written as

$$Q_{ab} = S_{ab}T_cI - \tfrac{1}{2}I^2r_D - \kappa_{ab}(T_h - T_c) \quad \text{.....(1.19)}$$

In the calculation, the Kelvin relation is used to get heat removed by Peltier effect. By differentiating Equation 1.19, the current that gives maximum heat pumping can obtained.

$$I'_{\max} = \frac{S_{ab}T_c}{r_D} \quad \text{.....(1.20)}$$

which gives a coefficient of performance

$$\phi' = \frac{\frac{1}{2}Z_DT_c^2 - (T_h - T_c)}{Z_DT_hT_c} \quad \text{.....(1.21)}$$

Therefore, the maximum possible temperature difference or lowest temperature of cold end is given by

$$T_c = \frac{\sqrt{1 + 2Z_DT_h} - 1}{Z_D} \quad \text{.....(1.22)}$$

In a steady state, the external potential should balance the Seebeck voltage and device electrical resistivity, so the power input can be calculated as

$$P = S_{ab}\Delta TI + I^2R \quad \text{.....(1.23)}$$

The coefficient of performance is defined as heat removed divided by the power input.

$$\phi = \frac{S_{ab}T_cI - \tfrac{1}{2}I^2r_D - \kappa_{ab}(T_h - T_c)}{S_{ab}\Delta TI + I^2R} \quad \text{.....(1.24)}$$

The coefficient of performance depends on the current, so the maximum can be obtained by differentiating Equation 1.24 in respect to the current.

$$I''_{\max} = \frac{S_{ab}\Delta T}{r_D\sqrt{1+Z_D T_{Ave}}-1} \quad \text{.....(1.25)}$$

By putting Equation 1.25 to 1.24, the maximum coefficient of performance can be written as

$$\phi_{\max} = \frac{T_c\left[\sqrt{1+Z_D T_{Ave}} - T_h/T_c\right]}{(T_h - T_c)\left[\sqrt{1+Z_D T_{Ave}}+1\right]} \quad \text{.....(1.26)}$$

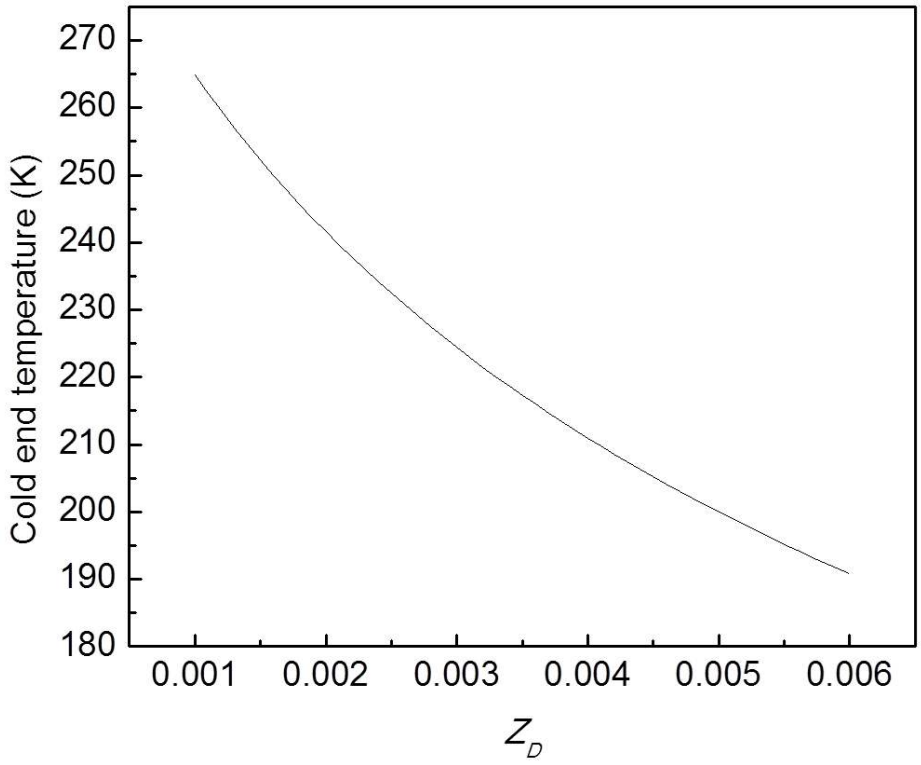

Figure 1.7. The lowest temperature that can be achieved through Peltier cooling against Z_D at a hot end temperature of 300 K.

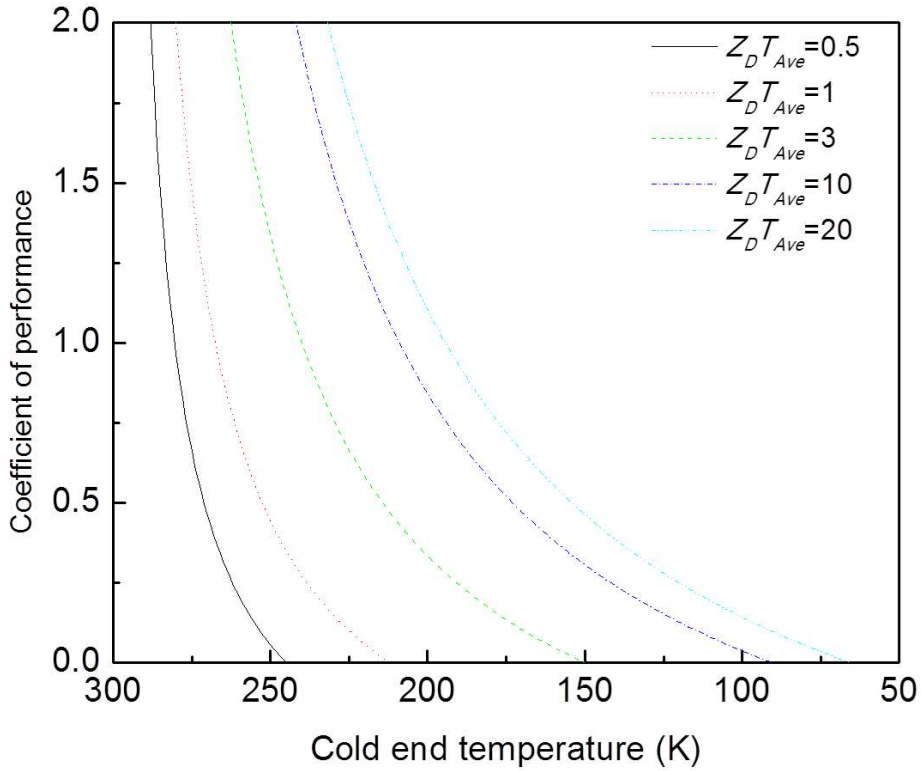

Figure 1.8. The maximum coefficient of performance against cold end temperature at different Z_DT_{Ave} given a hot end temperature of 300 K.

According to Equation 1.22, the lowest temperature that can be achieved through Peltier cooling is plotted out against Z_D assuming hot end temperature is 300 K in Figure 1.7 that shows that higher Z_D can lead to lower junction temperature. In real application, every thermoelectric device has a lowest temperature that can be achieved once the hot end temperature is fixed. Under the same assumption, the maximum coefficient of performance is plotted out against cold end temperature at different Z_DT_{Ave} in Figure 1.8 that shows that higher Z_DT_{Ave} results in larger coefficient of performance but as lower cold end temperature is achieved, lower coefficient of performance is expected. Of course,

as discussed in Chapter 1.2, Figure 1.7 and 1.8 only represent the theoretical situation and actual devices can hardly reach such performance.

1.4 Seebeck Coefficient and Electrical Conductivity

As introduced in previous sections, *ZT* is defined by three intrinsic properties of materials: Seebeck coefficient, electrical and thermal conductivity. If each property is regarded individually, it is safe to say that the variation of Seebeck coefficient is at the order of around 10^2, electric conductivity is about 10^5 and thermal conductivity is around 10^3, thus the variation of ZT could be over an order of 10^{10}, which implies amazingly high *ZT*. However, in fact the three properties of certain material are correlated and determined by some common fundamental parameters, which is to say that they cannot be tuned independently. Here I will discuss *ZT* in the perspective of electron and phonon transport and try to find the physics that governs the optimization of *ZT*.

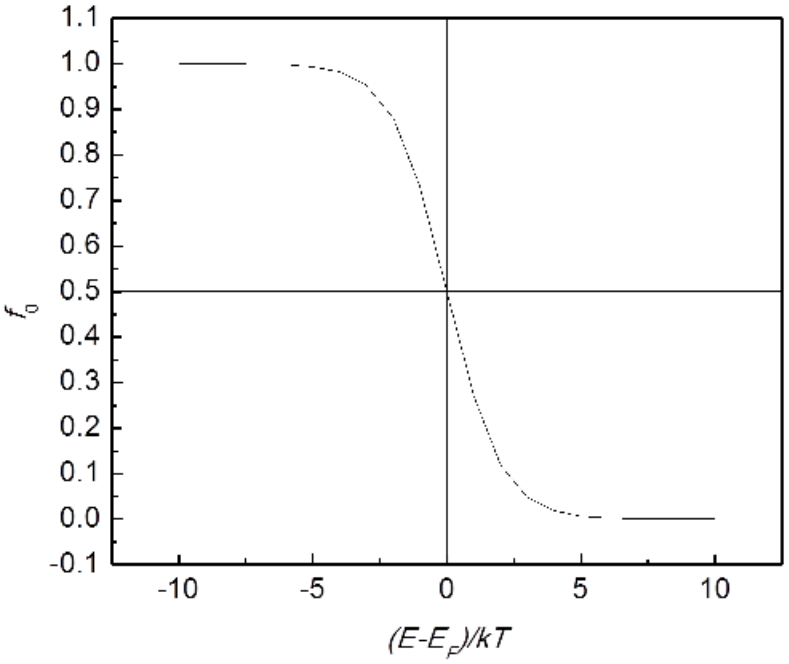

Figure 1.9. A plot of Fermi distribution depending on electron energy.

Quantum mechanics gives Fermi distribution to measure the probability that one energy state is occupied by electrons [Grosso et al, 2000].

$$f_0(E) = \left[\exp\left(\frac{E - E_F}{kT} \right) + 1 \right]^{-1} \quad \text{.....(1.27)}$$

E_F and k are Fermi level and Boltzmann's constant. Figure 1.9 is plotted according Equation 1.27, which shows that f_0 is equal to a number between 0 and 1 in a small energy range near Fermi level; otherwise it is equal to 1 when $E << E_F$ and 0 when $E >> E_F$. At Fermi level, f_0 is equal to 0.5. When f_0 is equal to 1, all the energy states are occupied, so conduction cannot happen because no empty state available for electrons to move. When f_0 is equal to 0, electrons cannot move either as no states available at all.

[Grosso et al, 2000] Fermi distribution infers a very important fact that is only the electrons with energy distributed around the Fermi level can participate in transport or conduction.

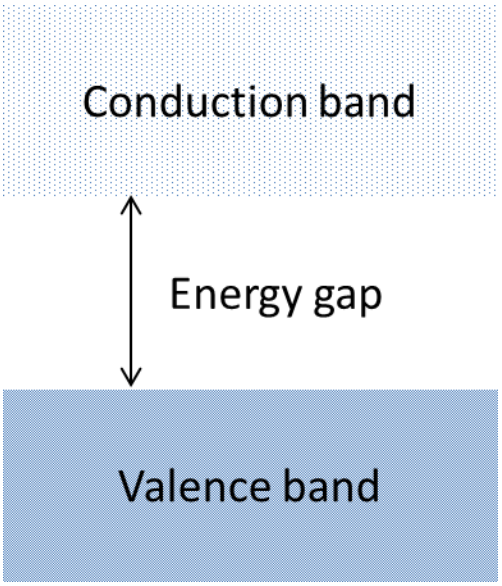

Figure 1.10. Electron energy diagram described by band structure.

In solid state physics, the electron energy diagram is described with band structure that is composed of conduction band, band gap and valence band [Grosson et al, 2000] (Figure 1.10). If Fermi level is in the band gap and distant to band edges, there will be no electrons in the conduction band and fully filled with electrons in the valence band so that the material will be insulator. However, if the band gap is small (several kT), thermal excitation can create electrons in the conduction band and leave holes in the valence band. This material is called intrinsic semiconductor and non-degenerate semiconductor [Grosson et al, 2000]. If the Fermi level is at the band edge or even in the band, there will be lots of empty states and also electrons and the material can be very conductive. This

often happens in metal or heavily doped semiconductor (or so-called degenerate semiconductor) [Grosson et al, 2000].

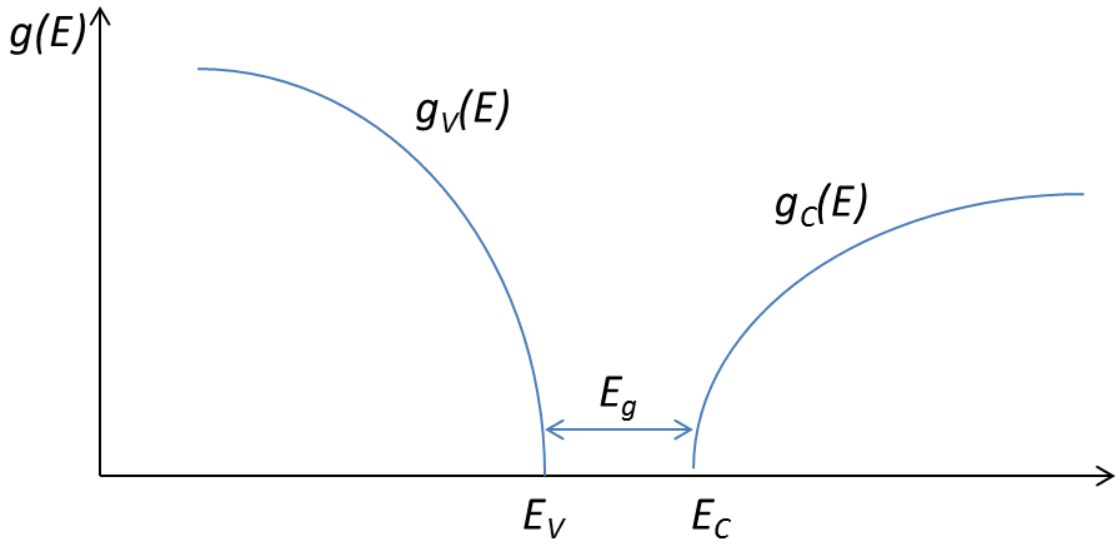

Figure 1.11. An illustration of density of states depending on electron energy.

Quantitatively, the band structure is described by *g(E)* (Figure 1.11) which is called density of states and the number of energy states between *E* and *E+dE* can be written as *g(E)dE* [Grosson et al, 2000]. Therefore, the total number of electrons is

$$n = \int_0^\infty f_0(E)g(E)dE \quad \text{.....(1.28)}$$

The discussion will become more understandable with the picture of band structure described above. The electron transport is based on the Boltzmann equation that assumes the distribution function *f* is slightly disturbed from equilibrium f_0 [Goldsmid et al, 2010a].

$$\frac{f(E)-f_0(E)}{\tau_e}=u\frac{df_0(E)}{dE}\left(\frac{dE_F}{dx}+\frac{(E-E_F)}{T}\frac{dT}{dx}\right) \quad \text{.....(1.29)}$$

Here, τ_e is relaxation time for charge carrier in the form of $\tau_0 E^r$. r is called scattering constant, which is equal to -1/2 for acoustic phonon scattering and 3/2 for ionized impurities scattering. If different scattering mechanisms exist, the reciprocal relaxation time can be added to calculate overall relaxation time [Goldsmid et al, 2010a]. u is the velocity of carriers. Electric current density, i, can be written as [Goldsmid et al, 2010a]

$$i=\mp\int_0^\infty euf(E)g(E)dE \quad \text{.....(1.30)}$$

e is the electron charge. The charge carrier heat flux density is [Goldsmid et al, 2010a]

$$j=\int_0^\infty u(E-E_F)f(E)g(E)dE \quad \text{.....(1.31)}$$

We can use $f(E)$-$f_0(E)$ to replace $f(E)$ in Equation 1.30 and 1.31, because no flux will happen when $f(E)=f_0(E)$. By applying Boltzmann equation (1.29), i and j can rewritten as

$$i=\mp\int_0^\infty eu^2\tau_e g(E)\frac{df_0(E)}{dE}\left[\frac{dE_F}{dx}+\frac{(E-E_F)}{T}\frac{dT}{dx}\right]dE \quad \text{.....(1.32)}$$

$$j=\int_0^\infty u^2\tau_e(E-E_F)g(E)\frac{df_0(E)}{dE}\left[\frac{dE_F}{dx}+\frac{(E-E_F)}{T}\frac{dT}{dx}\right]dE \quad \text{.....(1.33)}$$

Electrical conductivity can be obtained by the ratio of i to electrical field (dE_F/dx) when there is no temperature gradient ($dT/dx=0$) [Goldsmid et al, 2010a; Culter et al, 1969].

$$\sigma=-\int_0^\infty eu^2\tau_e g(E)\frac{df_0(E)}{dE}dE \quad \text{.....(1.34)}$$

Seebeck coefficient is calculated by the ratio of the electric field to the temperature gradient at the same condution [Goldsmid et al, 2010a; Culter et al, 1969].

$$S = \pm \frac{1}{eT}\left[E_F - \frac{\int_0^\infty g(E)\tau_e u^2 E^2 \frac{df_0(E)}{dE} dE}{\int_0^\infty g(E)\tau_e u^2 E \frac{df_0(E)}{dE} dE} \right] \quad \text{.....(1.35)}$$

Electron contribution, κ_e, to thermal conductivity is equal to the ration of j to –dT/dx when the electric current is zero [Goldsmid et al, 2010a; Culter et al, 1969].

$$\kappa_e = \frac{1}{T}\left\{ \frac{\left[\int_0^\infty g(E)\tau_e u E \frac{df_0(E)}{dE} dE \right]^2}{\int_0^\infty g(E)\tau_e u \frac{df_0(E)}{dE} dE} - \int_0^\infty g(E)\tau_e u E^2 \frac{df_0(E)}{dE} dE \right\} \quad \text{.....(1.36)}$$

In 1969 [Culter et al, 1969], Cutler and Mott derived the Mott relation based on the Equation 1.34, 1.35 and 1.36, which can be written as

$$S = -\frac{k}{e}\frac{1}{\sigma}\int_0^\infty \sigma(E)\left(\frac{E - E_F}{kT}\right)\left(\frac{df_0(E)}{dE}\right) dE \quad \text{.....(1.37)}$$

Here $\sigma(E)$ is defined as differential conductivity and it can be expressed as [Heremans et al, 2005a]

$$\sigma(E) = n(E)e\mu(E) \quad \text{.....(1.38)}$$

where $n(E)$ and $\mu(E)$ are defined as differential carrier concentration and differential mobility. In this formalism, the electrical conductivity can be written as [Shakouri, 2011]

$$\sigma = -\int_0^\infty \sigma(E)\left(\frac{df_0(E)}{dE}\right) dE \quad \text{.....(1.39)}$$

Equation 1.37 and 1.39 indicates several important points: first, the electrons with energy above and below Fermi level contribute negatively and positively to Seebeck coefficient, respectively, which can explain the sign of n-type and p-type semiconductors; second, the

electrons with energy farther away from Fermi level contribute more to the Seebeck coefficient; third, Seebeck coefficient is the difference between the differential electrical conductivity weighted mean energy of electrons and the Fermi level; four, Seebeck coefficient and electric conductivity are not independent.

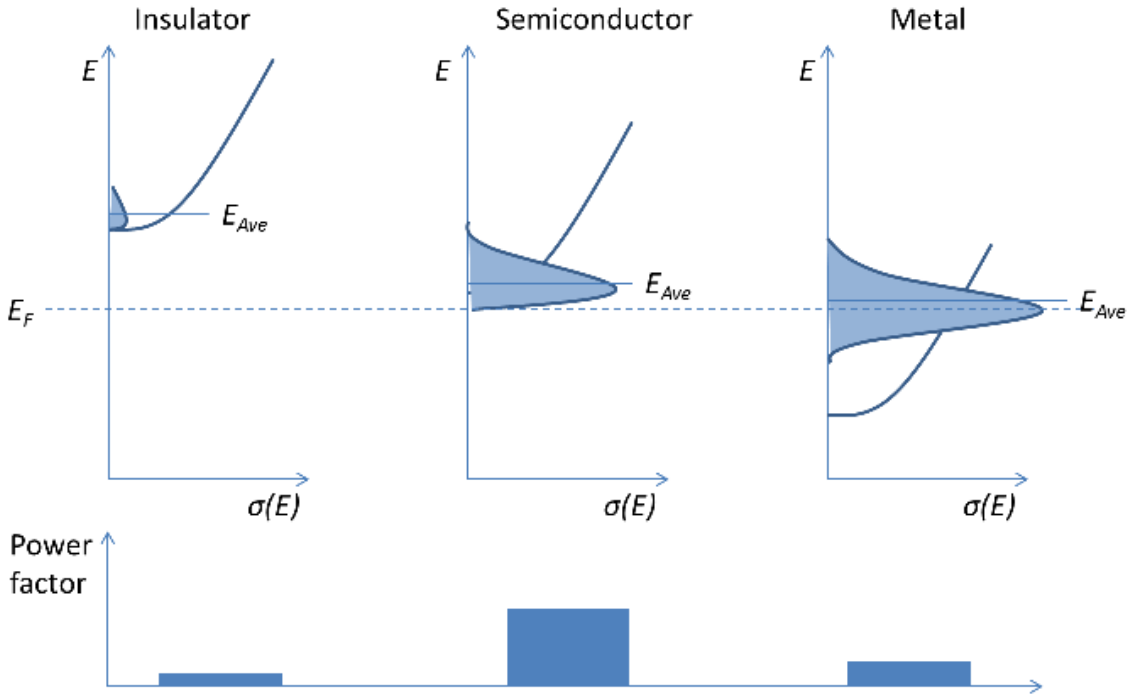

Figure 1.12. An illustration of the relation between Seebeck coefficient and electrical conductivity in insulator, semiconductor and metal.

Here we use Figure 1.12 to illustrate the relation between Seebeck coefficient and electrical conductivity [Shakouri, 2011]. In an insulator or non-degenerate semiconductor, the Fermi level in the band gap and distant to the band edge where the moving electrons locate, so the large margin between average energy of moving electrons and Fermi level results in a large Seebeck coefficient but small electrical conductivity. In a degenerate

semiconductor, the Fermi level in on the band edge which leads to a number of moving electrons in the conduction band, so it can have a good electrical conductivity and still a fairly large Seebeck coefficient. In a metal, the Fermi level is in the conduction band which results in large number of moving electrons that contribute to an excellent electrical conductivity but poor Seebeck coefficient because of the symmetrical distribution of electrons around the Fermi level. In conclusion, due to the trade-off between Seebeck coefficient and electrical conductivity, the electric power factor of degenerate (or heavily doped) semiconductor is the best and insulator or metal is a not good choice for thermoelectric application.

1.5 Thermal Conductivity and Bipolar Effect

As shown in Equation 1.36, the electrons can also transport heat and contribute to thermal conductivity. The Lorenz number was used to relate electrical conductivity and electron thermal conductivity.

$$L = \frac{\kappa_e}{\sigma T} \quad \text{.....(1.40)}$$

In the case of strongly degenerate semiconductor or metal, the Lorenz number is constant [Goldsmid et al, 2010a].

$$L = \frac{\pi^2}{3}\left(\frac{k}{e}\right)^2 = 2.44\times10^{-8} W\Omega K^{-2} \quad \text{.....(1.41)}$$

However, in the case of non-degenerate semiconductor, the Lorenz number is related to the scattering constant, *r* [Goldsmid et al, 2010a].

$$L = \left(\frac{k}{e}\right)^2\left(r+\frac{5}{2}\right) \quad \text{.....(1.42)}$$

From Equation 1.40, it can be seen that electron thermal conductivity will increase with electrical conductivity, which is to say that electrical and thermal conductivity are also related to each other. For a real material, the Lorenz number should be more carefully calculated through Equation 1.34 and 1.36.

The lattice vibration can also conduct heat and in the case of insulator it is the only means of heat conduction. Debye first shows thermal conductivity can be calculated by phonon mean free path l_t [Goldsmid et al, 1960].

$$k_l = \frac{1}{3} c_v v l_t \quad \text{.....(1.43)}$$

c_v is the specific heat per unit volume and v is the velocity of sound. When the temperature is above the Debye temperature (Θ), the phonon-phonon scattering dominates and the more intensive lattice vibration at high temperature would reduce the mean free path. Therefore, lattice thermal conductivity usually decreases with temperature [Goldsmid et al, 1960]. If the temperature is below the Debye temperature, boundary scattering dominates and the mean free path is decided by the size of the crystal. The specific heat is proportional to T^3, so the thermal conductivity would increase with temperature [Goldsmid et al, 1960].

The k_l is also influenced by other factors, such as size of the grains and carrier concentration. Bhandari and Rowe analyzed the thermal conductivity of sintered semiconductors with heavy doping that are frequently studied as thermoelectric materials [Bhandari et al, 1978]. The conclusion of their quantitative analysis is (shown in the case

of room temperature thermal conductivity of Si_{70}-Ge_{30} alloy) that smaller grain size or higher carrier concentration would lead to lower lattice thermal conductivity.

Another analysis that can provide instruction for selecting materials for thermoelectrics from the periodic table is described by Goldsmid in his book [Goldsmid et al, 2010b] and first developed by Keyes [Keyes et al, 1959]. In Keyes' calculation, k_l is written as

$$k_l = \frac{1}{T}\frac{R^{3/2}}{3\gamma^2\varepsilon_m^3 N_A^{1/3}}\frac{T_m^{3/2}\rho_d^{2/3}}{A^{7/6}} \quad \text{.....(1.45)}$$

In 1.45, N_A is Avogadro's number, A is the mean atomic weight, R is the gas constant, T_m is the melting temperature, ρ_d is the density, ε_m and γ do not change much for different materials. Therefore, the materials with higher atomic weight elements have lower lattice thermal conductivity. This trend was actually discovered experimentally by Ioffe in 1954 and he reported that the lattice thermal conductivity of materials with similar structure and bonding decreases as atomic weight increases [Goldsmid et al, 2010b].

So far we have known that the total thermal conductivity is comprised of electron and lattice contribution, but for semiconductors with narrow band gap or wide band gap at high temperature another contribution will become important which is from bipolar effect. The origin of bipolar effect is from the simultaneous electric conduction of electrons and phonons. In the conduction of two types of carriers, the current densities of electrons (n) and holes (p) can be written as [Goldsmid et al, 2010a]

$$i_n = \sigma_n\left(\frac{dV}{dx} - S_n\frac{dT}{dx}\right) \quad \text{.....(1.46)}$$

$$i_p = \sigma_p \left(\frac{dV}{dx} - S_p \frac{dT}{dx} \right) \quad \text{.....(1.47)}$$

The electrical conductivity can be calculated by setting $\frac{dT}{dx}$ to zero.

$$\sigma = \frac{i_n + i_p}{dV / dx} = \sigma_n + \sigma_p \quad \text{.....(1.48)}$$

The Seebeck coefficient can be calculated by setting $i_n + i_p$ to zero.

$$S = \frac{dV / dx}{dT / dx} = \frac{S_n \sigma_n + S_p \sigma_p}{\sigma_n + \sigma_p} \quad \text{.....(1.49)}$$

Since the signs of S_n and S_p are opposite, the magnitude of Seebeck coefficient will be reduced if minority carriers start to contribute in bipolar effect. The heat flux can be written as [Goldsmid et al, 2010a]

$$j_n = S_n T i_n - \kappa_{e,n} \frac{dT}{dx} \quad \text{.....(1.50)}$$

$$j_p = S_p T i_p - \kappa_{e,p} \frac{dT}{dx} \quad \text{.....(1.51)}$$

The thermal conductivity is defined at zero current ($i_n + i_p = 0$). By solving Equation 1.46 and 1.47 for *dV/dx* that is plugged back in either Equation 1.46 or 1.47, we can have

$$i_n = -i_p = \frac{\sigma_n \sigma_p}{\sigma_n + \sigma_p} (S_n + S_p) \frac{dT}{dx} \quad \text{.....(1.52)}$$

The thermal conductivity is calculated by $-\frac{(j_n + j_p)}{dT / dx}$.

$$\kappa_e = \kappa_{e,n} + \kappa_{e,p} + \frac{\sigma_n \sigma_p}{\sigma_n + \sigma_p} (S_n - S_p)^2 T \quad \text{.....(1.53)}$$

Interestingly, the total electron thermal conductivity is the sum of the thermal conductivities of both carriers and a third term that is called bipolar contribution. Researchers often write the total thermal conductivity as the sum of lattice contribution, single carrier contribution and bipolar contribution

$$\kappa = \kappa_l + \kappa_e + \kappa_b \quad \text{.....(1.54)}$$

even though bipolar contribution (κ_b) is actually a part of electron contribution (κ_e) [Rowe et al, 1983c]. The bipolar effect can become dominating at sufficiently high temperature when minority carriers is intensively thermally excited [Goldsmid et al, 1956].

1.6 Optimization of *ZT*

So far we have discussed the three material properties that decide the figure of merit *ZT*. It would be nice if *ZT* can be calculated by taking account of all the three properties. In a non-degenerate semiconductor, the *ZT* can be calculated as [Goldsmid et al, 2010b]

$$ZT = \frac{\left[\eta - (r + 5/2)\right]^2}{(\beta \exp(\eta))^{-1} + (r + 5/2)} \quad \text{.....(1.55)}$$

η is called the reduced Fermi energy and calculated by $\eta = \frac{E_F}{kT}$. In fact, the higher the η is, the higher the carrier concentration is as Fermi level is closer to the conduction band edge (in the case of n-type semiconductor). β is calculated as [Chasmar et al, 1959]

$$\beta = 2eT\left(\frac{2\pi kT}{h^2}\right)^{3/2}\left(\frac{k}{e}\right)^2\left(\frac{\mu(m^*)^{3/2}}{k_l}\right) \quad \text{.....(1.56)}$$

In Equation 1.56, h is the Planck constant and m^* is the effective mass. Only the $\left(\frac{\mu(m^*)^{3/2}}{k_l}\right)$ term in Equation 1.56 decides the magnitude of β, since other terms are calculated by either constants or temperature. Equation 1.55 shows that larger β leads to larger *ZT*, so the conclusion can be made that a material with large mobility and effective mass but small lattice thermal conductivity has decent *ZT*.

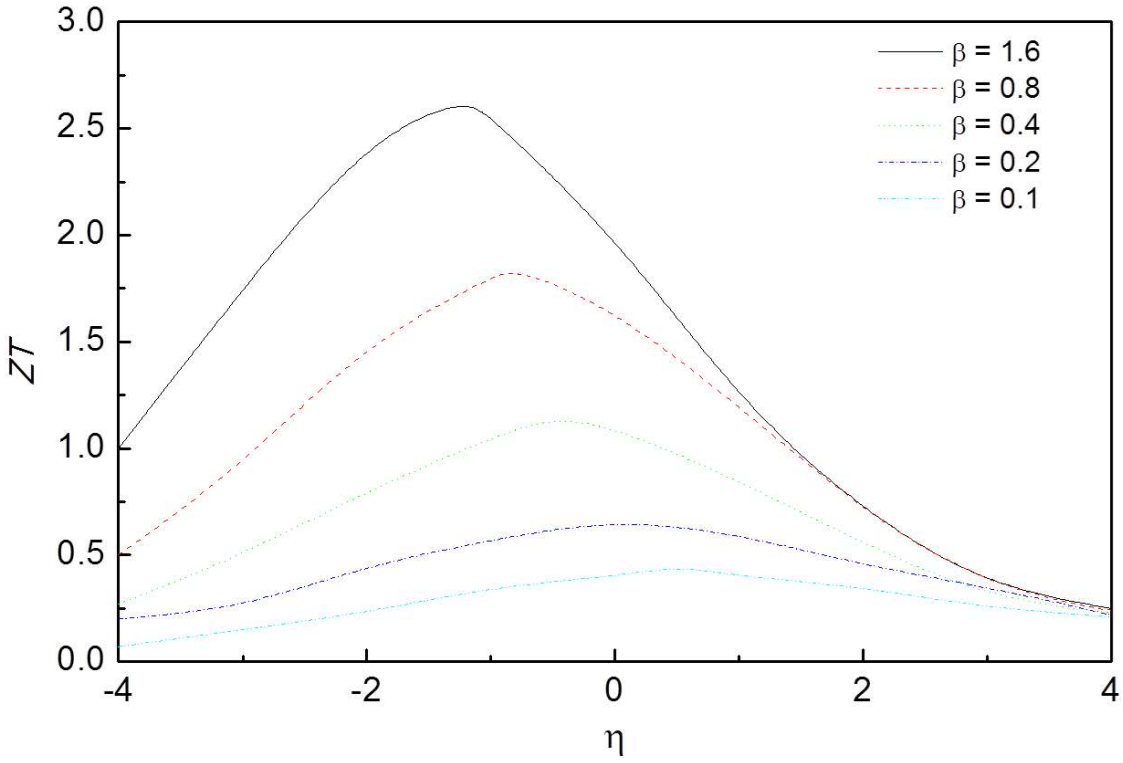

Figure 1.13. The calculation results of ZT depending on reduced Fermi level η at different β in the case of scattering parameter r = -1/2. [Adapted from reference Goldsmid et al, 2010b]

In Figure 1.13, the ZT is plotted out with variation of η at different β in the case of r = -1/2 [Goldsmid et al, 2010b]. First, ZT has a maximum value at certain reduced Fermi energy for each value of β. Since reduce Fermi energy is closely related to carrier concentration, tuning carrier concentration by doping is an effective way to optimize *ZT* in real material synthesis. Second, the magnitude of β decides the maximum ZT that can be obtained in the system. Similar diagrams can be drawn for other scattering mechanisms (*r*) [Rowe et al, 1983c].

The effective mass (m^*) is related to the band structure and in the unit of real electron mass (9.11×10^{-31} kg). For multi-valley band structure, the effective mass is written as [Rowe et al, 1983d]

$$m^* = N^{2/3}(m_1 m_2 m_3)^{1/3} \quad \text{.....(1.57)}$$

N is the number of valleys in the band structure and m_1, m_2, m_3 are the electron masses along the principal directions in each valley. The mobility is related to effective mass and proportional to $m_N^{-3/2} m_I^{-1}$ in the case of acoustic phonon scattering mechanism where m_N is $(m_1 m_2 m_3)^{1/3}$ and m_I is $3\left(1/m_1 + 1/m_2 + 1/m_3\right)^{-1}$ that is the effective mass of each valley [Goldsmid et al, 2010b]. Therefore, $\mu(m^*)^{3/2}$ in β is proportional to N/m_I, which is to say that a semiconductor with multiple valley (*N*) and smaller effective mass of each valley has better *ZT* [Goldsmid et al, 2010b]. Of course, low lattice thermal conductivity is also desired at the same time.

1.7 Conclusion

In this Chapter, I introduced thermoelectrics that can be applied for waste heat recovery and refrigeration. From the calculation of device efficiency, *ZT* was introduced that is calculated by three intrinsic properties: Seebeck coefficient, electrical conductivity and thermal conductivity. From a physical perspective, we discussed the factors that influence three properties individually and the internal connections among them. Finally, we discussed the factors or strategies to optimize ZT, which is very instructive in designing thermoelectric materials.

CHAPTER 2. NANOSTRUCTURED THERMOELECTRICS

In the past 20 years, thermoelectrics has achieved great progress because the introduction of nanotechnology into the field. In this chapter, we will discuss the reasons why nanotechnology can benefit thermoelectrics and improve *ZT*. This chapter is divided into several sub-chapters and each one will discuss one popular theory of nanostructured thermoelectrics. We will also summarize the popular methods of making nanostructured thermoelectric materials and state the motivation of my graduate research.

2.1 Quantum Confinement Effect

The application of nanotechnology into thermoelectrics was first inspired by the theoretical work reported by Hicks and Dresselhaus in 1993 [Hicks et al, 1993a; Hicks et al, 1993b]. In these two papers, the *ZT* of 2-D quantum well, i.e. thin film and 1-D quantum wire, i.e. nanowire were calculated based on a single parabolic band. In their calculation, the ZT of quantum well can be written as

$$Z_{2D}T = \frac{\left(2F_1/F_0 - \eta^*\right)^2 F_0}{1/\beta' + 3F_2 - 4F_1^2/F_0} \quad \text{.....(2.1)}$$

Here η^* is defined with the reduced Fermi energy (η) and thickness of thin film (a)

$$\eta^* = \eta - \frac{\hbar\pi^2}{2m_1 a^2 kT} \quad \text{.....(2.2)}$$

and F_0 and F_1 is Fermi-Dirac functions that are a function of η^* and the definition can be found in the paper. In Equation 2.1, the term β' is very similar to the β we discussed in Chapter 1.6.

$$\beta' = \frac{1}{2\pi a}\frac{2kT}{\hbar^2}\left(m_1 m_2\right)^{1/2}\frac{k^2 T\mu_1}{ek_l} \quad \text{.....(2.3)}$$

However, except for the parameters m^*, μ and k_l that have been discussed in Chapter 1.6, the thickness of thin film *a* can play an important role here. If the ultra-thin film can be fabricated, a large β' will be achieved which enhances *ZT*.

ZT can be significantly larger than 1 when β' is larger than 1. The *ZT* of Bi_2Te_3 thin film growing along *a-b* plane was calculated with variable thickness and current flowing in *c* direction [Hicks et al, 1993a]. When the film thickness is less than 1, the *ZT* becomes larger than 1 and increases very fast with decrease of the film thickness while bulk *ZT* can only achieve 0.52 with the same parameters.

In the same year, Hicks and Dresselhaus published another paper calculating the *ZT* of 1-D quantum wire. Similar results were obtained and the term β'' for 1-D quantum wire can be written as [Hicks et al, 1993b]

$$\beta'' = \frac{2}{\pi a^2}\left(\frac{2kT}{\hbar^2}\right)^{1/2}\frac{k^2 T m_1^{1/2}\mu_1}{ek_l} \quad \text{.....(2.4)}$$

where a is the diameter of the quantum wire with a square cross section. Reducing the diameter of the quantum wire can significantly increase β'' similar to the case of quantum wire.

Here is the calculation result of the optimized ZT of Bi_2Te_3 nanowire that grows along a direction against wire diameter a [Hicks et al, 1993b]. At a = 1 nm, Bi_2Te_3 quantum wire has ZT of 6 while Bi_2Te_3 quantum well has ZT of 2.5 and the bulk Bi_2Te_3 have ZT of 0.52. The trend indicates the advantage of making materials at lower dimensions.

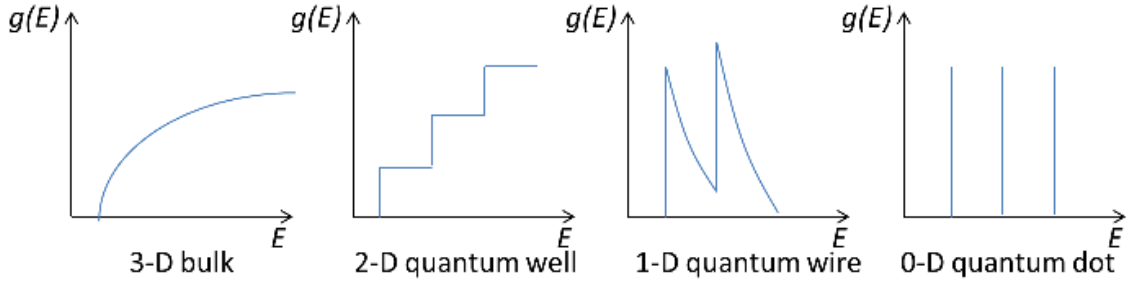

Figure 2.1. An illustration of the density of states against electron energy in 3-D bulk, 2-D quantum well, 1-D quantum wire and 0-D quantum dot.

In fact, the major improvement to ZT because of quantum confinement is the enhancement of Seebeck coefficient. Under the assumption of degenerate semiconductor, the Mott equation (Equation 1.37) can be written as [Heremans et al, 2012]

$$S = \frac{\pi^2}{3}\frac{k_B}{q}(k_B T)\left[\frac{1}{n(E)}\frac{dn(E)}{dE} + \frac{1}{\mu(E)}\frac{d\mu(E)}{dE}\right] \quad \text{.....(2.5)}$$

The Seebeck coefficient is dependent on the magnitude of $\frac{dn(E)}{dE}$ which is proportional to $\frac{dg(E)}{dE}$ (Equation 1.28). The density of states (DOS) per unit volume for a single band/sub band material system can be expressed [Pichanusakorn et al, 2010]

$$g_{3D}(E) = \frac{2^{1/2}}{\pi^2\hbar^3}\left(m_1 m_2 m_3\right)^{1/2} E^{1/2} \quad \text{.....(2.6)}$$

$$g_{2D}(E) = \frac{\left(m_1 m_2\right)^{1/2}}{a\pi\hbar^2}, E \geq E_n \quad \text{.....(2.7)}$$

$$g_{1D}(E) = \frac{\left(2m_1\right)^{1/2}}{a^2\pi\hbar}(E - E_{n,m})^{-1/2}, E \geq E_{n,m} \quad \text{.....(2.8)}$$

Here E_n and $E_{n,m}$ are defined as confinement energy. The *g(E)* of 0-D quantum dots is a series of delta function (δ) because it becomes quite like atoms [Kuno et al, 2011]. The *g(E)* against energy can be illustrated in Figure 2.1 [Heremans et al, 2005b]. As shown in the figure, the quantum confinement effect significantly increases the energy dependency of *g(E)*, which can enhance the term $\frac{dn(E)}{dE}$ in Equation 2.5 so that Seebeck coefficient can be strongly improved [Heremans et al, 2005a].

On the other hand, an increase in $\frac{d\mu(E)}{dE}$ will also lead to an enhancement in Seebeck coefficient. $\mu(E)$ is proportional to relaxation time $\tau(E)$ which can be calculated by

$$\tau = \tau_0 E^r \quad \text{.....(2.9)}$$

for semiconductors with parabolic bands [Heremans et al, 2005a]. τ_0 is energy-independent relaxation time and *r* is called scattering parameter, different values of which

represent different scattering mechanisms. r = -1/2 is for scattering of electrons on acoustic phonons; r = 0 is for scattering of electrons on neutral impurities; r = 3/2 is for scattering of electrons on ionized impurities [Heremans et al, 2005a]. A larger scattering constant will lead to a higher Seebeck coefficient. Scattering of electrons on interfacial boundaries due to the large specific surface area can increase the scattering parameter, which in turn improve Seebeck coefficient [Heremans et al, 2004]. However, this improvement comes at a price that is the reduction in mobility or electrical conductivity [Heremans et al, 2004]. Therefore, it needs more careful discussion to claim this is beneficial for *ZT* enhancement. It is worth noting that Hicks and Dresselhaus' two papers did not count in the effect of interfacial boundaries scattering on carrier mobility and they used the bulk mobility in their calculation.

Another potential benefit of the quantum confinement is an increase in band gap, which can transform semimetal in bulk form that has poor *ZT* to semiconductor at nanoscale that possesses better *ZT* [Hicks et al, 1993c]. Hicks and Dresselhaus calculated the band overlap between the lowest conduction band and highest valence band and it can written as [Hicks et al, 1993c]

$$\varepsilon_0 = \varepsilon_0^{bulk} - \frac{\hbar^2 \pi^2}{2 m_{ez} a^2} - \frac{\hbar^2 \pi^2}{2 m_{hz} a^2} \quad \text{.....(2.10)}$$

Semimetal has positive band overlap. As a decreases, the ε_0 becomes more negative meaning band gap become positive. A frequently cited example is theoretical calculation of *ZT* of Bi nanowire [Lin et al, 2000]. The calculation indicates that when the diameter of Bi nanowire is reduced to a critical value (50 nm), Bi nanowire transits from

semimetal to semiconductor, which improves the *ZT* of Bi that is usually not considered as a good thermoelectric material in bulk form.

The theoretical prediction stimulated a series of experimental efforts to test the improvement brought by quantum confinement. Lin and Dresselhaus synthesized $Bi_{1-x}Sb_x$ nanowires with different diameters and observed the theoretically predicted semimetal to semiconductor transition with the decrease of diameters [Lin et al, 2002]. The Seebeck coefficient is significantly improved compared to bulk Bi after the diameter of $Bi_{1-x}Sb_x$ nanowire reaches 45 nm [Lin et al, 2002]. Hicks and Dresselhaus grew PbTe/$Pb_{1-x}Eu_xTe$ 2-D quantum well using molecular beam epitaxy (MBE) [Hicks et al, 1996]. The data shows that the 2-D quantum well system has increased Seebeck coefficient with film thickness that is much higher than bulk PbTe when the thickness reaches 5 nm [Hicks et al, 1996]. T. C. Harman fabricated $PbTe_{1-x}Se_x$/PbTe quantum dots superlattice (QDSL) film which creates a delta function distribution of density of states and discrete energy levels in a 3-D matrix that can favor thermoelectric properties [Harman et al, 2002]. A *ZT* of 1.6 was achieved at room temperature. A possible mechanism proposed is the miniband formation in coupled 3-D quantum dots arrays [Balandin et al, 2003], but the major mechanism for the *ZT* enhancement is the reduction of lattice thermal conductivity due to the interfacial boundary scattering of phonons [Heremans et al, 2005b; Lin et al, 2003), which will be discussed more later in this chapter.

Quantum confinement effect in thermoelectrics proposed by Hicks and Dresselhaus stimulated researchers' interest in nanostructured materials in the field, which started the

20 years of development of nanostructured thermoelectrics until present. During the development, a few other theories have been proposed that are worth discussion here.

2.2 Energy Filtering Effect

Energy filtering effect is another popular theory that predicted enhanced Seebeck coefficient or power factor. In the last section, we have already mentioned the interfacial boundaries can increase the scattering parameter of electrons in PbTe nanocomposite, which improved Seebeck coefficient [Heremans et al, 2004]. Heremans attributes the improvement to preferential scattering of electrons depending on their energy [Heremans et al, 2004]. Later on researchers designed binary nanocomposites or superlattice to intentionally create electron transport barrier for optimal utilization of this effect. The reason for Seebeck coefficient improvement can be intuitively understood based on the discussion in the first chapter (Figure 1.12).

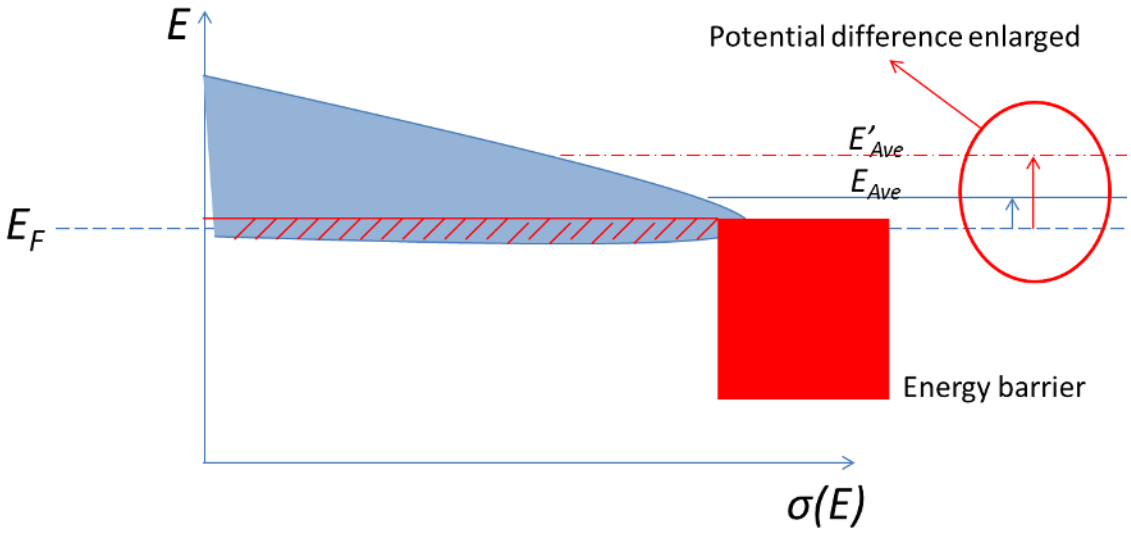

Figure 2.2. An illustration of energy filtering effect. The energy barrier blocks the low energy electron transport, which improves the average energy of moving electrons.

As shown in Figure 2.2, the average energy of moving carriers increases because the energy barrier blocks lower energy carriers. The result is that the increased the difference between Fermi level and average energy of moving carriers leads to a higher Seebeck coefficient. Of course, the electrical conductivity will decrease because of the energy filtering. Therefore, optimizing the system is crucial for power factor enhancement. Faleev and Léonard reported their theoretical calculation results on a system with metallic nanoinclusions embedded in PbTe matrix [Faleev et al, 2008]. The results summarize three important factors in optimizing the system and the inverse of relaxation time from nanoinclusion scattering that is more energy dependent than bulk relaxation time.

$$\tau_i^{-1}(E) \approx \frac{V_B^2 x}{R} E^{-3/2} \quad \text{.....(2.11)}$$

τ_i is the relaxation time due to electron scattering on nanoinclusions, V_B is defined as the energy barrier at the interface between nanoinclusions, matrix and R is the radius of nanoinclusions and x is the volume fraction of nanoinclusions. First, Seebeck coefficient will increase with reduced radius of nanoinclusions (R) at a fixed volume fraction, since smaller nanoinclusions have larger surface area.

The calculation result that PbTe with metallic nanoinclusions has higher Seebeck coefficient than PbTe and smaller radius of nanoinclusions leads to even higher Seebeck coefficient at the same carrier concentration. Second, the power factor can reach maximum at an optimal energy barrier (V_B).

An increased energy barrier (V_B) leads to an improved Seebeck coefficient but a reduced electrical conductivity, so an optimal power factor can be obtained at an energy barrier of 0.07 eV for the system of PbTe with metallic nanoinclusions. Zebarjadi reported their theoretical calculation results on another system with ErAs nanoinclusions embedded in InGaAlAs matrix [Zebarjadi et al, 2009]. The material used for comparison is Si doped InGaAlAs. The influence of energy barrier height and nanoinclusion concentration on Seebeck coefficient, electrical conductivity and power factor is considered.

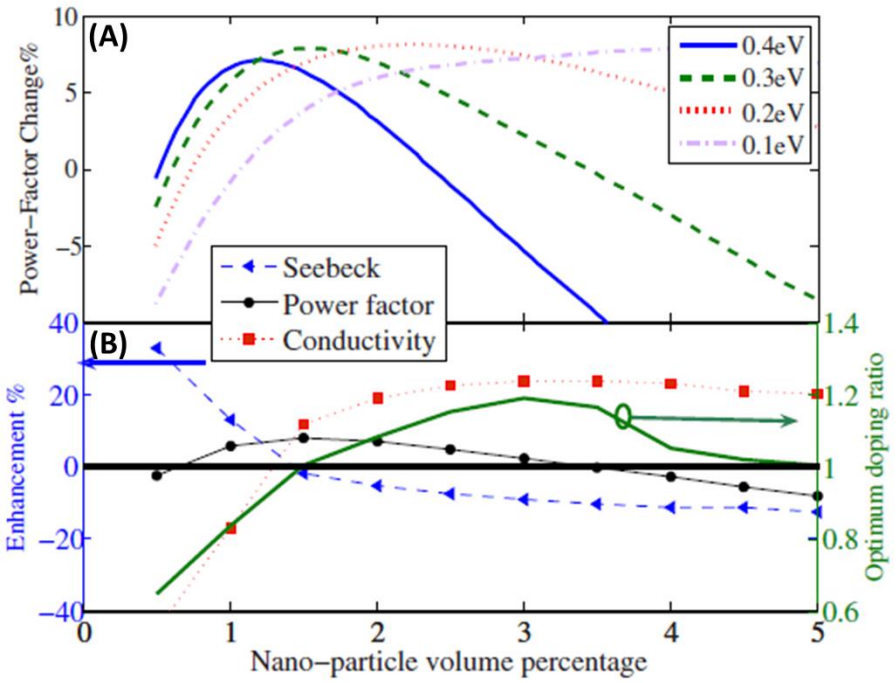

Figure 2.3. (A) Enhancement of the power factor of the nanoparticle sample with respect to that of the Si-doped sample by percentage. Four different energy barriers are included for calculation. (B) Enhancement of power factor and the corresponding Seebeck coefficient and electrical conductivity and the ratio of the optimum electron concentration of the samples with embedded nanoparticle at an fixed energy barrier height of 0.3 eV to that of the bulk material. [Adapted from reference Zebarjadi et al, 2009]

A few important conclusions are made in the paper (Figure 2.3). First, the highest improvement of power factor by including ErAs nanoparticles instead of Si dopant is 5% - 8%. Second, the energy barrier height does not influence the magnitude of maximum power factor but the optimal concentration of ErAs nanoinclusions. Third, the ErAs nanoinclusions can act as modulation dopants to increase the carrier concentration; the improvement of power factor mainly comes from the increase of electrical conductivity with a less reduced Seebeck coefficient than that found in Si doped InGaAlAs, which results from the interfacial scattering of electrons on the ErAs nanoinclusions.

Many papers that focus on the experimental study of energy filtering effect can be found in previous literature. Here are a few examples. Zeng fabricated ErAs:InGaAs/InGaAlAs superlattice and measured the in-plan and cross-plan Seebeck coefficient [Zeng et al, 2007]. The result shows that the Seebeck coefficient measured cross plan is significant larger than that in plan at the same carrier concentration, which indicates energy filtering effect due to the energy barrier between InGaAs and InGaAlAs. Heremans made PbTe matrix with Pb nanoinclusion and found its Seebeck coefficient is improved compared to pure PbTe at the same carrier concentration [Heremans et al, 2005c]. Ko and Murry blended platinum (Pt) nanoinclusions (13nm) with antimony telluride (Sb_2Te_3) and then drop-casted the mixture on glass substrates for thermoelectric property measurement [Ko et al, 2011]. The mixture has a larger Seebeck coefficient but lower electric conductivity than pure Sb_2Te_3 and the power factor is actually slightly improved by blending Pt nanoinclusions. Sumithra and Stokes incorporated Bi nanoinclusions in the matrix of Bi_2Te_3 and found the electric conductivity increases by a factor of 2 but the Seebeck coefficient decreases compared to pure Bi_2Te_3 [Sumithra et al, 2011]. They actually found that Bi nanoinclusions donate electrons to the matrix and improves the carrier concentration of the composite, which causes the reduced Seebeck coefficient. However, when compared to that of the pure Bi_2Te_3 at the same high carrier concentration, the Seebeck coefficient of the composite is still larger which implies the energy filtering effect. Zhang and Bahk have recently published a paper, in which a thin layer of oxide was deposited between Ag and Sb_2Te_3 to minimize Ag diffusion in matrix [Zhang et al, 2014]. The result shows Ag nanoinclusions remain intact in the Sb_2Te_3 and the Seebeck coefficient of Ag/oxide/Sb_2Te_3 was improved compared to the matrix that at a lower

carrier concentration. Pisarenko relation was also calculated at different cut-off band potentials and the experimental data points locate above the curve, which strongly suggests the existence of energy filtering effect.

Another important effect commonly coexisting with energy filtering in multiphase nanocomposite is modulation doping that is worth a short discussion here. Modulation doping has potential to improve *ZT* as well, because dopants are separated from the matrix and charge carriers can transport freely without ionized impurity scattering in the un-doped matrix; this leads to a simultaneously high mobility and carrier concentration [Dingle et al, 1978; Friedrich et al, 1997]. The advantage of modulation doping in thermoelectrics is electrical conductivity improvement at the same carrier concentration and Seebeck coefficient because of the higher carrier mobility than traditionally doped materials. In real material design, a heavily doped second phase is usually used to dope the matrix instead of traditional ionized impurity dopants. For example, B (p-type) or P (n-type) doped Si nanoinclusions were embedded in the $Si_{80}Ge_{20}$ matrix and both cases have an enhanced power factor compared to those of traditionally doped samples, $Si_{80}Ge_{20}B_x$ and $Si_{80}Ge_{20}P_y$ [Zebarjadi et al, 2011]. Work from the same group on $Si_{70}Ge_{30}P_x$ nanoinclusion doped $Si_{95}Ge_5$ also showed an enhanced power factor compared to that of the traditionally doped $Si_{95}Ge_5P_y$ sample [Yu et al, 2012].

The energy filtering effect has been proven to be able to improve Seebeck coefficient and power factor, but it requires careful optimization of material systems. Heremans observed electron mobility decreases by a factor of 3 in the Pb:PbTe system because of the

embedding of Pb nanoinclusion [Heremans et al, 2005c]. Even after optimization of the material system, Zebarjadi only obtained 5% - 8% power factor improvement that is quit marginal in ErAs: InGaAlAs system [Zebarjadi et al, 2009]. Even though modulation doping can maintain a relatively high carrier mobility, still the power factor enhancement is limited to around 20% [Zebarjadi et al, 2011; Yu et al, 2012]. However, another factor that also plays an important role has not been discussed, which is the thermal conductivity reduction because of the nanostructuring. The loss from the electrical conductivity is possible to be compensated by the thermal conductivity reduction. In the next section, we will discuss the thermal conductivity of nanostructured materials in detail.

2.3 Reduction of Thermal Conductivity by Nanostucturing

The previous sections only cover the effects of nanostructuring on electron transport that influence power factor. In this section, we will discuss its effects on thermal conductivity that play a central role and are well accepted as the major reason for improvement of *ZT* in nanostructured materials. As discussed in the chapter 1, the thermal conductivity is contributed from both electron and phonon transport. If we use the Wiedemann-Franz law for metal or highly-degenerate semiconductor (Equation 1.40 and 1.41), the *ZT* can be written as

$$ZT = \frac{S^2}{L}\left(1+\frac{\kappa_l}{\kappa_e}\right)^{-1} \quad \text{.....(2.12)}$$

Equation 2.12 indicates that small lattice thermal conductivity is wanted but a large electron thermal conductivity needs to be maintained or a decreased ratio of κ_l / κ_e is needed, which requires a unique material structure called "phonon–glass electron–crystal" which is quite difficult to realize in traditional materials [Bhandari, 2005]. Due to the nanoscale size and boundary scattering, phonon mean-free path is reduced, leading to a lower lattice thermal conductivity. The detailed analysis will be discussed below.

The lattice thermal conductivity can be calculated for an isotropic material [Chen et al, 2005]:

$$\kappa_l(T) = \frac{1}{3}\int C_\lambda(\lambda,T)v(\lambda)L(\lambda,T)d\lambda \quad \text{.....(2.13)}$$

λ is the wavelength, C_λ is the spectral specific heat per unit wavelength, v is the spectral group velocity and L is the spectral mean-free path. Proposed by Dames and Chen [Chen et al, 2005], two strategies can be used to reduce the lattice thermal conductivity: first, reducing the $C_\lambda v$ term by altering the phonon dispersion relation; second, reducing L term by boundary scattering on nanoscale grains.

The first strategy can be realized by altering the dispersion relations, i.e. reducing specific heat and group velocity, which requires that the nanograin size is comparable or even smaller than the phonon wavelength, so the length scale of the phonon wavelength is very important. Under the approximation that neglects the frequency dependence of the mean-free path, the following equation can be obtained using Equation 2.13 [Chen et al, 2005].

$$\int_{\lambda_{\min}}^{\lambda_\alpha(T)} C_\lambda(\lambda,T)v(\lambda)d\lambda = \alpha\int_{\lambda_{\min}}^{\lambda_{\max}} C_\lambda(\lambda,T)v(\lambda)d\lambda \quad \text{.....(2.14)}$$

Here $\lambda_\alpha(T)$ is defined as the wavelength below which α of the thermal conductivity was contributed and α represents percentage. For example, if α=50%, it means that 50% of the thermal conductivity is contributed by phonon of wavelength smaller than $\lambda_{50}(T)$.

Dames and Chen introduced normalized wavelength (λ/λ_0) and normalized temperature (T/T_0) to describe $\lambda_\alpha(T)$. λ_0 and T_0 are defined as characteristic wavelength and temperature that are different from one material to another. For Si, λ_0 = 0.55 nm and T_0 = 530 K; for PbTe, λ_0 = 0.66 nm and T_0 = 126 K [Chen et al, 2005]. In realistic applications, the thermoelectric materials are usually used at the temperature comparable to or even higher than T_0. It can be seen that λ/λ_0 almost stay as constants and a simple calculation can give us that $\lambda_{50} \approx 1\,\text{nm}$ and $\lambda_{90} \approx 2\,\text{nm}$ for both Si and PbTe, which is to say that almost 90% of the thermal conductivity is contributed by phonons with wavelength smaller than 2 nm. As mentioned previously, altering the dispersion relations needs the nanograin size comparable to or even smaller than the wavelength of phonons. Since achieving size of 2 nm is very difficult, the dispersion relations stay almost unchanged in most cases, which is to say the first strategy is very difficult to realize. However, the surface roughness of nanograin is usually comparable to the wavelength of phonons which leads to diffusive scattering at the interface while the thermal wavelength of electrons is much larger than that of phonons or surface roughness which results in specular scattering at the interface. The diffusive scattering can provide more resistance

than the specular scattering, which means that interfaces will scatter phonon transport while still maintain a good electron transport, leading to a lower κ_l / κ_e [Chen et al, 2005].

Compared to the first strategy of altering dispersion relation, shortening the mean free path of phonon (L) is more effective in reducing the thermal conductivity, which can be realized by making the crystal size smaller and taking advantage of boundaries scattering. A simple relation between the mean free path of phonon and crystal size was proposed by Bhandari [Bhandari, 2005]: L = 1.12 D and D stands for the side of a specimen with square cross-section. Therefore, the length scale of mean free path of phonon in the bulk materials is very important, since it decides the critical size of crystals which begins to influence thermal conductivity significantly. In the bulk materials, the phonon mean free path can be limited by phonon-phonon scattering, phonon-electron scattering, phonon-impurity scattering [Bhandari, 2005]. Similar to the analysis in estimating the length scale of phonon wavelength, the percentage phonon mean free path can be calculated [Chen et al, 2005]

$$\int_0^{L_\alpha(T)} k_L(L,T)dL = \alpha \int_0^{L_{\max}} k_L(L,T)dL \quad \text{.....(2.15)}$$

Here $L_\alpha(T)$ is defined as the mean free path below which α of the thermal conductivity was contributed and α represents percentage. According to the calculation of Dames and Chen [Chen et al, 2005], for bulk Si at 300 K, only 10% of the thermal conductivity is contributed by phonons with mean free path less than 87 nm which the phonons with mean free path up to 12.8 μm contributes 90% of the thermal conductivity. The calculation indicates that a large portion of the thermal conductivity is from the phonons

with long mean free paths, which is to say making grain size nanoscale can significantly reduce thermal conductivity compared to bulk Si. Li et al synthesized Si nanowire with different diameter: 115 nm, 56 nm, 37 nm, 22 nm. The thermal conductivity measurement clearly shows the trend of reducing thermal conductivity with smaller diameter of Si nanowire and the 56 nm Si nanowire possesses only 15% of bulk Si thermal conductivity [Li et al, 2003a; Dames et al, 2004).

Of course, the length scale of phonon mean free path is different from one material to the other. The phonon mean free path of bulk PbTe is about one order of magnitude smaller than that of bulk Si. For bulk PbTe at 300 K [Chen et al, 2005], 10% of the thermal conductivity is contributed by phonons with mean free path less than 6 nm while 90% of the thermal conductivity is contributed by phonons with mean free path less than 860 nm. However, the length scale still gives lots of space of thermal conductivity reduction and the PbTe nanostructured material with feature size of 10 nm possess only 26% of the bulk PbTe according to the calculation of Dames and Chen [Chen et al, 2005].

The significant thermal conductivity reduction in nanostructured materials have stimulated a large number of experimental studies among which some record breaking *ZT* values were reported. Venkatasubramanian et al fabricated Bi_2Te_3/Sb_2Te_3 and $Bi_2Te_3/Bi_2Te_{2.83}Se_{0.17}$ superlattice thin film with different periodicities (2 – 25 nm) using molecular beam epitaxy (MBE) and achieved extremely small lattice thermal conductivity of 0.25 W/m-K for Bi_2Te_3/Sb_2Te_3 (33% of bulk counterpart) and 0.58 W/m-K (34% of bulk counterpart) for $Bi_2Te_3/Bi_2Te_{2.83}Se_{0.17}$ thin film in the *c* direction, leading to a *ZT* of 2.4 and 1.46 at 300 K, respectively [Scherrer et al, 1995; Venkatasubramanian,

2000; Venkatasubramanian, 2001]. Harman et al applied similar method (MBE) to fabricate PbTe/$PbSe_{0.98}Te_{0.02}$ quantum dot superlattice thin film with a periodicity of 13 nm. The deduced lattice thermal conductivity is 0.33 W/m-K at 300 K that is only 16% of its bulk counterpart [Harman et al, 2002; Goldsmid, 2010c; Harman et al, 2000]. Lee et al grew $Si/Si_{1-x}Ge_x$ ($x = 0.9 - 0.95$) superlattice nanowire and found its lattice thermal conductivity can be further reduced compared to pure Si nanowire with similar diameter (~ 56 nm) from 26 W/m-K to 6 W/m-K [Li et al, 2003a; Li et al, 2003b]. The above materials are either thin films or individual nanowires fabricated by expensive MBE or Chemical Vapor Deposition (CVD). Hsu et al used high temperature solid state reaction and controlled cooling to grow Ag-Sb-rich precipitates (quantum dots) in PbTe matrix. The lattice thermal conductivity of 1 W/m-K (50% of bulk PbTe) at 300 K was obtained and a *ZT* of 2.0 can be achieved in this bulk material with nano-precipitates at 800 K [Goldsmid, 2010c; Hsu et al, 2004]. Poudel et al fabricated $Bi_{0.5}Sb_{1.5}Te_3$ bulk nanocomposites using ball milling and hot press and obtained a lattice thermal conductivity of 0.6 W/m-K while the bulk sample has a thermal conductivity of 0.9 W/m-K at 300 K, so an enhanced *ZT* of 1.4 was achieved [Poudel et al, 2008]. Biswas et al fabricated PbTe matrix with SrTe precipitates with controlled cooling and developed a so-called all-scale hierarchical architecture to scattering phonons with different mean free paths. A largely enhanced ZT of 2.2 was achieved at 925 K due to the significant reduction thermal conductivity down to 0.55 W/m-K that is only 55% of the bulk sample with the sample composition and doping concentration [Biswas et al, 2012].

From the discussion so far in the second chapter, we know that nanostructuring has been proven to be able to improve the thermoelectric performance of materials theoretically and experimentally. The next important question is how to produce such nanostructured materials, so the unique benefits can be applied to real life situation. In the next section, I am going to summarize popular ways of making nanostructured materials for thermoelectric application.

2.4 Nanostructured Materials Preparation

2.4.1 High Vacuum Deposition

In general, four popular methods are used to prepare nanostructured materials that are vapor deposition, mechanical alloying and milling, precipitation from solid solution and solution synthesis. Vapor deposition is usually used to fabricate thin films and need delicate facilities. The process usually involves deposition by chemical or physical routes on selected substrates with certain growth orientation in a high vacuum environment [Böttner et al, 2006]. The thickness of thin films can be accurately controlled and even composites can be fabricated by changing the precursors in turns. The best example is that Venkatasubramanian et al fabricated Bi_2Te_3/Sb_2Te_3 and $Bi_2Te_3/Bi_2Te_{2.83}Se_{0.17}$ superlattice thin film with different periodicities [Venkatasubramanian et al, 2001]. Popular vapor deposition methods are MBE [Mzerd et al, 1995; Mzerd et al, 1994; Beyer et al, 2002], metallorganic chemical vapor deposition (MOCVD) [Venkatasubramanian et al, 1999], flash-deposition [Völklein et al, 1990; Foucaran et al, 1998]. However, MBE only produce micro-thickness thin films even after a long period of time [McCray et al, 2007], so it can serve quite few specialized applications in thermoelectrics [Chowdhury

et al, 2009]. Here we will discuss the other three methods: mechanical alloying and milling, precipitation from solid solution and solution synthesis that are able to produce centimeter size bulk samples with nanostructures.

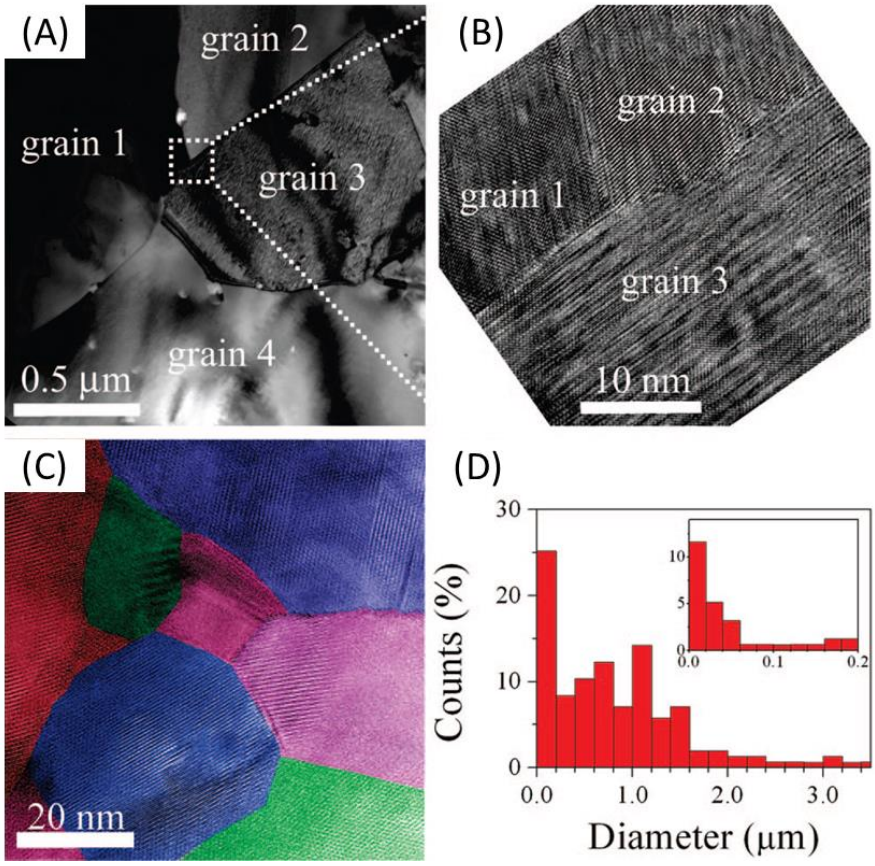

Figure 2.4. (A) Bright field transmission electron microscope (TEM) image of multigrains, (B) high resolution TEM (HRTEM) of grain boundaries, (C) HRTEM images of smaller grains, and (D) particle size distribution histogram for the nanograined bulk material with the inset zooming in on the distribution of small size particles less than 200 nm. [Adapted from reference Lan et al, 2009]

2.4.2 Mechanical Alloying and Milling

Mechanical alloying and milling include two different ways of synthesizing thermoelectric materials. Mechanical alloying means individual elements are directly

ground to form alloys while mechanical milling usually refers to grinding crystalline ingots into nanoparticles. The advantage of mechanical alloying and milling is that large quantity of nanopowder can be produced through a relative convenient procedure and with a minimal requirement for equipment [Harringa et al, 2005]. A typical device is composed a sealed chamber which can rotate or oscillate with milling balls and samples are ground through the friction between moving balls [Harringa et al, 2005]. Before high-energy ball milling was introduced in 1970s [Suryanarayana et al, 2001], mechanical alloying and milling is taken as a way to synthesize thermoelectric materials directly and a variety of materials were produced, such as Si-Ge, rare-earth sulfides, Bi-Sb-Te, Pb-Te, Fe-Si and skutterudites [Harringa et al, 2005]. High-energy ball milling is able to produce large quantity of nanoparticles without surfactants that are usually used to control the crystal growth in solution synthesis [Suryanarayana et al, 2001]. Direct alloying [Joshi et al, 2008; Ma et al, 2008] or milling from crystal ingots [Poudel et al, 2008] can both be found in the literature. Afterwards, consolidation methods, such as hot pressing or spark plasma sintering, are applied to obtain bulk materials with nanosize grains. The relative density of consolidated materials can reach as high as 98% or even 100%, which is very important since porosity can significantly reduce electrical conductivity by increasing scattering surface area. The review article by Lan et al summarized a large number of materials fabricated with this method [Lan et al, 2010]. Figure 2.4 show the high resolution TEM images of the hot pressed $Bi_{0.5}Sb_{1.5}Te_3$ nanocomposite [Lan et al, 2009]. The size distribution analysis indicates that the majority of grains have sizes below 1.6 μm and 17 % of the grains are in the range of 0 – 40 nm. The wide size distribution also

benefits the scattering of phonons with a large range of mean free path as discussed in Chapter 2.3.

In conclusion, mechanical alloying and milling has been developed into a very mature method of making different kinds of thermoelectric nanocomposites and significant improvement of *ZT* was observed in literature. The advantages include simple procedure, minimal requirement on equipment, large yield and surfactant-free environment. The disadvantages include energy intensive, time consuming and little morphology control.

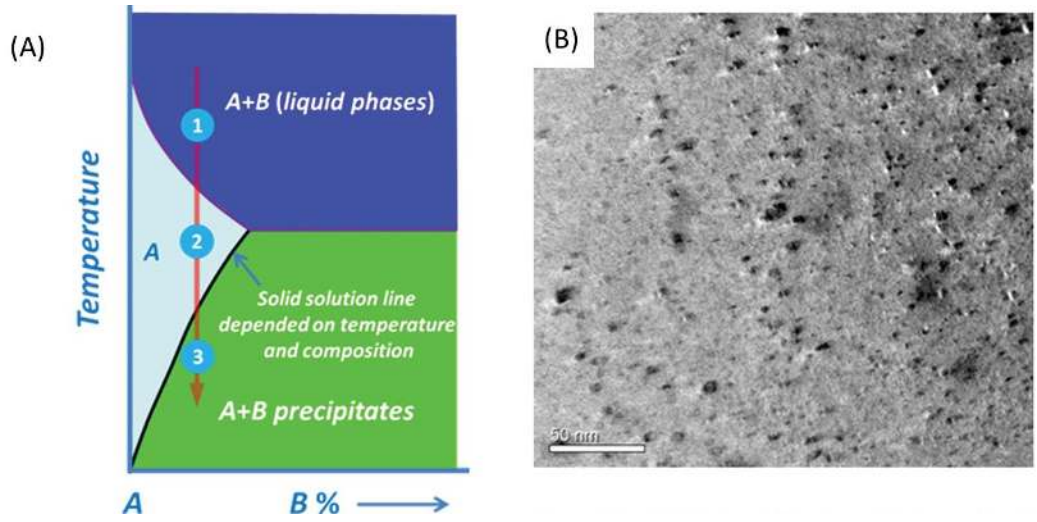

Figure 2.5. Nanostructure formation approach: (A) schematic ternary diagram, which indicates a strongly temperature-dependent solubility of the second phase of B in the A matrix, (B) typical nanostructural precipitates observed by TEM. [Adapted from reference Zhao et al, 2014]

2.4.3 Precipitation From Solid Solution

Another extremely successful method of making nanostructured materials is through precipitation from solid solution. Different from the nanostructured materials made by

mechanical alloying and milling that are composed of nanosize grains, the nanostructured materials made by precipitation from solid solution is a major bulk matrix embedded with a second phase of nanoprecipitates that can act as scattering center to reduce thermal conductivity. The advantage of this method is that the effect on electron transport can be minimized while phonons are scattered. A typical process is described in Figure 2.5A [Zhao et al, 2014]: first, the A-B mixture is heated up above the solid-liquid temperature line (step 1); second, the A-B mixture is then cooled down and annealed at step 2 where B completely dissolves in A as a single phase; third, the A-B mixture is further cooled down to step 1 where the minority phase starts to precipitate below the solid solubility line. This method was first proven to be able to fabricate materials with high *ZT* in $AgPb_mSbTe_{2+m}$ (LAST) system [Hsu et al, 2004], which has been mentioned in Chapter 2.3. Kanatzidis' group is mainly responsible for the development of this method.

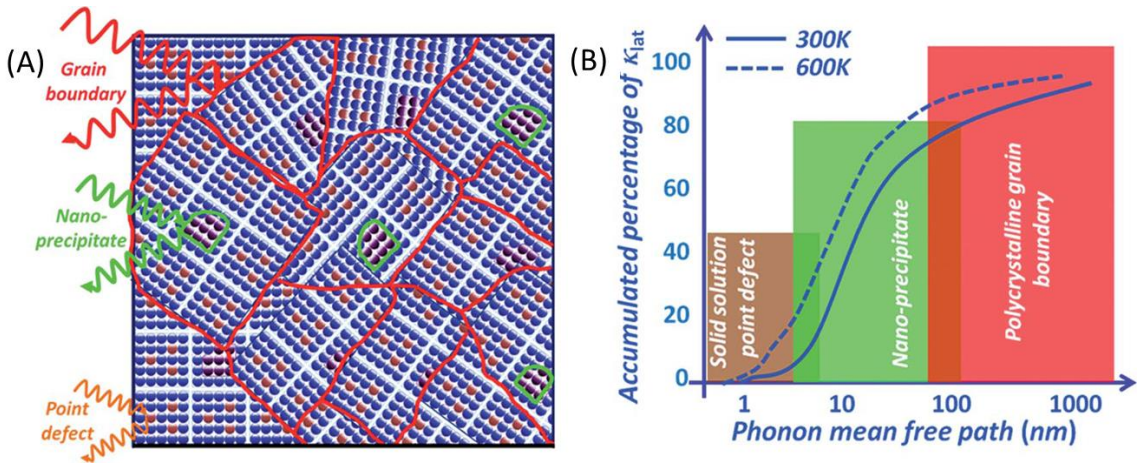

Figure 2.6. All-scale hierarchical architectures and lattice thermal conductivity: (A) all-scale hierarchical architectures, and (B) cumulative distribution function of lattice thermal conductivity with respect to the phonon mean free path in Si or PbTe bulk. [Adapted from reference Zhao et al, 2014]

Later on, his group brought up the idea of all-scale hierarchical architectures to scatter different mean free path of phonons (Figure 2.6): alloying defects to scatter short mean free path phonons, nanoprecipitates to scatter mid-long mean free path phonons and grain boundaries to scatter long mean free path phonons, which leads to the lowest possible thermal conductivity. In the light of the idea, his group published large number of high qualities papers on different matrix materials with varies of second minority phase, such as PbTe [Biswas et al, 2011a; Ahn et al, 2010; Biswas et al, 2011b], PbSe [Zhao et al, 2013; Lee et al, 2013] and PbS [Zhao et al, 2012a; Zhao et al, 2011a; Zhao et al, 2012b].

In conclusion, precipitation from solid solution has been extremely successful since the unique materials system can minimize the negative effect on electron transport. The disadvantages include high temperature, energy intensive, time consuming.

2.4.4 Solution Synthesis

Recently, solution synthesis of nanoparticles starts to get more attention because of its low reaction temperature, short reaction time and delicate control on morphology and size [Zhao et al, 2011b]. In solution synthesis, atoms are assembled to form nuclei and surfactants or templates are used to confine the growth of nuclei in the range of nanoscale. Popular ways in solution synthesis are hydro- and solvo-thermal reaction [Wang et al, 2005a; Wang et al, 2005b; Mi et al, 2007], electrochemical deposition [Martín-González et al, 2003; Wu et al, 2002; Zhang et al, 2010], sonochemical synthesis [Zhao et al, 2005] and ligand-based synthesis [Foos et al, 2001; Kovalenko et al, 2010; Urban et al, 2007]. Both electrochemical deposition and sonochemical synthesis suffer from the limited scalability because electrochemical deposition needs templates and sonochemical synthesis is very sensitive to frequency and intensity of ultrasound [Zhao et al, 2011b].

Hydro- and solvo-thermal synthesis is a simple and scalable way but its reproducibility and safety issues are concerns when applying this method. Finally, compared to the last three methods, ligand-based synthesis seems to be a better way to go, because the reaction happens at atmosphere pressure and can be scaled up without limitation from templates or reaction conditions. Meanwhile, the ligand-based synthesis also possesses advantages over the vapor deposition, mechanical alloying and milling, precipitation from solid solution. First, the reaction can happen at a much lower temperature than solid state reaction; second, the reaction usually takes much less time than mechanical alloying or solid state reaction since solution phase reaction maximizes the interaction between precursors; last but not least, the reaction can be cost-efficient if cheap surfactants and reducing agents are used. Although possessing some obvious advantages over other methods of making nanostructured thermoelectric materials, several areas still needs development or improvement in ligand-based reaction: first, a simple and scalable method to synthesize a group of nanomaterials; second, a real demonstration of scalability of the ligand-based synthesis; third, an effective process to remove surfactants and improve relative density of nanocomposites; finally, a systematic study of temperature dependent thermoelectric properties and carrier concentration optimization.

2.5 Conclusion

In this chapter, I have introduced the benefits of nanostructured materials in enhancing *ZT*. Specifically, three popular theories: quantum confinement, energy filtering and phonon scattering are discussed in details and also related experiments were reviewed, which prove the predictions of theories. Basically, the conclusions made from the

fundamental physics and derivation in Chapter 1 and 2 serve as the guideline of materials synthesis and design in my graduate research. Especially, Chapter 2 is the motivation for me to research nanostructured materials in thermoelectrics. Moreover, I also briefly reviewed the popular methods of fabricating nanostructured materials, but each has its own limitations, such as energy and time consuming, scalability, economics and so on, which inspires the general goals for my graduate research: first, develop a general method to synthesize a group of promising nanomaterials for thermoelectrics; second, scale up the synthesis in order to make a real technological impact; third, design advanced materials system to fully take advantage of benefits from nanostructuring; four, fabricate centimeter nanocomposite and optimize their thermoelectric properties under the guidance from the first two chapters; Five, explore new applications of thermoelectrics. In the following chapters, I will discuss my thesis work and each chapter will summarize one of my projects.

CHAPTER 3. SYNTHESIS OF TE NANOWIRES AND CONVERSION TO Bi_2Te_3 NANOWIRES

3.1 Introduction

Our research aims at tackling the challenge of producing these thermoelectric nanomaterials in an economical yet scalable way so that the exceptional properties of these materials can be put into real application. We took the path of solution-phase reaction that has low reaction temperature and short reaction time and it also can be easily coupled with large-scale industrial practice. Among numerous thermoelectric materials, tellurides have the best historical *ZT* in a wide range of temperature [LaLonde et al, 2011a]. Our synthetic method provides a general route to large-scale synthesize a wide variety of high-quality telluride nanowire and delicate nanowire heterostructure. In this chapter, I will introduce our synthetic method, and particularly the synthesis of Te nanowire templates that later are used for conversion to different telluride nanowire and nanowire heterostructure. The results of this work have been published on Nanoscale, 2014 [Finefrock et al, 2014a].

3.2 Synthesis Procedure

The synthesis requires chemicals including TeO_2 (≥99%), polyvinylpyrrolidone (PVP) (molecular weight ~40 000), KOH (90%), N_2H_4 (98%) and $Bi(NO_3)_3 \cdot 5H_2O$ (98%) were purchased from Sigma Aldrich while ethylene glycol (≥99%) was purchased from VWR.

The large-scale (>800 ml) synthesis takes place in a 1 liter Chemglass CHEMRxnHUB reactor in which the jacket fluid is heated and cooled using a Huber high precision thermo-regulator.

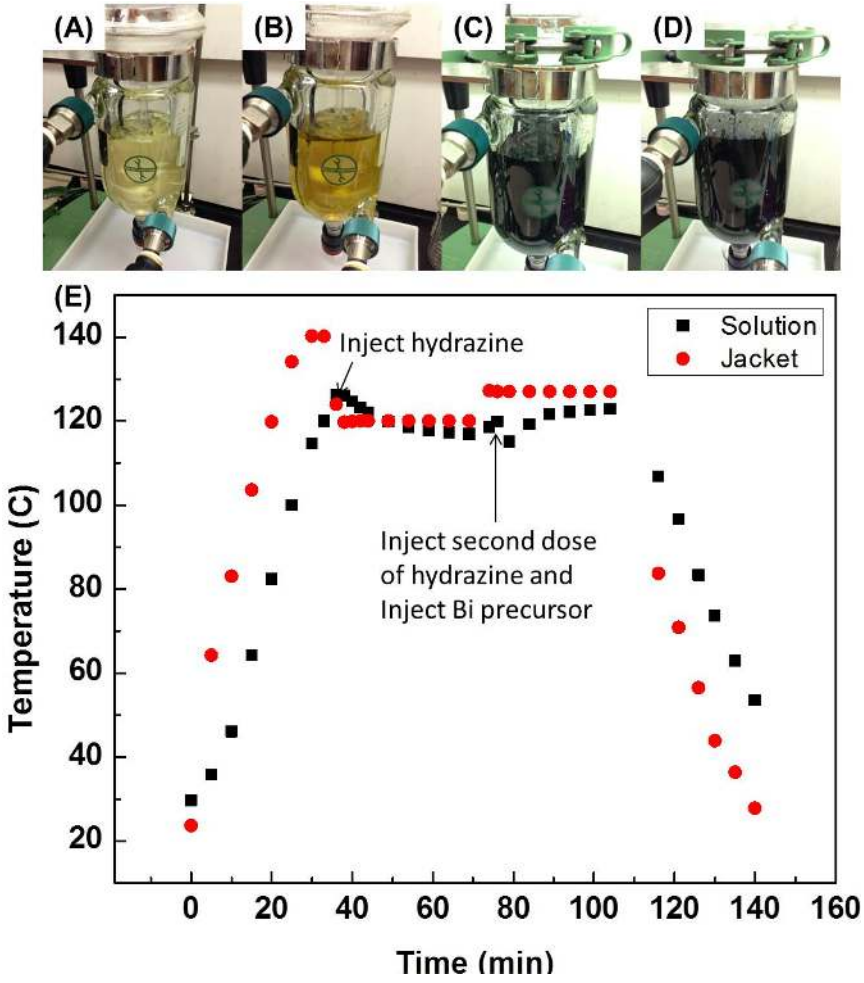

Figure 3.1. (A)-(D) show the color change at different time points in the reaction. (E) is the temperature profile of the reaction that includes both the reaction solution and heating fluid.

For the synthesis of Te nanowires and the conversion to Bi_2Te_3 nanowires, 23.30 g PVP, 11.17 g TeO_2 (70.0 mmol), 21 g KOH and ~700 ml ethylene glycol are added to the reactor. The jacket temperature setpoint is increased to above 120 °C and mechanical stirring is initiated; as the reaction mixture is heated, the colour changes from white/opaque to transparent yellow as shown in Figure 3.1A, B. When the reaction temperature reaches 120 °C, 18.7 ml N_2H_4 is rapidly injected, resulting in an immediate colour change from transparent yellow to opaque black (Figure 3.1C), and nitrogen protection is applied to the reactor via a Schlenk line. Minimal overshoot in temperature is observed in this step as show in Fig. 3.1E. As the Te nanowires form, a Bi precursor solution is made by dissolving 4.70 g PVP and 22.64 g $Bi(NO_3)_3 \cdot 5H_2O$ (46.7 mmol) in ~ 140 ml ethylene glycol by stirring on a 120 °C hot plate. 45 min after N_2H_4 injection, the Bi precursor solution is injected into the reaction mixture (Figure 3.1D) and another 18.7 ml N_2H_4 is also injected in the reaction solution. According to a previous report [Wang et al, 2011], the reaction mechanism is that Bi^{3+} can be reduced to Bi atoms that diffuse into the Te nanowires to form Bi_2Te_3 nanowires. The second dose of anhydrous hydrazine helps the reduction process and completes the conversion from Te to Bi_2Te_3 nanowires. 30 min after the Bi precursor injection, the jacket temperature setpoint is decreased to 20 °C. Then the product is collected by centrifuge and washed three times with deionized (DI) water and one time with ethanol for characterization.

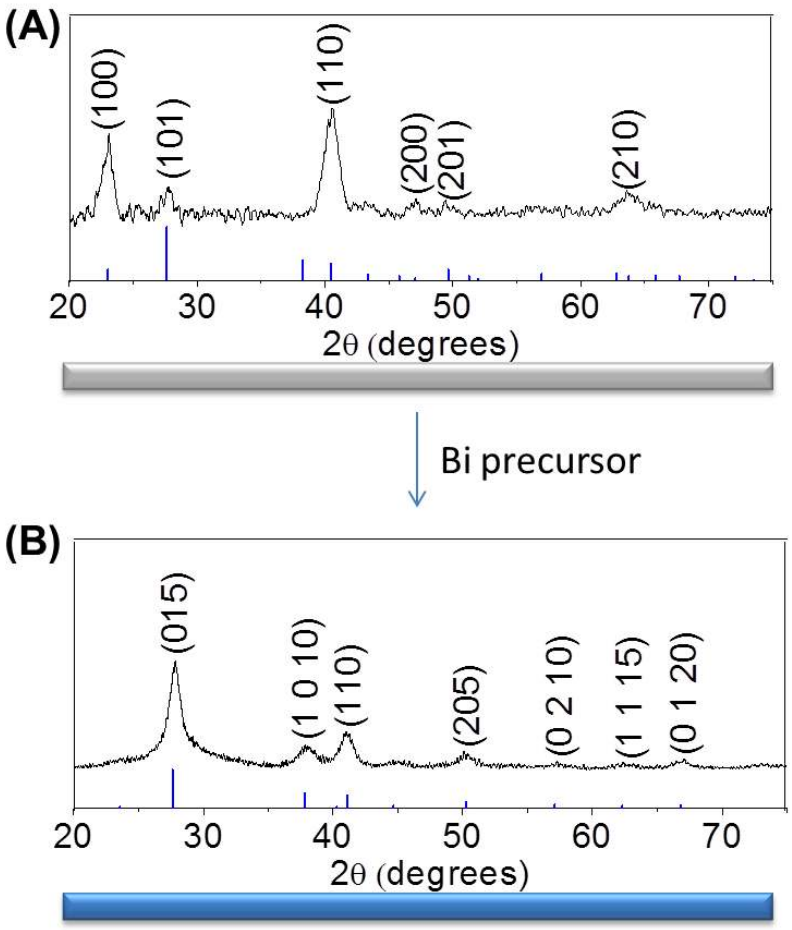

Figure 3.2. (A) is a scheme and XRD of Te nanowire. (B) is a scheme and XRD of Bi_2Te_3 nanowire.

3.3 Results of Materials Characterization

The Te and Bi_2Te_3 nanowires are first characterized by X-ray diffraction (XRD). As shown in Figure 3.2, the product in the first step (Figure 3.2A) and after the conversion (Figure 3.2B) can be readily indexed as pure Te (JCPDS no.35-1452) and Bi_2Te_3 phase (JCPDS no.15-0863) without any impurities identified, respectively.

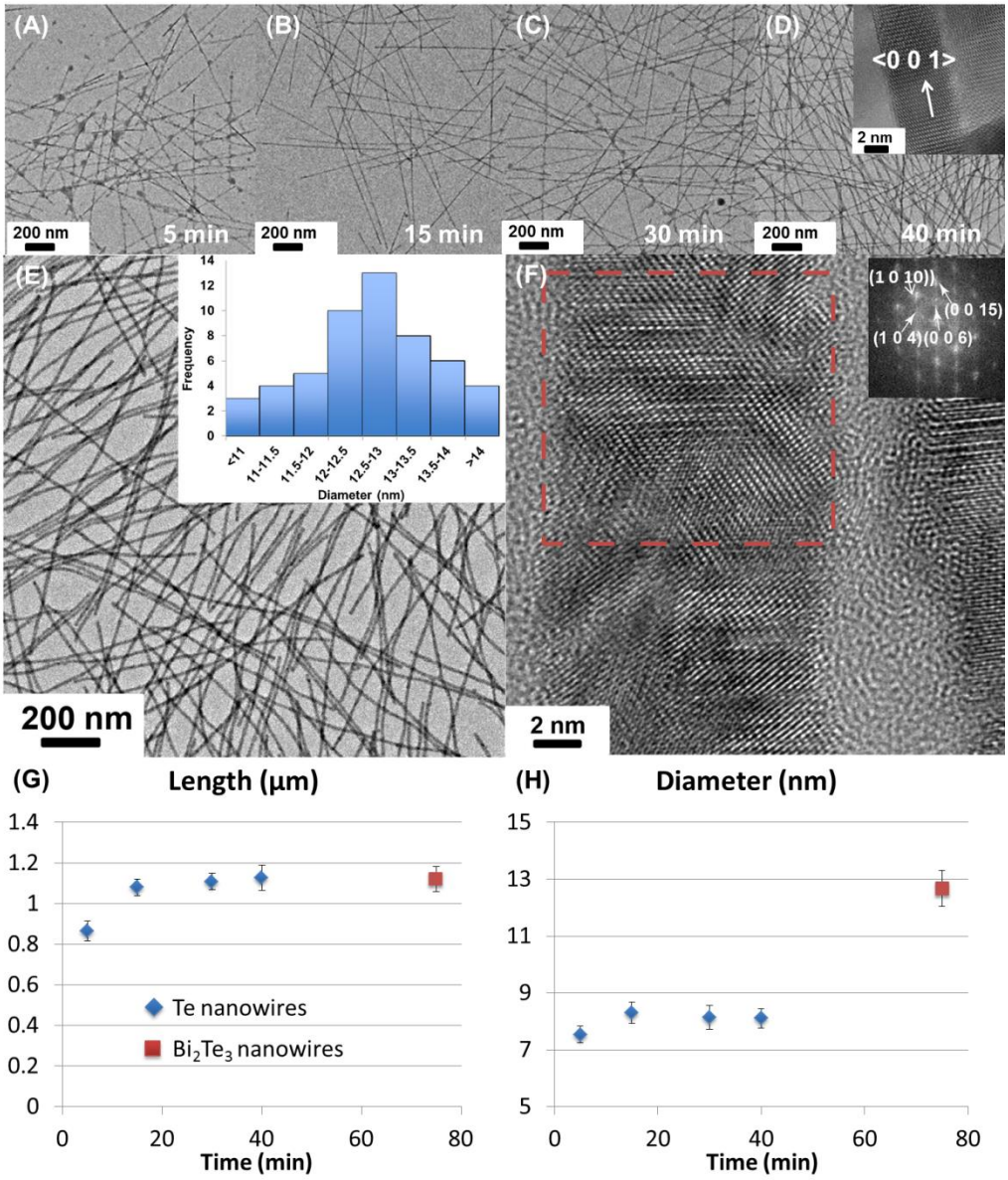

Figure 3.3. (A)-(D) show the TEM images of aliquots taken at different time points from the reaction solution; the inset of (D) is the HRTEM image of one Te nanowire. (E) is the low resolution TEM image of Bi_2Te_3 nanowires and the inset is the wire diameter distribution. (F) is the HRTEM image of one Bi_2Te_3 nanowire with the inset being the fast Fourier transformation (FFT) of the selected area. (G) is the wire length change with time and (H) is the diameter change with time.

The transmission electron microscope (TEM) studies on aliquots taken during the Te nanowire growth step show that Te rapidly grows one dimensionally even during the first

five minutes after N_2H_4 injection, (Fig. 3.3A). As the reaction proceeds, nanowire morphology is retained as shown in Fig. 3B–D. Length and diameter measurements of the Te nanowire aliquot images (Fig. 3G, H) reveal that most of the Te nanowire growth occurs during the initial fifteen minutes, with only small increases in length and diameter afterwards. High-resolution TEM (HRTEM) imaging of the Te nanowires (Fig. 3D inset) shows that the axial direction of the nanowires is the <001> direction. Overall we attribute the formation of ultrathin nanowires to the anisotropic crystal structure of Te [Song et al, 2008], radial growth passivation by PVP [Ying-Jie et al, 2006; Qian et al, 2006] and the use of at least 8 times excess hydrazine, which encourages rapid formation of many small nuclei, which then grow one dimensionally [Zhang et al, 2012b].

TEM analysis of the Bi_2Te_3 products (Figure 3.3E) shows that the original Te nanowire morphology is very well preserved during the Bi insertions step. Interestingly, the length of the Bi_2Te_3 nanowires is 1.121 ± 0.062 μm (Figure 3.3G), which is nearly identical to the length of Te nanowires (1.125 ± 0.062 μm) while the diameter of Bi_2Te_3 nanowires is 12.6 ± 1.1 nm (Figure 3.3H), which is increased compared to the diameter of Te nanowires (8.1 ± 0.3 nm), which indicates that Te nanowires act as templates that are sacrificed during Te to Bi_2Te_3 conversion. The HRTEM image (Figure 3.3F) actually shows that the Bi_2Te_3 nanowires are polycrystalline, which is different from another reported case of Te-template assisted synthesis of Bi_2Te_3 nanowires that are actually single crystalline with axial direction of <1 1 9> [Wang et al, 2011]. An FFT on the selected area (Figure 3.3F; inset) confirms the Bi_2Te_3 phase and shows the axial direction of <0 0 1>.

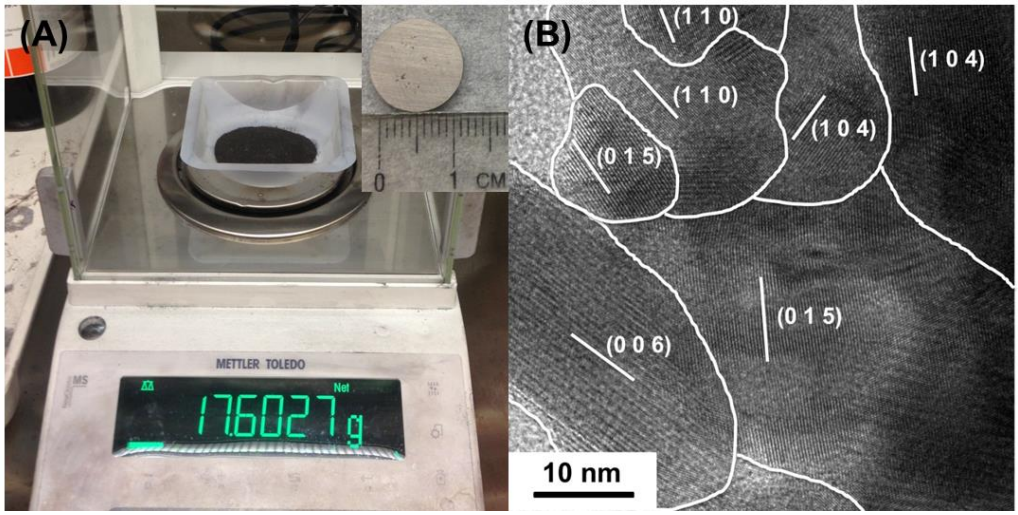

Figure 3.4. (A) shows the product from one batch on a balance; the inset of (A) is the picture of one hot pressed pellet. (B) is the HRTEM image of the cross section of the hot pressed pellet.

Table 3.1. The calculation of the yield of the large scale synthesis of Bi_2Te_3 nanowires.

Bi_2Te_3	Dried powder	Idea	Yield
Amount	17.6027g (21.982mmol)	18.6844g (23.333mmol)	94.21%

As-synthesized Bi_2Te_3 nanowires can be washed, stripped of the PVP surfactants, and vacuum dried using our previously published procedure [Zhang et al, 2011b]. The resulting material can then be ground into a fine powder and weighed to determine the overall reaction yield (Figure 3.4A). As described in Table 3.1, greater than 17 grams of Bi_2Te_3 nanowire powder is produced per batch. Given theoretical yields determined by the weights of the starting precursors, the yields of our reactions can even exceed 94%. The washed and dried nanowire powder can be hot pressed into centimeter-sized discs with high relative density (~90%) and good structural integrity as shown in the upper

insets of Figure 3.4A. HRTEM analysis of hot pressed Bi_2Te_3 nanowires reveals nanoscale grains of only Bi_2Te_3 (Figure 3.4B). The well-preserved nanoscale grain boundaries with random orientation in both materials could significantly enhanced phonon scattering to lower the thermal conductivity and improve the isotropy for in-plane and cross-plane electrical and thermal property measurements.

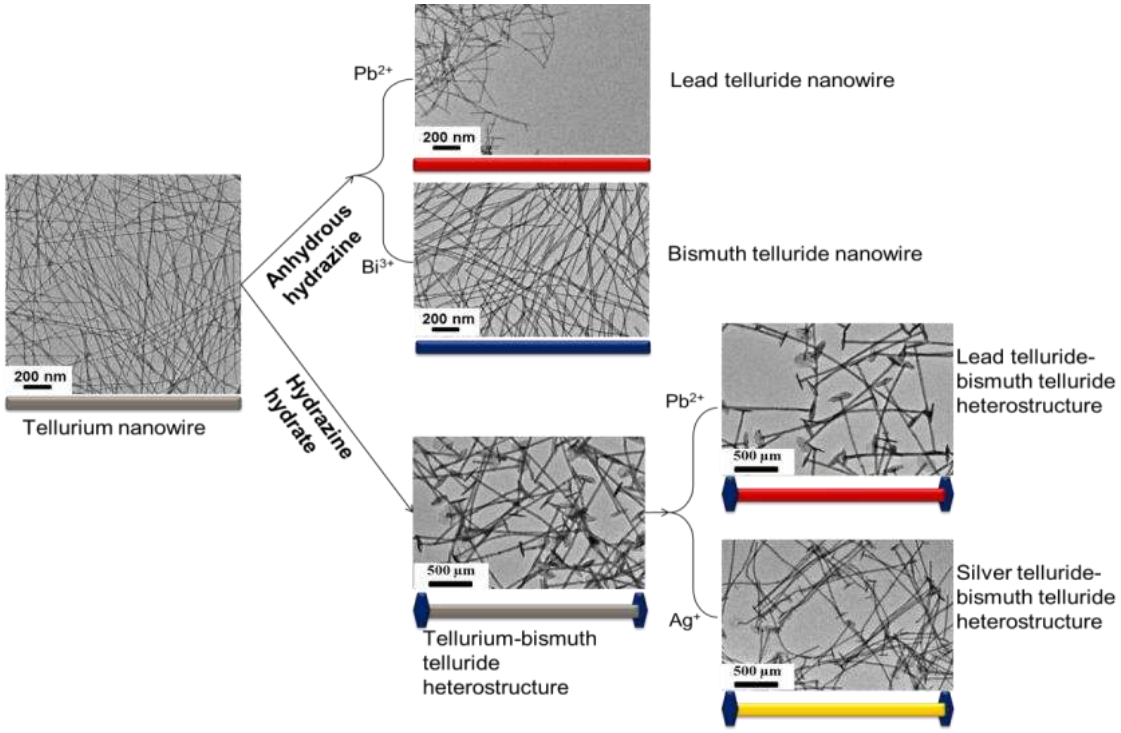

Figure 3.5. A conclusion of the telluride nanowires and nanowire heterostructures synthesized during my graduate research. This is also a demonstration of the flexibility of our synthetic method.

3.4 Overview of Our General Strategy

The conversion to Bi_2Te_3 nanowires from Te nanowires is just an example to demonstrate our synthetic method. As a matter of fact, by injecting different cation precursor in the

second step, different tellurides nanowire can be synthesized, such as PbTe [Finefrock et al, 2014a] and Ag_2Te [Yang et al, 2014] nanowires. Through reducing the concentration of reducing agent, hydrazine, in the reaction, a partial conversion to Bi_2Te_3 plates at the two ends of Te nanowires can be accomplished [Zhang et al, 2012b]. Afterwards, center Te nanowire of the partially converted Te-Bi_2Te_3 heterostructure can be further converted into other tellurides such as PbTe [Fang et al, 2013] and Ag_2Te [Fang et al, 2014a]. Figure 3.5 summarizes the telluride nanowires and nanowire heterostructures I have synthesized in my graduate research, which demonstrates the flexibility of our general synthetic method. Afterwards, as schemed in Figure 3.6 the dried powder of these nanoparticles is consolidated into bulk pellets composed of nanograins on which the thermoelectric properties are measured.

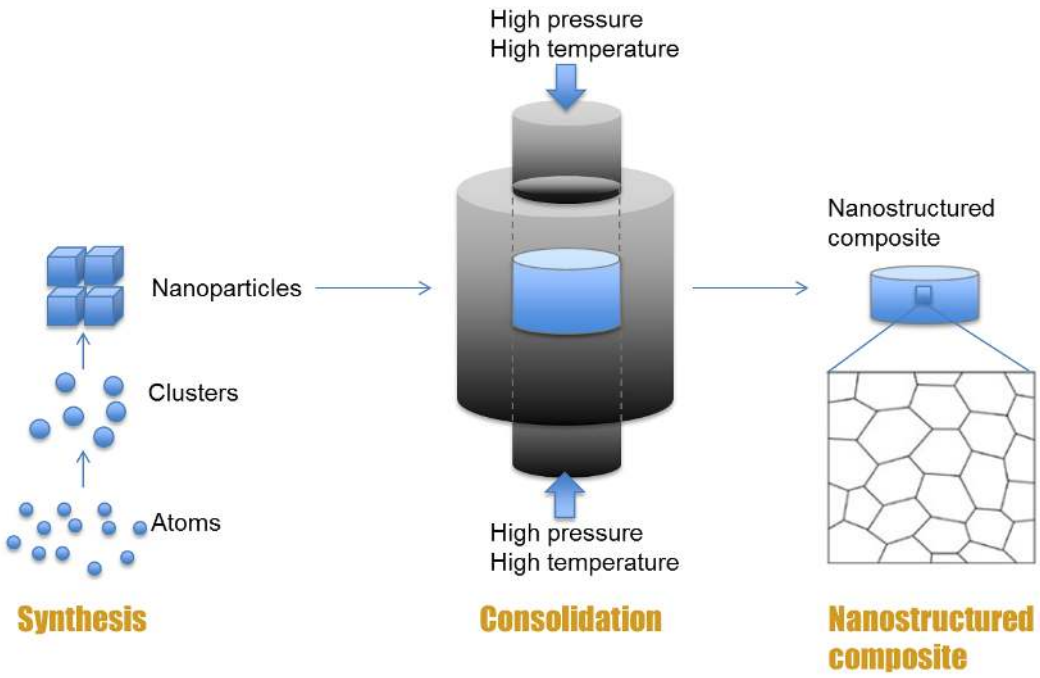

Figure 3.6. A schematic demonstration of our general strategy of making nanostructured composite from solution synthesized nano-powder.

3.5 Conclusion

In conclusion, we have developed a simple and general method to synthesize Te and Bi_2Te_3 nanowires, the success of which was confirmed by XRD and TEM. A large scale reaction was demonstrated in a 1 liter reactor and over 17 g Bi_2Te_3 nanowires can be obtained at a yield of 94%. Basically, the synthesis of Te nanowire lays the foundation of graduate research. Other than Bi_2Te_3 nanowires, a group of other tellurides can be synthesized as well. In the following chapters, I will discuss in more details about the synthesis and characterization of those tellurides in Figure 3.5 and also their thermoelectric properties optimization. As some of the knowledge and theories that will be applied in the following discussion have been introduced in the first two chapters, the conclusions made in the first two chapters will be directly used to explain our materials properties without further interpretation.

CHAPTER 4. AN INVESTIGATION OF Se DOPING EFFECT ON THERMOELECTRIC PROPERTY OF Bi_2Te_3 NANOCOMPOSITE

The thermoelectric properties of Bi_2Te_3 nanocomposite pellet made from as-synthesized Bi_2Te_3 nanowires are mediocre, because the carrier concentration, measured by Hall Effect, is higher than the optimal value. A third element, Se, is introduced to dope the nanocomposite, which improves the *ZT* and also gives us the chance to investigate how the carrier concentration can influence the thermoelectric properties of Bi_2Te_3 nanocomposite. Due to the Se doping, the room temperature power factor increases by 60%. Detailed material characterization and semiconductor parameter measurement, e.g. carrier concentration and mobility, helped explaining the thermoelectric performance improvement. At the same time, theoretical calculation is also done to establish fundamental understanding of the material system. The results of this work are in preparation for publication within 2014.

4.1 Introduction

Bismuth telluride (Bi_2Te_3) based materials have the best thermoelectric figure of merit ($ZT=S^2\sigma T/\kappa$) near room temperature, where S is Seebeck coefficient, σ is electrical conductivity, κ is thermal conductivity and T is absolute temperature. Historical ZT values of single-crystalline Bi_2Te_3 ingots alloyed with Sb (p-type) and Se (n-type) are

around 1 [Yim et al, 1972; Carle et al, 1995; Yamashita et al, 2003]. In the past 10 years, researchers began to fabricate nanostructured Bi_2Te_3 that is proven to be able to enhance ZT through reducing thermal conductivity. The most cited examples are that Bi_2Te_3/Sb_2Te_3 and $Bi_2Te_3/Bi_2Te_{2.83}Se_{0.17}$ superlattice thin films achieved ZT of 2.4 and 1.4, respectively [Venkatasubramanian et al, 2001] and $Bi_{0.5}Sb_{1.5}Te_3$ nanostructured bulk reached ZT of 1.4 [Poudel et al, 2008]. The great success stimulates researchers' efforts in nanostructured materials. However, complex high-vacuum molecular beam epitaxy and energy-intensive ball milling were involved in fabricating those materials. Therefore, solution synthesis of Bi_2Te_3 nanoparticles, as an alternative path that is easier and more energy-efficient, is passionately pursued by researchers. R. J. Mehta et al reported that solution synthesized n-type Bi_2Te_3 and p-type $Bi_{0.5}Sb_{1.5}Te_3$ nanoplates achieved ZT of 1.1 and 1.2 repectively, which is the most successful effort so far in solution synthesized Bi_2Te_3 nanoparticles [Mehta et al, 2012]. Recently, our group reported a 1 liter scale synthesis which can produce over 17 gram of Bi_2Te_3 nanowires at an impressive yield of 94.21 % [Finefrock et al, 2014a]. Herein, we reported thermoelectric performance optimization of the consolidated pellets of Bi_2Te_3 nanowires and insightful analysis of the thermoelectric properties.

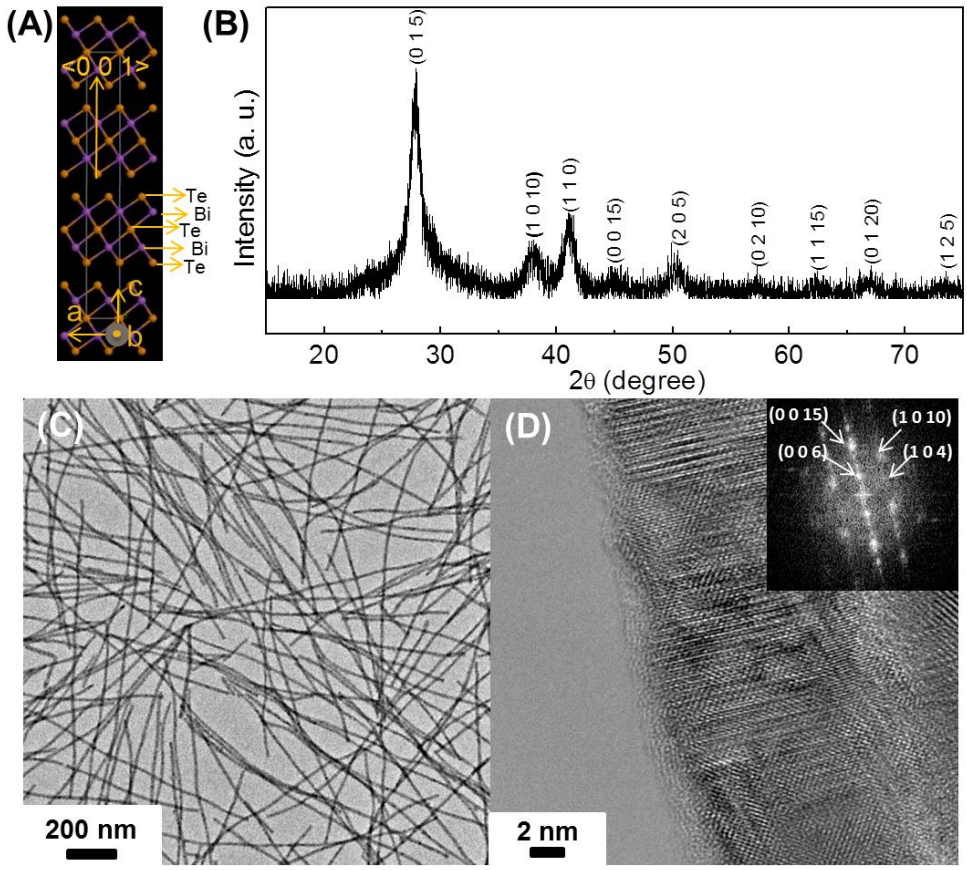

Figure 4.1. (A) is a scheme of Bi_2Te_3 lattice; the picture is from Jmol (an open-source Java viewer for chemical structures in 3D; http://www.jmol.org/). (B) is the XRD of as-synthesized Bi_2Te_3 nanowires. (C) is the low resolution TEM image of Bi_2Te_3 nanowires and (F) is the HRTEM image of one Bi_2Te_3 nanowire with the inset being the FFT of the selected area.

Bi_2Te_3 has a layer lattice structure and the configuration of one quantum layer is Te(1)-Bi-Te(2)-Bi-Te(1) (Figure 4.1A). Te(1) and Bi is covalently bonded while adjacent quantum layers are loosely bonded thorough Van der Waals force [Drabble et al, 1958; Mishra et al, 1997]. Due to the unique crystal structure, the defect chemistry of Bi_2Te_3 is quite complicated. Te vacancy is one of the most common defects existing in Bi_2Te_3. Since Te (52.55 kJ/mol) has a smaller evaporation energy than Bi (104.80 kJ/mol), Te tends to evaporate more than Bi during high temperature consolidation or annealing

treatment [Liu et al, 2011]. Te vacancy can donate two free electrons according to equation: $Te_{Te} = V_{Te}^{2+} + Te + 2e^{-}$, which significantly increases n-type conductance [Schultz et al, 1962; Hyun et al, 2001; Jiang et al, 2005]. Due to the small electronegativity difference between Bi and Te [Scanlon et al, 2012], defect of Bi in Te site (Bi_{Te}) or Te in Bi site (Te_{Bi}) is also widely found in literature. The formation of Bi_{Te} antisite follows equation: $Bi + Te_{Te} = Bi_{Te}^{-} + Te + h^{+}$ and donates one free hole to Bi_2Te_3 per site [Starý et al, 1988; Jia et al, 2011; Fuccillo et al, 2013]. Te_{Bi} antisite, one the other hand, donates one free electron to Bi_2Te_3 per site following equation: $Te + Bi_{Bi} = Te_{Bi}^{+} + Bi + e^{-}$ [Scanlon et al, 2012; Jia et al, 2012]. Recent reports show that the Seebeck coefficient of Bi_2Te_3 nanowire is much lower than bulk mainly due to higher electron carrier concentration contributed by defects easier formed in Bi_2Te_3 nanowire probably because of dangling bonds on large surface area [Mavrokefalos et al, 2009; Chen et al, 2010; Shin et al, 2014]. We also found that the consolidated pellet of our large-scale synthesized Bi_2Te_3 nanowires have extremely high electron carrier concentration which leads to mediocre thermoelectric performance. To reduce the carrier concentration, Se was used as dopant to occupy double-charged Te vacancy and compensate free electrons. However, more Se addition potentially creates single-charged Se_{Bi} or Te_{Bi} antisite that donates free electrons and increases electron carrier concentration again. The well-engineered carrier concentration extracts the maximum thermoelectric performance from Bi_2Te_3 nanowire pellets.

4.2 Pellets Preparation

The synthesis of Bi_2Te_3 nanowires exactly follows the procedure of our previously published paper on the large scale production of Bi_2Te_3 nanowires [Finefrock et al, 2014a]. After the as-synthesized Bi_2Te_3 nanowires are washed with deionized (DI) water three times, they are re-dispersed and stirred overnight in hydrazine aqueous solution composed of 90% of water and 10% of hydrazine hydrate solution (80%) in order to get rid of surfactants on the nanowires. Then, the Bi_2Te_3 nanowires are washed with 3 times with DI water and 1 time with ethanol before dried completely in vacuum and annealed at 450 °C for half an hour. Afterwards, the Bi_2Te_3 nanowires lumps are ground into fine power in a glovebox with nitrogen protection and then Se powder is thoroughly mixed with the nanowires by grinding. Finally, the mixture is consolidated into centimeter pellets with hot press at 450 °C for half an hour.

4.3 Results of Materials Characterization

The as-synthesized Bi_2Te_3 nanowires are characterized XRD and TEM (Figure 4.1). The spectrum of the nanowires can be readily indexed as Bi_2Te_3 (JCPDS No. 15-0863) without any impurity peaks identified (Figure 4.1B). The low resolution TEM image shows the morphology of nanowires with uniform distribution (Figure 4.1C). The lattice resolved image of the nanowire was obtained with high resolution TEM (Figure 4.1D), which reveals the polycrystalline nature of a single nanowire while the FFT can indexed as pure Bi_2Te_3 phase. More discussion on the Bi_2Te_3 nanowire characterization can be found in our previous report [Finefrock et al, 2014a].

Table 4.1. A summary of the relative density, Se atomic percentage and chemical formula of all the samples identified by numbers from 1 to 7.

Sample ID	Relative density (%)	Se atomic %	$Bi_2Te_xSe_y$
1	92.42	0	$Bi_2Te_{2.62}$
2	92.81	1.52 ± 0.34	$Bi_2Te_{2.62}Se_{0.07}$
3	92.49	3.91 ± 0.68	$Bi_2Te_{2.64}Se_{0.19}$
4	90.57	5.66 ± 0.58	$Bi_2Te_{2.57}Se_{0.27}$
5	90.44	8.20 ± 0.97	$Bi_2Te_{2.51}Se_{0.4}$
6	91.95	11.54 ± 0.68	$Bi_2Te_{2.42}Se_{0.58}$
7	91.34	17.71 ± 0.38	$Bi_2Te_{2.14}Se_{0.89}$

A total of 7 pellets with different Se concentrations were fabricated for carrier concentration optimization. First, the densities of Bi_2Te_3 nanocomposite pellets with different Se concentrations were calculated from mass and geometry and the theoretical density of Bi_2Te_3 was used for the relative density calculation. The results listed in Table 4.1 indicate that all of the pellets possess high relative densities over 90%. Furthermore, Se concentration in each pellet was measured with EDS whose error bars come from the geometrical distribution of Se (Table 4.1). The corresponding chemical formula based on the EDS results for each pellet is also summarized in Table 4.1.

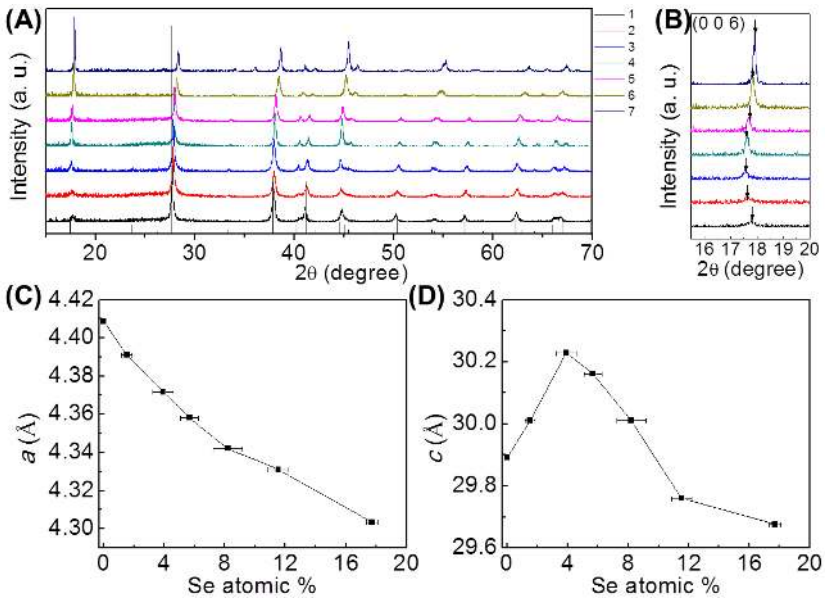

Figure 4.2. (A) is a summary of the XRD spectra of all 7 samples and the spikes is the standard spectrum of Bi_2Te_3 (JCPDS No. 15-0863). (B) is the zoom-in view of the (0 0 6) peak. (C) and (D) are the change of calculated lattice constants *a* and *c* with Se atomic percentage.

Notably, the Se concentration has a significant impact on the XRD spectra of the pellets. Generally speaking, Te and Se are in the same group in the periodic table but Se has a smaller atomic radius than Te. Therefore, the Se doping would decrease the lattice constants and cause the XRD peaks shift to higher angles according to the Bragg equation ($\sin\theta = n\lambda/2d$). The initial observation on the XRD spectra (Figure 4.2A) confirms that the XRD peaks shift to higher angles as Se concentration increases. Moreover, the calculated lattice constant *a* from the XRD spectra show a decreasing trend with Se concentration (Figure 4.2C). However, if taking a closer look at the variation of (0 0 6) peak positions with Se concentration (Figure 4.2B), which is solely determined by the *c* constants, one can notice that the (0 0 6) peaks first shift to a lower angle and then to a higher angle. The calculated lattice constant c corresponds to the (0 0 6) peak shifting and

reaches the maximum value (30.229 Å) that is, of course, still smaller than that of pure Bi_2Te_3 (30.483 Å) at the Se concentration of 3.91%. Combining the EDS results (Table 4.1) and the fact that *a* monotonically decreases while *c* first increases and then decreases with the Se concentration, we proposed a plausible Se doping mechanism that can interpret the lattice constants as well as the carrier concentration variation with Se concentration that was measured later on. Sample 1 made from pure Bi_2Te_3 nanowires is Te deficient (Table 4.1), which means lots of Te vacancies exist in the lattice. As discussed previously (Figure 4.1A), since Bi_2Te_3 has a layer lattice structure, the Te vacancies means some Te atomic layers are missing in the lattice, which leads to a smaller *c* constant (29.891 Å) than that of perfect Bi_2Te_3 (30.483 Å), whereas the *a* constant (4.409 Å) is slightly higher than that of perfect Bi_2Te_3 (4.385 Å) because Bi has a slighter larger atomic radius than Te. When Se is doped into the Bi_2Te_3 pellets, Te vacancies are occupied by Se so that the layer structure is stretched along *c* direction, leading to a larger *c* constant. However, the *a* constant becomes smaller because Se has a much shorter atomic radius than Bi and Te. As Se concentration continues increasing until 3.91%, the *c* constant starts to decrease while *a* constant keeps going down. At this point, Se not only fills the Te vacancies but also starts occupying the Bi atomic layers to form Se_{Bi} antisites, probably because of the defect formation energy of Se_{Bi} antisites becomes favorable with richer Se or poorer Bi [Scanlon et al, 2012]. Again, due to the atomic radius difference between Bi and Se, the layer structure shrinks in *c* direction, leading to a decreasing *c* constant, while *a* constant keeps its decreasing trend. To summarize, through analyzing the variation of *a* and *c* lattice constants with Se

concentration, we discussed a plausible Se doping mechanism that in fact can also explain the change of carrier concentration with Se concentration as well.

4.4 Influence of Se Concentration on Thermoelectric Properties

To investigate the thermoelectric properties, the 7 pellets are cut and polished into required dimensions. Seebeck coefficient is measured in home built system by bridging the sample between a heater and heat sink and testing the voltage and temperature difference between the hot and the cold sides in a vacuum chamber. Electrical conductivity is measured with Van der Pauw method in a system where a MMR K-20 temperature stage is used to control sample temperature and an Agilent is connected to provide source current and collect voltage signals. Hall Effect is carried out by applying magnetic field up to 1 Tesla to the electrical conductivity measurement system. Thermal conductivity is calculated via the equation $\kappa = \alpha\rho Cp$ (ρ is the density) and the thermal diffusivity (α) is measured through the laser flush method. All the measurements are carried out under vacuum in the temperature range from 300 to 500 K.

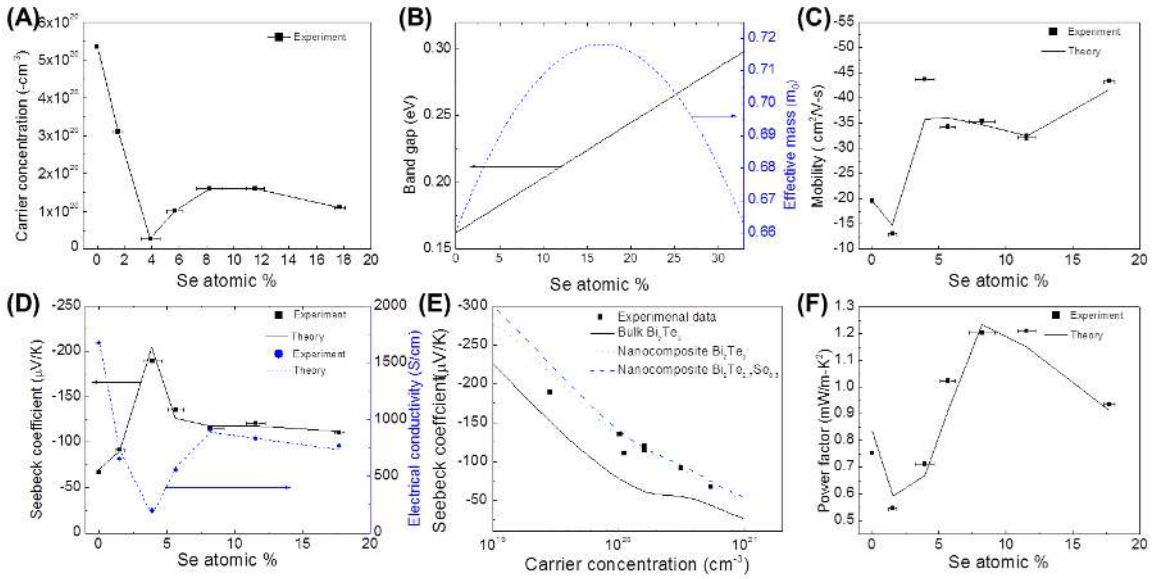

Figure 4.3. Influence of Se concentration on thermoelectric properties. (A) Carrier concentration; (B) the theoretical calculation result of band gap and effective mass; (C) Mobility; (D) Seebeck coefficient and electrical conductivity; (E) Pisarenko relation (Seebeck coefficient v.s. carrier concentration); (F) power factor.

Figure 4.3 gives a clear picture of how Se concentration influences the thermoelectric properties of the samples at 300 K. As discussed previously, the each Te vacancy donates two electrons, so Sample 1 has an extremely high carrier concentration of 5.36×10^{20} cm^{-3} (Figure 4.3A). When doped into the system, Sample 2 and 3 possess reduced carrier concentration because Se fills the Te vacancy and compensates the two free electrons: $Se + V_{Te}^{2+} + 2e^{-} = Se_{Te}$, which decreases carrier concentration in the materials. The Se doping efficient is calculated to be 0.45 electrons per Se atom from the results of Sample 1 – 3. Interestingly, the carrier concentration reaches a minimum value of 2.84×10^{19} cm^{-3} in Sample 3 and then start to increase, which exactly corresponds to the crest point of *c* constant (Figure 4.2D). As discussed in the Se doping mechanism, Se

occupies the Bi site, which can donate one free electrons to the system according to the equation: $Se + Bi_{Bi} = Se_{Bi}^{+} + Bi + e^{-}$. The Se doping efficient is calculated to be 0.11 electrons per Se atom from the results of Sample 3 – 5. As Se concentration continues increasing, Sample 6 has almost identical carrier concentration as Sample 5 at 1.60×10^{20} cm^{-3} whereas the carrier concentration of Sample 7 drops to 1.10×10^{20} cm^{-3}. As a matter of fact, the band gap of $Bi_2Te_{3-x}Se_x$ increases linearly from 0.16 eV at 0% Se to 0.245 eV at 20% Se [Neuberger et al, 1966] (Figure 4.3B). A wider band gap leads to a lower carrier concentration, which acts as a counter-effect to the doping effect of Se_{Bi} antisites, which could probably explain the unusual trend where the carrier concentration possesses a wide plateau (3.34%) before a relatively small drop when Se concentration increases by as significant as 6.17%. Figure 4.3C plots the mobility of the 7 samples at 300 K, which reveals a few important points. First, the magnitude of the mobility is in the range from 12 to 45 $cm^2V^{-1}s^{-1}$ that is comparable to some other solution synthesized $Bi_2Te_{3-x}Se_x$ nanocomposite [Son et al, 2012; Zhao et al, 2010; Soni et al, 2012] and thin films [Yoo et al, 2005; Kim et al, 2006; Boulouz et al, 1998] but smaller than most mechanical alloyed [Yang et al, 2000; Liu et al, 2011] and single crystalline $Bi_2Te_{3-x}Se_x$ [Carle et al, 1995] that have mobility from 100 to 250 $cm^2V^{-1}s^{-1}$. Second, our theoretical calculation implies that a scattering parameter (r) of 0.8 is needed to fit the mobility and later the Seebeck coefficient, compared to the much smaller scattering parameter found in bulk (r = -0.3), which is due to the boundaries/defects and porosity (~9%) found in our samples. Third, Sample 2 has lower carrier concentration and mobility simultaneously than Sample 1, which does not follow the common trend that mobility increases with carrier

concentration. The reduced mobility here is actually due to the increasing effective mass upon Se alloying in the range between 0 and 16% (Figure 4.3B) [Goldsmid, 2010b].

The influence of Se concentration on Seebeck coefficient and electrical conductivity at 300 K is shown in Figure 4.3D. All 7 samples have negative Seebeck coefficients that indicate their n-type nature. The Seebeck coefficient generally follows Mott equation that predicts higher carrier concentration leads to lower Seebeck coefficient (Figure 4.3D) [Goldsmid, 2010a, Cutler et al, 1969]. The highest Seebeck coefficient (-189 μV/K) was achieved at the Se concentration of 3.91% that corresponds to the carrier concentration of 2.84×10^{19} cm^{-3} while the lowest Seebeck coefficient is -67 μV/K measured in Sample 1 with the carrier concentration of 5.36×10^{20} cm^{-3} (Figure 4.3D). A theoretical study was performed to calculate the Pisarenko relation (carrier concentration v.s. Seebeck coefficient). As shown in Figure 4.3E, the Seebeck coefficients of all 7 samples distribute slightly above the bulk curve, which means our nanocomposites possess higher Seebeck coefficients than bulk at the same carrier concentration. The enhancement of Seebeck coefficients are from the elevated electron scattering in nanocomposites. After the scattering parameter is increased from -0.3 to 0.8, the theoretically predicted Pisarenko relation can fit well with the experimental results (Figure 4.3E). The electrical conductivities of all 7 samples at 300 K are also shown in Figure 4.3D. Basically, the electrical conductivity follows the same trend with Se concentration as the carrier concentration. The highest electrical conductivity is 1675 S/cm in Sample 1 while the lowest electrical conductivity is 198 S/cm obtained at the Se concentration of 3.91% in Sample 3. Overall, the mobility of our samples leads to smaller electrical conductivity

than those of mechanical alloyed [Yang et al, 2000; Liu et al, 2011] or single crystalline $Bi_2Te_{3-x}Se_x$ at the same carrier concentration [Carle et al, 1995]. However, the electrical conductivities of our samples have an edge over some other solution synthesized $Bi_2Te_{3-x}Se_x$ nanocomposites [Son et al, 2012; Zhao et al, 2010; Soni et al, 2012]. Further improvement on electrical conductivity can be achieved by increasing the mobility of our samples, which will be discussed later.

Based on the Seebeck coefficient and electrical conductivity at 300 K, the power factor was calculated and plotted out in Figure 4.3F. It turns out that the optimal power factor is ~1.2 mW/m-K^2 obtained between the Se concentration of 8.2% and 11.54% that corresponds to the carrier concentration of ~1.60×10^{20} cm^{-3}. The mechanical alloyed $Bi_2Te_{3-x}Se_x$ cited here [Yang et al, 2000; Liu et al, 2011] can achieve optimal power factor at carrier concentration of 1.50×10^{19} cm^{-3} and 2.28×10^{19} cm^{-3}, respectively, which are smaller than the optimal value in our samples by one order of magnitude. It is due to the smaller mobility in our sample that makes the optimal carrier concentration shifts to a higher value [Goldsmid, 2010b]. Meanwhile, another case of solution synthesized $Bi_2Te_{3-x}Se_x$ nanocomposite claims that the optimal power factor is obtained at carrier concentration of 7.8×10^{20} cm^{-3} and the corresponding mobility is 1.33 $cm^2V^{-1}s^{-1}$ [Soni et al, 2012].

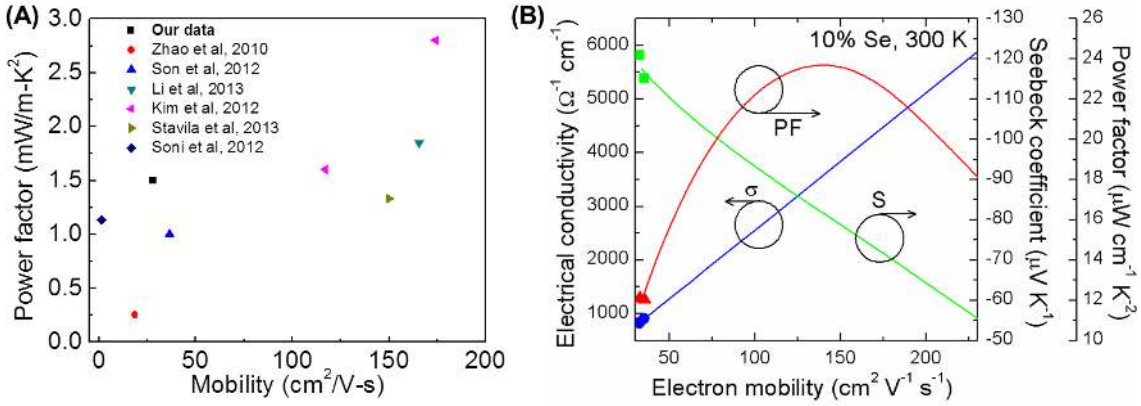

Figure 4.4. (A) is a comparison between our best power factor and mobility with other historical values. (B) is a theoretical prediction of the Seebeck coefficient, electrical conductivity and power factor with an increasing mobility.

Figure 4.4A displays the historical data of power factor (y axis) and mobility (x axis) of solution synthesized $Bi_2Te_{3-x}Se_x$ nanocomposites, but please notice that only the papers reporting both power factor and mobility are included here. Our sample possesses a better power factor than other values at low mobility end and even one value at high mobility end, which is due to the well engineering of carrier concentration. However, in general the power factors at high mobility end are better than ours. Therefore, we applied theoretical calculation to predict the power factor enhancement given better mobility and the results show that the best power factor reaches 2.4 mW/m-K^2 if the mobility could be as high as 150 $cm^2V^{-1}s^{-1}$ (Figure 4.4B). Experimentally, the enhancement of mobility can be realized by increase hot pressing time, annealing or growing thicker Bi_2Te_3 nanowires. The research is underway for further improvement of power factor.

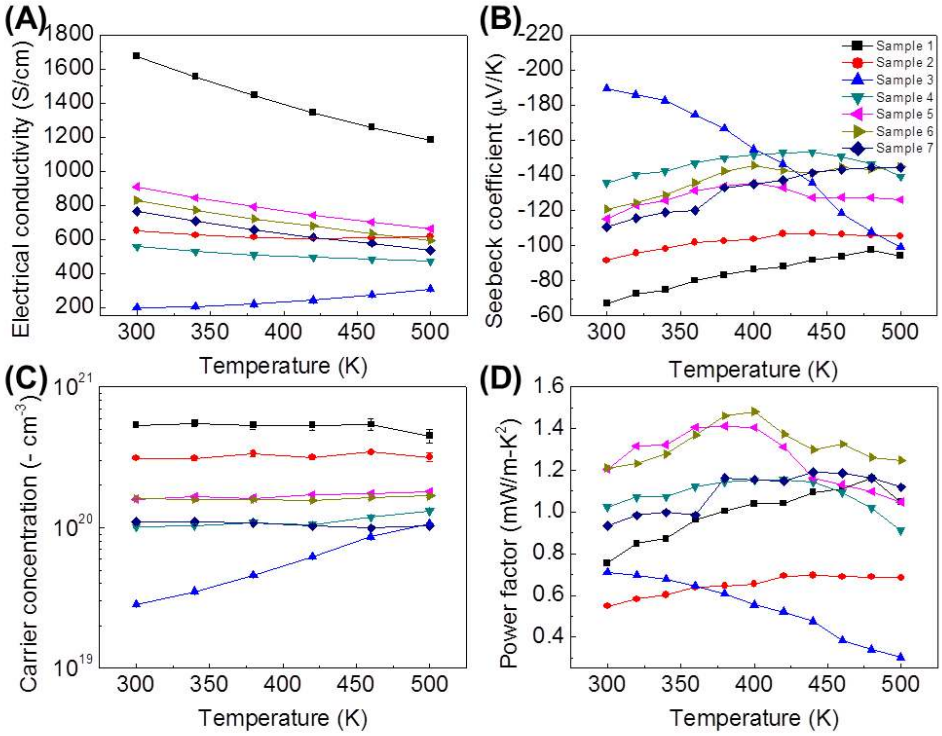

Figure 4.5. The temperature dependent thermoelectric properties. (A) electrical conductivity; (B) Seebeck coefficient; (C) carrier concentration; (D) power factor.

4.5 Temperature Dependent Thermoelectric Properties

Figure 4.5 shows the temperature dependent thermoelectric properties of $Bi_2Te_{3-x}Se_x$ nanocomposites with different Se concentration. On one hand, the negative temperature dependent behavior of electrical conductivity of almost all samples indicates they are degenerate semiconductors (Figure 4.5A). On the other hand, the electrical conductivity of Sample 3 increases with temperature, which is due to its lowest carrier concentration at 300 K and increasing carrier concentration at elevated temperatures (Figure 4.5C). Meanwhile, the Seebeck coefficient of Sample 3 has a pronounced negative dependency on temperature (Figure 4.5B), which corresponds to the increasing carrier concentration

and electrical conductivity with temperature. We also note that the peak Seebeck coefficient shifts from 480 K in Sample 1 to 400 – 440 K in other samples because the reduced carrier concentration due to Se doping decreases the onset temperature of bipolar effect (Figure 4.5B) [Rowe et al, 1983c]. The calculated power factor based on electrical conductivity and Seebeck coefficient is plotted out in Figure 4.5D. First, due to decreasing Seebeck coefficient with temperature, Sample 3 has the lowest power factor among all the samples. Second, in the temperature range of 300 – 500 K, the optimal Se concentration is 11.54% which gives power factor of 1.48 mW/m-K^2 at 400 K. This value is much higher than that the pure Bi_2Te_3 nanocomposite (1.04 mW/m-K^2 at 400 K and 1.16 mW/m-K^2 at 480 K). The enhancement is contributed to the optimized carrier concentration and slightly increased mobility.

4.6 Conclusion

In this chapter, we used the Bi_2Te_3 nanowire large scale synthesized in previous chapter and consolidated them into bulk pellet. In order to improve its thermoelectric performance, Se is used as a dopant to tune the carrier concentration. EDX and XRD were used to investigate the Se doping mechanism which can explain the lattice constant as well as the carrier concentration change. Due to the Se doping, the optimal power factor obtained is 1.2 mW/m-K^2 at 300 K that is around 60% higher than the undoped Bi_2Te_3 and the corresponding carrier concentration is 1.6×10^{20} cm^{-3}. The thermal conductivity measurement is still underway but should be a highlight of this research since the nanostructure is effective to reduce the thermal conductivity.

CHAPTER 5. DESIGN PRINCIPLE OF TELLURIDE-BASED NANOWIRE HETEROSTRUCTURES FOR POTENTIAL THERMOELECTRIC APPLICATIONS

The Chapter 5, 6 and 7 will discuss our work in XTe-Bi_2Te_3 (X=Pb or Ag) nanowire heterostructure synthesis and their thermoelectric properties evaluation. In this chapter, our research in the Te-Bi_2Te_3 nanowire heterostructure will be introduced and the results were published on Nano Letter in 2012. I would like to start the three consecutive chapters with an overview of the current status of solution synthesized binary-phase nanocomposite.

5.1 An Overview of the Current Status of Solution Synthesized Binary-Phase Nanocomposite

Binary-phase nanocomposites, despite of their complexity, have been enthusiastically pursued by researchers due in part to the record-breaking ZT values of 2.2 achieved in PbTe/SrTe nanostructured bulk [Biswas et al, 2012] and 2.4 obtained in Bi_2Te_3/Sb_2Te_3 superlattice film [Venkatasubramanian et al, 2001]. The significant enhancement of ZT mostly comes from the substantial thermal conductivity reduction caused by lattice mismatch between two phases and effective scattering of mid- to long-mean free path phonons by nanoinclusions in the matrix. The above successful binary-phase

nanocomposites were either fabricated with solid-state reaction or molecular beam deposition. Solution synthesis, with its time and energy efficient nature, could potentially contribute to producing such materials in a more economical yet scalable way. Here we review recent efforts in solution synthesis and conclude the challenges that need to be addressed in the future.

Table 5.1. Lattice thermal conductivity comparison between binary-phase nanocomposite and corresponding matrix fabricated with the same method. κ_L is lattice thermal conductivity and RD stands for relative density.

Nanocomposites	κ_L (W/m-K)	RD (%)	Reference
Sb_2Te_3	0.85	-	Zhang et al, 2014
Ag/oxide/Sb_2Te_3	0.65	-	
Bi_2Te_3	0.40	97	Kim et al, 2013
CNT/Bi_2Te_3	0.28	96	
PbS	1.20	80	Ibáñez et al, 2013
$(PbS)_{0.72}/(PbTe)_{0.28}$	0.69	80	
PbTe	1.90	-	Dong et al, 2013
PbTe/Graphen (3wt%)	0.81	-	
PbTe	0.94	85	Finefrock et al, 2014b
$(PbTe)_{0.96}/(Bi_2Te_3)_{0.04}$	0.55	76	Fang et al, 2013
Ag_2Te	0.3	89	Yang et al, 2014
$(Ag_2Te)_{0.95}/(Bi_2Te_3)_{0.05}$	0.24	87	Fang et al, 2014a

The common methods of making binary-phase nanocomposites through solution synthesis can be concluded in two major categories: physically blending two separately grown nanoparticles and directly solution synthesizing heterostructures. Afterwards, hybrid nanopower can be consolidated into binary-phase nanocomposites that usually possess much smaller thermal conductivity than the corresponding majority phase. Table 5.1 concludes room temperature lattice thermal conductivity (κ_L) comparison between hybrid and single phase in previous reports and a significant 20 – 60 % reduction in κ_L was observed by including a second phase, which can rival with the ~30 % reduction observed in PbTe/SrTe made by solid-state reaction [Biswas et al, 2012]. However, solution synthesized binary-phase nanocomposites can only achieve ZT around 1 that is still far to reach 2.2 of PbTe/SrTe [Biswas et al, 2012].

One important factor is that the porosity of consolidated pellets can be as high as 20 %, which significantly reduces the electrical conductivity by a factor of 10 to 1000 [Fang et al, 2013; Fang et al, 2014a; Jin et al, 2012; Scheele et al, 2011]. The significant porosity can be caused by retained surfactants [Jin et al, 2012; Scheele et al, 2011] or lack of consolidation optimization [Fang et al, 2013; Fang et al, 2014a]. To address this issue, several groups have developed surfactant-free synthesis, which can improve relative density to 85 – 93 % [Zhang et al, 2011a; Min et al, 2013]; K. T. Kim et al applied post-annealing to solution synthesized nanopowder and obtained a relative density of 97 % [Kim et al, 2013]. Another important aspect still lacking in solution synthesized binary-phase nanocomposites is the optimization of carrier concentration. To the best of our knowledge, a systematic study of optimizing carrier concentration in solution synthesized

binary-phase nanocomposites cannot be found in literature. As a matter of factor, the carrier concentrations reported by a few papers stay in the range of 10^{17} - 10^{19} cm^{-3} which is outside of the optimal range of 10^{19} – 10^{20} cm^{-3} [Kim et al, 2013; Dong et al, 2013; Scheele et al, 2011; Zhang et al, 2012a; Ko et al, 2011]. Therefore, it is quite necessary to develop ways of effectively doping solution synthesized nanocomposites for further improvement of thermoelectric properties.

In addition to the traditional ways of improving binary-phase nanocomposites discussed above, the band offset between two phases can provide a unique opportunity to further enhance power factor through low energy carrier filtering. One thing worth noting, though, is that the addition of a second phase usually can significantly alter the carrier concentration of matrix. For example, fullerene can act as p-type dopant in Bi_2Te_3 [Kim et al, 2013; Kulbachinskii et al, 2012], $PtTe_2$ can act as n-type dopant in PbTe [Zhou et al, 2009] and Ag can act as p-type dopant in Bi_2Te_3 [Zhang et al, 2012a]. Strictly speaking, only an increase of Seebeck coefficient compared to the matrix that is at the same or even lower carrier concentration could potentially be attributed to energy filtering effect. D. K. Ko et al fabricated Pt/Sb_2Te_3 nanocrystal thick film that shows a simultaneous increase of Seebeck coefficient and carrier concentration compared to Sb_2Te_3 nanocrystal thick film, which could be attributed to energy filtering effect [Ko et al, 2011]. Y. Zhang and J. H. Bahk have recently published a paper, in which a thin layer of oxide was deposited between Ag and Sb_2Te_3 to minimize Ag diffusion in matrix [Zhang et al, 2014]. The result shows Ag nanoinclusions remain intact in the Sb_2Te_3 and the Seebeck coefficient of Ag/oxide/Sb_2Te_3 was improved compared to the matrix that at a lower carrier

concentration. Pisarenko relation was also calculated at different cut-off band potentials and the experimental data points locate above the curve, which strongly suggests the existence of energy filtering effect.

After reviewing the progress of solution synthesized binary-phase nanocomposites, we think this particular field is still at its initial stage, which allows a lot of space for improvement; the future efforts should focus on optimization of surfactant removal, consolidation, carrier concentration and development of new methods to take advantage of the potential benefits from energy filtering effect.

5.2 Introduction

Certain TE materials, such as Bi_2Te_3/Sb_2Te_3 superlattice film (ZT ~ 2.4) [Venkatasubramanian et al, 2001] and $AgPb_mSbTe_{2+m}$ bulk crystals (ZT ~ 2.2) [Hsu et al, 2004], although possessing high performance due to the improved phonon scattering at nanoscale interfaces and grain boundaries, require very complicated material composition or an extremely expensive/time-consuming manufacture process such as molecular beam epitaxy. Theoretical predictions and initial experimental results have suggested that one-dimensional (1D) nanostructures, especially the nanowire heterostructures, which take the advantages of both quantum confinement to enhance the power factor and phonon scattering at nanowire surface and compositional interfaces to lower thermal conductivity, could offer a much higher ZT value [Hicks et al, 1993b; Lin et al, 2003; Dames et al, 2004; Hochbaum et al, 2008; Zhou et al, 2005]. Meanwhile, the syntheses of various 1D nanowire heterostructures have been demonstrated through the chemical vapor deposition

process based on vapor–liquid–solid (VLS) growth mechanism as well as the pulsed electrodeposition, [Wu et al, 2004; Gudiksen et al, 2002; Wang et al, 2007; Wang et al, 2008; Ouyang et al, 2006; Jin et al, 2005] but it is still a great challenge to obtain high-quality thermoelectric nanowire heterostructures in a simple yet scalable way.

We choose solution-phase chemical routes to explore the rational and scalable synthesis of 1D thermoelectric nanowire heterostructures with a particular focus on telluride-based compounds. Previously, there have been only few studies showing the growth of Te–Bi_2Te_3 heterostructures with dimensions over hundreds of nanometers using expensive precursors and surfactant [Lu et al, 2005a] or through the catalyst-assisted growth of Bi_2Te_3 plates on the tips of Te nanorods [Wang et al, 2010], but the control of size/density of Bi_2Te_3 plates has not been demonstrated. In addition, the unintentional doping of catalyst cations (Fe) could also alternate the intrinsic properties of thermoelectric materials. All of these have resulted in the unclearness of the thermoelectric performance and how such a heterogeneous system can be generally developed into other heterostructures. Herein, we show a catalyst-free synthesis of Te–Bi_2Te_3 "barbell" nanowire heterostructures with a narrow diameter and length distribution as well as a rough control over the density of the hexagonal Bi_2Te_3 plates on the Te nanowire bodies by varying the reaction conditions. The initial characterizations of the hot-pressed nanostructured bulk pellets made from the Te–Bi_2Te_3heterostructures show a largely enhanced Seebeck coefficient and greatly reduced thermal conductivity, leading to an enhanced thermoelectric figure of merit.

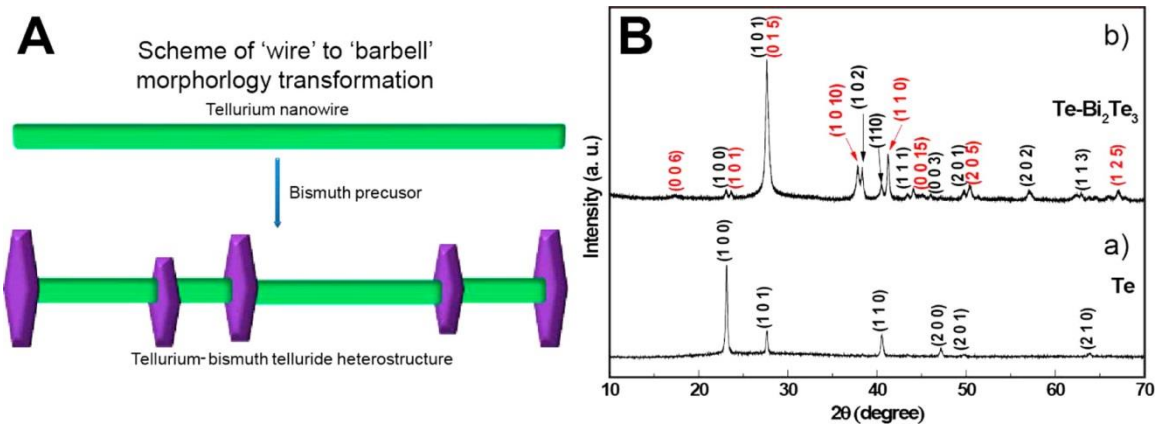

Figure 5.1. (A) Schematic of tellurium nanowire formed in the first step and tellurium−bismuth telluride heterostructure after adding bismuth precursor in the second step. (B) XRD patterns of Te nanowires and Te−Bi_2Te_3 heterogeneous nanostructures after the injection of Bi precursor solution (the black marks stand for the peaks from Te, and the red stand for Bi_2Te_3). [Adapted from reference Zhang et al, 2012b]

5.3 Synthesis Procedure

The synthesis of Te–Bi_2Te_3 "barbell" nanowire heterostructures is carried out in a standard Schlenk line with nitrogen protection. Tellurium dioxide (TeO_2, 99%+), ethylene glycol (EG, 99%+), potassium hydroxide flakes (KOH, 90%), polyvinylpyrrolidone (PVP, average molecule weight 40 000), hydrazine hydrate solution ($N_2H_4 \cdot H_2O$, 80%), bismuth nitrate pentahydrate ($Bi(NO_3)_3 \cdot 5H_2O$, 98%), and lead acetate trihydrate ($Pb(CH_3CO_2)_2 \cdot 3H_2O$, 99%+)) were all purchased from Sigma-Aldrich. All of the chemicals are used as received without further purification. In a typical synthesis, 1.5 mmol of TeO_2, 10 mmol of KOH, 0.3 g of PVP, and 15 mL of EG are added into a 50 mL three-neck flask. Nitrogen is purged through the system to keep the reaction in an oxygen-free environment. The mixture is stirred and heated to 98 °C. After all of the chemicals are dissolved thoroughly, 0.15 mL of 80% hydrazine hydrate solution is injected into the reaction, and the yellow-transparent solution starts to turn into black

slurry, which is kept under 98 °C for 1 h to let Te nanowires form completely. Meanwhile, 0.5 mmol of $Bi(NO_3)_3 \cdot 5H_2O$ is added into 5 mL of EG in a glass vial to form a solution, which is kept at 100–120 °C. After one hour, the temperature of Te nanowire solution is raised to 110 °C, and the $Bi(NO_3)_3 \cdot 5H_2O$/EG solution is hot-injected into the flask. The reaction continues at 110 °C for 1 h, and then the solution is cooled down naturally and the product is centrifuged followed by washing with deionized water three times and ethanol twice. The whole process is shown in Figure 5.1A.

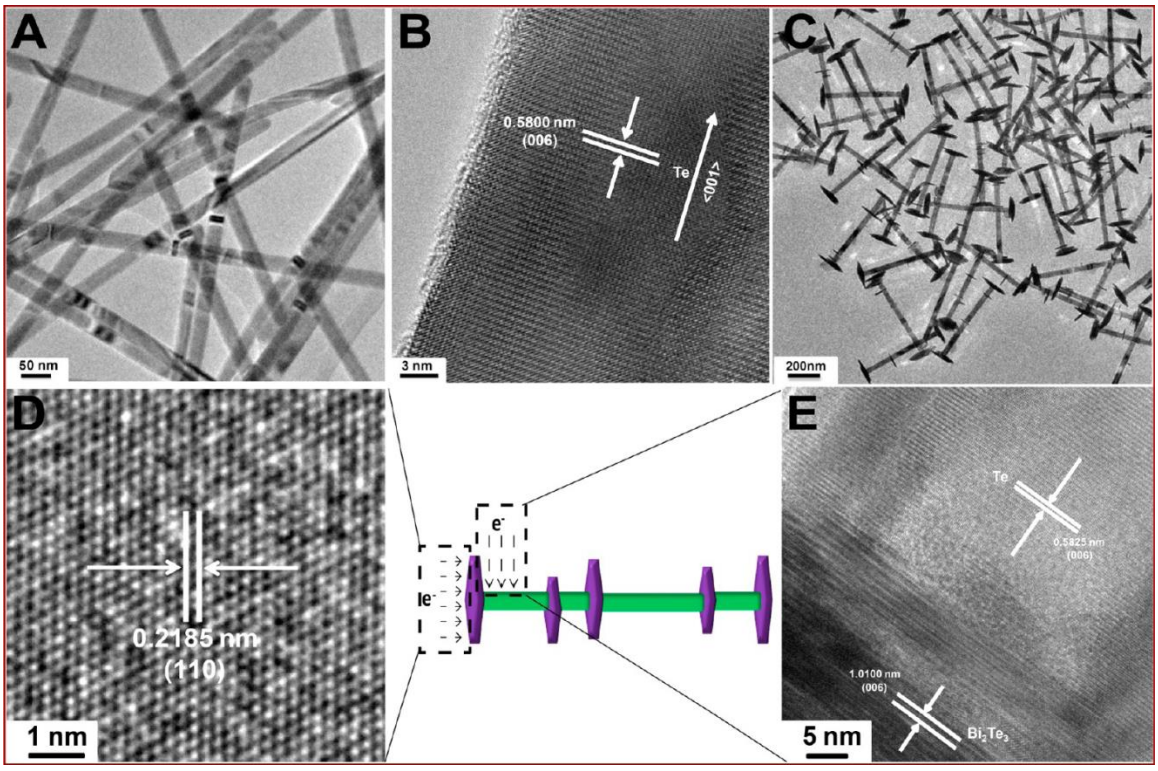

Figure 5.2. TEM images of Te nanowires and Te–Bi_2Te_3 nanowire-multiple plates heterostructure: (A) low magnification and (B) HRTEM images of tellurium nanowire; (C) low magnification and (D, E) HRTEM images of the Te–Bi_2Te_3 heterostructure. The scheme indicates the regions/view directions studied by HRTEM. Part D shows the top view of the Bi_2Te_3 plate, and part E shows the side view of Bi_2Te_3 plate and the junction between Te and Bi_2Te_3. [Adapted from reference Zhang et al, 2012b]

5.4 Results of Materials Characterization

The intermediate product of Te nanowires and the Te–Bi_2Te_3 "barbell" nanowire heterostructures are first characterized using XRD. The lower spectrum in Figure 5.1B can be readily indexed to pure hexagonal phase Te (JCPDS No. 36-1452), while the upper spectrum clearly indicates the partial formation of Bi_2Te_3 (JCPDS No. 15-0863) after adding the Bi precursor. TEM studies further confirm the conversion from the Te nanowires (Figure 5.2A and B) to the "barbell" nanowire heterostructures of Te–Bi_2Te_3 (Figure 5.2C–E) and reveal several important features: First, the TEM data demonstrate clearly the uniformity of the Te nanowires and Te–Bi_2Te_3 nanowire heterostructures. Statistical analyses performed on Figure 5.2A and C show that the diameter of Te nanowires and the Te parts in the Te–Bi_2Te_3 nanowire heterostructures are 36.62 ± 1.46 nm and 36.92 ± 1.86 nm, respectively. The nearly unchanged diameters suggest that the growth of Bi_2Te_3 is highly selective. The random deposition and alloying over the Te nanowire body in our two-step reaction is strongly suppressed, which usually will result in an obvious change in diameter as observed in our previous report [Zhang et al, 2011b]. Second, high-resolution TEM (HRTEM, Figure 5.2B, D, E) studies show the lattice-resolved images and prove that both Te nanowires and Te–Bi_2Te_3 nanowire heterostructures are single crystals. The distance between two neighboring lattice fringes in Figure 5.2B is about 0.58 nm, corresponding to the Te (006) crystal planes and suggesting the growth direction for Te nanowires is along *c*-axis, which is mainly due to the anisotropic crystal structure in hexagonal Te phase [Tang et al, 2005; Zhang et al, 2007]. Figure 5.2 parts D and E show the top view (Figure 5.2D) of the Bi_2Te_3 plate and the side view (Figure 5.2E) of Bi_2Te_3 plate; the junction between Te and Bi_2Te_3 in the

Te–Bi_2Te_3 nanowire heterostructures along the view directions highlighted in the scheme. The lattice fringes with a distance of 0.2185 nm in Figure 5.2D correspond to the (110) crystal planes of Bi_2Te_3 phase. The side view (Figure 5.2E) of Bi_2Te_3 plate shows the lattice fringe of Bi_2Te_3 (006) crystal planes and the epitaxial growth interface between Te and Bi_2Te_3, which is mainly due to the small lattice mismatch (as low as 1.62%) between the (001) crystal directions of Te and Bi_2Te_3 [Lu et al, 2005a; Habas et al, 2007].

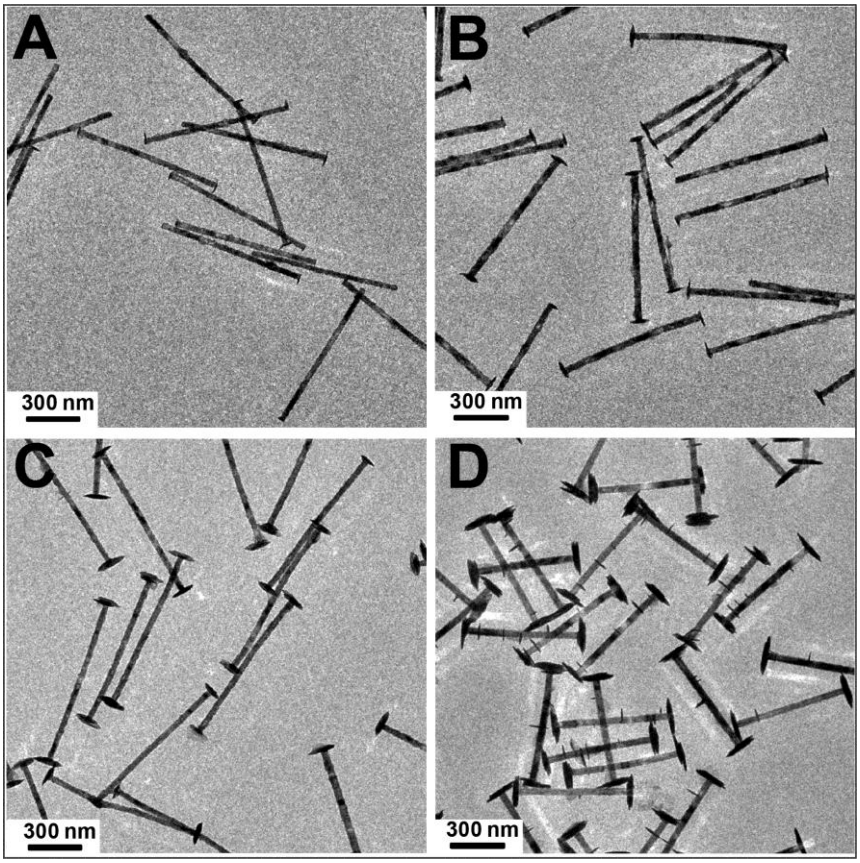

Figure 5.3. Evolution of "barbell" morphology by adding different amounts of hydrazine hydrate in the reaction: (A) 0.6 ml; (B) 0.5 ml; (C) 0.4 ml; and (D) 0.3 ml. [Adapted from reference Zhang et al, 2012b]

5.5 Discussion of Growth Mechanism

Notably, the concentration and the amount of hydrazine have been found to significantly impact the composition of the final product as well as the size and the density of the Te nanowires and Bi_2Te_3 plates. Using anhydrous hydrazine in the reaction will only lead to the formation of pure Bi_2Te_3 nanowires with a much thinner diameter, which is consistent with our previous report [Zhang et al, 2011b]. Decreasing the amount of 80% hydrazine hydrate added into the reaction (Figure 5.3) leads to the growth of a thicker Te nanowire body with larger Bi_2Te_3 plates and promotes multiple nucleation and growth of Bi_2Te_3 plates along the surface of Te nanowires (Figure 5.3D). Examining and understanding these observations suggest a possible growth mechanism for the "barbell" heterostructure: it has been widely accepted that the tips of nanowires usually possess the highest reactivity where the reaction/growth tends to happen first [Sadtler et al, 2009; Saunders et al, 2006]. If anhydrous hydrazine is used, the strong reduction environment as well as the high transient concentration of bismuth atoms (reduced from $Bi(NO_3)_3 \cdot 5H_2O$ by hydrazine) will override the preferred growth on Te nanowire tips so that a nonselective absorption and alloying between Bi and Te nanowire will lead to the uniform conversion into Bi_2Te_3 nanowires, which has been identified in the previous research [Wang et al, 2010; Zhang et al, 2011b]. Reducing the concentration of hydrazine to 80% and using smaller and smaller amounts slows down the generation of Bi atoms, thus promoting the selective growth of Bi_2Te_3 plates on the Te nanowire tips. However, when the amount/concentration of hydrazine is below a certain threshold (0.3 mL), the reaction is now controlled by the diffusion because of the slow generation of Bi atoms, and the randomly absorbed Bi atoms on Te nanowire bodies will form isolated

Bi_2Te_3 islands, which act as the new nucleation sites to guide the growth to follow the Volmer–Weber model [Xu et al, 2008]. The formation of these three-dimensional islands, along with coarsening, will cause multiple Bi_2Te_3 plates to grow on the Te nanowire surface. Statistical result from Figure 5.4E gives an average of 4.186 ± 1.314 Bi_2Te_3 plates per nanowire. Notably, analysis of the structure parameters of the "barbell" heterostructures prepared using the conditions described in Figure 5.3D, especially the positions of the Bi_2Te_3 plates (the black dots in Figure 5.4E) in the nanowire heterostructures, indicates that the positions of isolated Bi_2Te_3 plates on the nanowire body is totally random, which is significantly different from other mechanisms such as lattice strain-induced heterostructure formation [Robinson et al, 2007] and further confirms the different growth mechanisms for the Bi_2Te_3 plates on Te nanowire tips and bodies.

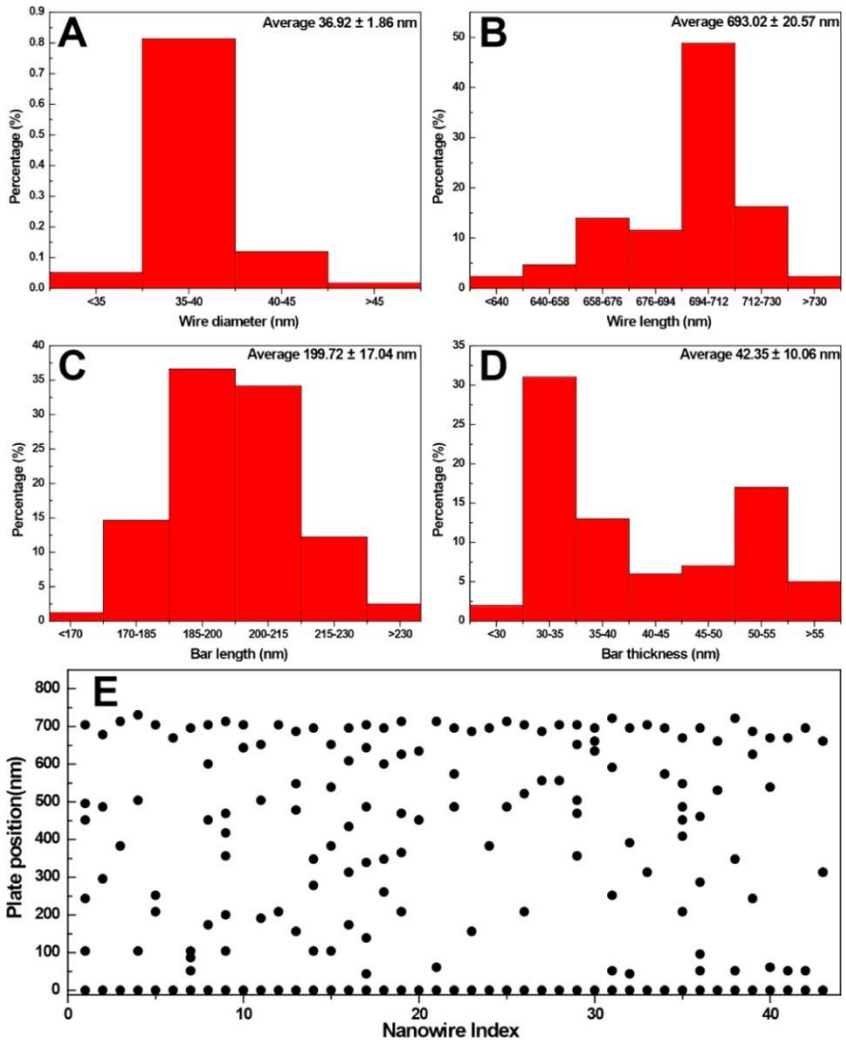

Figure 5.4. (A) and (B) Distribution of wire diameter and length; (C) and (D) distribution of bar length and thickness at the two ends of the wires; the reason for the two peaks in D is because two plates pile up at the ends of some wires; (E) the positions of the Bi_2Te_3 plates (black dots) on the nanowire heterostructures; the dots lined up perpendicularly to the *x*-axis are on a single wire. [Adapted from reference Zhang et al, 2012b]

5.6 Powder Consolidation

Figure 5.4 shows the size distributions in the diameter (Figure 5.4A, Te nanowire body) and the length (Figure 5.4B, overall length) of the Te–Bi_2Te_3 "barbell" nanowire heterostructures as well as in the length (Figure 5.4C) and the thickness (Figure 5.4D) of

the Bi_2Te_3 plates. The uniformity in all dimensions gives us a reliable and reproducible platform to study its fundamental electrical and thermal properties. In a typical process, we first remove the capping ligands on nanowire heterostructures by combining the Te–Bi_2Te_3 "barbell" nanowire heterostructures dispersed in ethanol with diluted hydrazine solution (10% volume ratio) and stirring vigorously until all of the nanowires are precipitated. The supernatant is decanted, and the precipitate is washed with ethanol three times to remove hydrazine residual. After the hydrazine treatment, the nanowires are collected by centrifugation, dried in vacuum, and consolidated into bulk pellets with 1.25 cm in diameter and 0.25 cm in thickness by hot press at 423 K for 30 min under an axial pressure of 150 MPa. For thermoelectric property measurements between 300 and 400 K, the pellets are cut into regular rectangular shapes and mechanically polished before the measurement of electrical conductivity, Seebeck coefficient, and thermal conductivity. The electrical conductivity is measured through a standard four-probe method with a maximum temperature fluctuation of ±2 K. The Seebeck coefficient is measured by bridging the sample between a heater and heat sink and testing the voltage difference between the hot and the cold sides with a maximum temperature fluctuation of ±0.2 K and a voltage resolution of 50 nV. The thermal conductivity (κ) is measured through thermal diffusivity (α) and specific heat (C_p) and then calculated via the equation $\kappa = \alpha\rho C_p$ (ρ is the density).

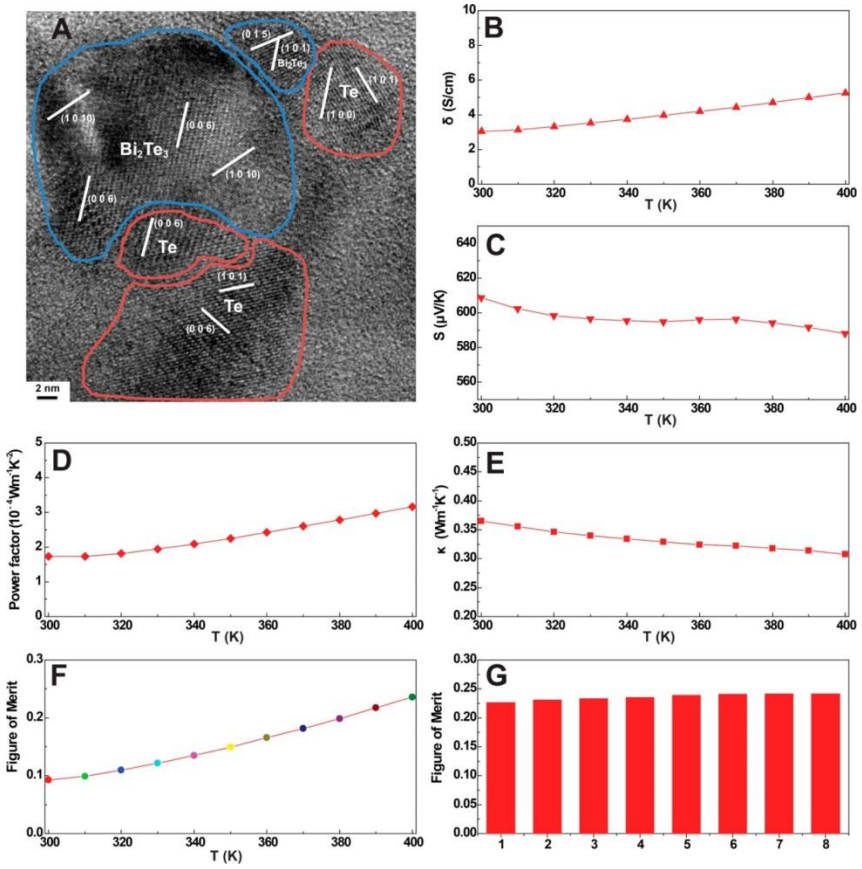

Figure 5.5. Thermoelectric properties of bulk nanocomposite pellet made by hot pressing the as-obtained Te–Bi_2Te_3 nanowire heterostructures. (A) Cross section HRTEM image of hot-pressed sample which clearly shows nanoscale grain boundaries preserved inside the sample; (B) electric conductivity, (C) Seebeck coefficient, (D) power factor, (E) thermal conductivity, (F) ZT of a typical sample measured between 300 and 400 K, and (G) the distribution of peak ZT from different samples. [Adapted from reference Zhang et al, 2012b]

5.7 Results of Thermoelectric Properties Measurement

Figure 5.5 shows the thermoelectric properties of the nanowire heterostructure composites after the hot press. Figure 5.5A shows the cross section HRTEM image of the nanowire heterostructure composite in which the nanoscale grain boundaries have been well-preserved to enhance the phonon scattering. The random orientations of the Te and Bi_2Te_3 domains also suggest the nanocomposite is a highly isotropic system. The

electrical conductivity (Figure 5.5B) of the Te–Bi_2Te_3 nanowire heterostructures increases from 3.051 $S \cdot cm^{-1}$ at 300 K to 5.244 $S \cdot cm^{-1}$ at 400 K. Figure 5.5C shows the temperature dependence of Seebeck coefficient of the Te–Bi_2Te_3 nanowire heterostructures. The positive Seebeck coefficient value indicates the p-type conduction. The Seebeck coefficient measurement shows a decreasing trend from 608 $\mu V \cdot K^{-1}$ at 300 K to 588 $\mu V \cdot K^{-1}$ at 400 K. The thermal conductivity (Figure 5.5E) is measured to be 0.365 $W \cdot m^{-1} \cdot K^{-1}$ at 300 K and decreases to 0.309 $W \cdot m^{-1} \cdot K^{-1}$ at 400 K. The calculated ZT for the Te–Bi_2Te_3 nanowire heterostructures (Figure 5.5F) increases from 0.09 at 300 K to around 0.24 at 400 K.

An analysis of these results highlights some important points: First, the electrical conductivity of our Te–Bi_2Te_3 nanowire heterostructures (3.051 S/cm at 300 K) is much higher than the value of the Te nanowires (0.08 S/m at 298 K) [See et al, 2010] and is comparable with the value of bulk Te (3.04 S/cm at 293 K). This improvement is mainly due to the hot press to form a nanostructured bulk disk with a reasonably high relative density (~63%) as well as the introduction of more electrically conductive Bi_2Te_3 to form the heterostructures, which through our rough estimation, counts for about 63.6% in the total volume. Further improvement in electrical conductivity could be achieved by optimizing the hot press temperature and pressure, and related systematic studies are underway. Second, the Seebeck coefficient in our Te–Bi_2Te_3 nanowire heterostructures (608 $\mu V \cdot K^{-1}$ at 300 K and 588 $\mu V \cdot K^{-1}$ at 400 K) is also considerably higher than that of Te nanowires (408 $\mu V \cdot K^{-1}$ at 298 K) [See et al, 2010], Te bulk crystals (340 $\mu V \cdot K^{-1}$ at 293 K). The largely enhanced Seebeck coefficient could result from the energy filtering

effect occurring at grain–grain interfaces, as seen in Figure 5.5A in our hot pressed samples. To decide whether there is any energy filtering effect happening in the heterostructure, the work function and band gap of tellurium and bismuth telluride need to be experimentally determined. However, if we use the work function and band gap reported in previous literatures (4.95 eV and 0.3 eV for tellurium [Zhang et al, 2012a] and 5.30 eV and 0.15 eV for bismuth telluride [Haneman, 1959], respectively), the Fermi level offset between the two materials is 0.35 eV, which is similar to the ones in previous papers where energy filtering was observed [Zhang et al, 2012a; Ko et al, 2011]. Based on the facts above, it is possible that low-energy carriers (holes in this case) are scattered by the energy barrier and high-energy carriers pass through with the proper band alignment in our heterostructure, thus leading to an increased power factor by theoretical prediction [Shakouri, 2011; Vashaee et al, 2004]. Third, the thermal conductivity of our sample (0.365 $W \cdot m^{-1} \cdot K^{-1}$ at 300 K and 0.309 $W \cdot m^{-1} \cdot K^{-1}$ at 400 K) is only ~16% of bulk Te crystal (2.27 $W \cdot m^{-1} \cdot K^{-1}$ at 293 K) and ~26% of pure Bi_2Te_3 nanowires reported previously (1.42 $W \cdot m^{-1} \cdot K^{-1}$ at 300 K and 1.19 $W \cdot m^{-1} \cdot K^{-1}$ at 400 K) [Zhang et al, 2011b]. Such a low thermal conductivity is comparable to the Te nanowire–poly(3,4-ethylenedioxythiophene):poly(styrenesulfonate) (PEDOT:PSS) composite (0.22–0.30 $W \cdot m^{-1} \cdot K^{-1}$ at 298 K) and pure organic PEDOT:PSS polymer (0.24–0.29 $W \cdot m^{-1} \cdot K^{-1}$ at 298 K) [See et al, 2010], which directly benefits from the enhanced phonon scattering at nanowire–nanowire, nanowire–plate, and plate–plate interfaces. Lastly and most importantly, the *ZT* of our Te–Bi_2Te_3 nanowire heterostructure-based composite is more than two orders better than pure Te nanowires (0.0004 at 298 K) and 2.4 times better than the Te nanowire–PEDOT:PSS composite (0.1

at 298 K). Moreover, our *ZT* has a very narrow distribution (0.2360 ± 0.0057) as shown in Figure 5.5G, which further proves the reliability and reproducibility of our synthetic approach. Notably, the *ZT* value observed here is much lower compared to the pure Bi_2Te_3nanowires (0.96 at 380 K) [Zhang et al, 2011b], which is mainly due to the presence of large percentage of Te (~36.4%) in the heterostructures, which significantly lowers the electrical conductivity of the heterostructures.

5.8 Conclusion

In summary, we have successfully developed a rational solution phase synthetic approach that will instantly open up great wealth of opportunities for the fundamental studies about the electron and phonon interactions in the unique platforms of telluride-based nanowire heterostructures. Initial physical characterizations demonstrate a significantly improved thermoelectric performance due to the enhanced phonon scattering at nanowire heterostructure surface and interface, which could significantly inspire further advances in using novel nanowire heterostructures for thermoelectric energy conversion.

CHAPTER 6. SYNTHESIS AND THERMOELECTRIC PROPERTIES OF COMPOSITIONAL-MODULATED LEAD TELLURIDE–BISMUTH TELLURIDE NANOWIRE HETEROSTRUCTURES

We demonstrate the rational solution-phase synthesis of compositional modulated telluride nanowire heterostructures containing lead telluride (PbTe) and bismuth telluride (Bi_2Te_3). By tuning the ratio between PbTe and Bi_2Te_3 through adjusting the amount of critical reactants and precursors during the synthesis, the influence of composition on the thermoelectric properties of the nanowire heterostructures has been investigated in hot pressed nanocomposite pellets. Measurements of the thermoelectric properties show strongly reduced thermal conductivity that leads to an enhanced thermoelectric figure of merit (*ZT*) of 1.2 at 620 K. The results of this research have been published on Nano Letter in 2013 [Fang et al, 2013].

6.1 Introduction

In the most recent literatures, dual-phase nanocomposites were studied intensively because of the extremely low thermal conductivity and great potential for enhancing thermoelectric properties [Biswas et al, 2012; Lo et al, 2012; Girard et al, 2012]. Herein, we use the Te–Bi_2Te_3 barbell nanowire heterostructures developed by our group previously [Zhang et al, 2012b] to synthesize PbTe/Bi_2Te_3 "barbell" nanowire heterostructures by converting the Te section into PbTe. The influence of composition

(ratio between PbTe and Bi_2Te_3) has been investigated in hot pressed nanocomposite pellets.

Few investigations have been performed on the PbTe/Bi_2Te_3 system. In the existing papers discussing PbTe/Bi_2Te_3 related systems, other elements, such as Sn and Sb, were introduced to form ternary alloy compounds; in other cases, Pb^{2+} or Bi^{3+}were simply used as dopants in Bi_2Te_3 or PbTe, respectively, without the coexistence of both phases [Oh et al, 2009; Su et al, 2006; Zhu et al, 2005]. Meanwhile, most of these materials were synthesized by high-temperature solid-state reaction, which are energy intensive. Moreover, ball milling has been used to obtain nano/micrometer-size grains, but it offers little control on the dimensions and uniformity of the grain sizes of each component.

6.2 Synthesis Procedure

Our synthetic approach to produce PbTe/Bi_2Te_3 nanowire heterostructures involves a three-step solution-phase reaction at a much lower temperature compared to solid-state reactions. The reaction starts with the synthesis of Te nanowires, followed by the growth of Bi_2Te_3nanoplates on the Te nanowire bodies, and then ends with the conversion of Te sections in the Te–Bi_2Te_3 nanowire heterostructures into PbTe. The synthesis of PbTe–Bi_2Te_3 barbell nanowire heterostructures is carried out in a standard Schlenk line with nitrogen protection. Tellurium dioxide (TeO_2, 99%+), ethylene glycol (EG, 99%+), potassium hydroxide flakes (KOH, 90%), polyvinylpyrrolidone (PVP, average molecule weight 40 000), hydrazine hydrate solution ($N_2H_4 \cdot H_2O$, 80%), anhydrous hydrazine (98%), bismuth nitrate pentahydrate ($Bi(NO_3)_3 \cdot 5H_2O$, 98%), and lead acetate trihydrate

($Pb(CH_3CO_2)_2 \cdot 3H_2O$, 99%+) were all purchased from Sigma-Aldrich. All of the chemicals are used as received without further purification. In a typical process, 1.5 mmol of TeO_2, 10 mmol of KOH, 0.3 g of PVP, and 15 mL of EG are added into a 50 mL three-neck flask. Nitrogen is purged through the system to keep the reaction in an oxygen-free environment. The mixture is stirred and heated to 98 °C. After all of the chemicals are dissolved thoroughly, 0.20 mL of 80% hydrazine hydrate solution is injected into the reaction, and the yellow-transparent solution becomes a black slurry, which is kept at 98 °C for 1 h to allow Te nanowires to form completely. Meanwhile, 0.6 mmol (for $PbTe/Bi_2Te_3$ = 2:1, molar ratio) or 0.1 mmol (for $PbTe/Bi_2Te_3$ = 27:1, molar ratio) of $Bi(NO_3)_3 \cdot 5H_2O$ are added into 5 mL of EG in a glass vial to form a solution that is kept at around 100 °C. After that, the temperature of Te nanowire solution is raised to 110 °C, and the $Bi(NO_3)_3 \cdot 5H_2O$/EG solution is hot-injected into the flask. The reaction continues at 110 °C for another hour. At the same time, 0.6 mmol (for $PbTe/Bi_2Te_3$ = 2:1) or 1.35 mmol (for $PbTe/Bi_2Te_3$ = 27:1) of $Pb(CH_3CO_2)_2 \cdot 3H_2O$ are added into 5 mL of EG in a glass vial to form a solution which is kept at around 100°C. After 1 h, 0.4 mL of anhydrous hydrazine is first added into the reaction and then the $Pb(CH_3CO_2)_2 \cdot 3H_2O$/EG solution is injected into the reaction, which continues for another 1 h before naturally cooling down to room temperature. The as-obtained product is centrifuged followed by washing with deionized water three times and ethanol twice. The whole procedure is shown in Figure 6.1A.

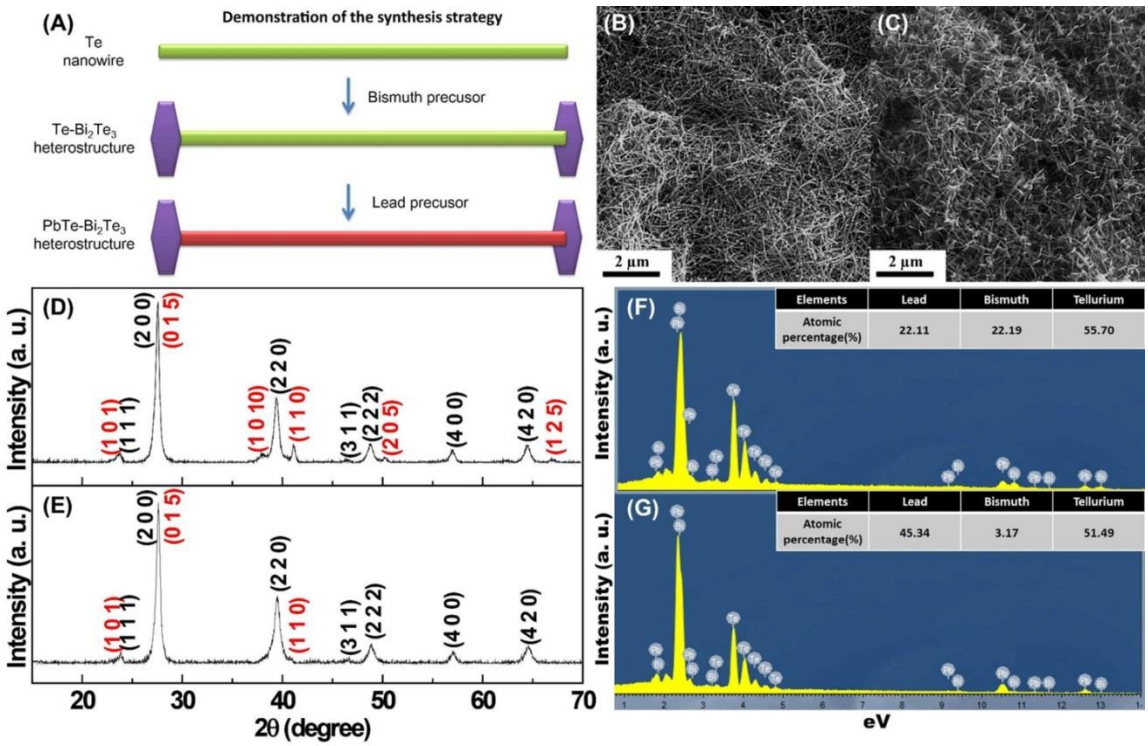

Figure 6.1. (A) Scheme of the transformation in the three-step synthesis of PbTe–Bi_2Te_3 barbell nanowire heterostructures. SEM images of the nanowire heterostructures with composition ratio of (B) PbTe/Bi_2Te_3 = 27:1 and (C) PbTe/Bi_2Te_3 = 2:1. XRD patterns of (D) PbTe/Bi_2Te_3 = 2:1 sample and (E) PbTe/Bi_2Te_3 = 27:1 sample. The black text refers to PbTe and the red text refers to Bi_2Te_3. Energy dispersive X-ray spectroscopy (EDS) of (F) PbTe/Bi_2Te_3 = 2:1 sample and (G) PbTe/Bi_2Te_3 = 27:1 sample. Inlaid tables give the atomic percentage of Pb, Bi, and Te. [Adapted from reference Fang et al, 2013]

6.3 Resultes of Materials Charaterization

The products of the PbTe/Bi_2Te_3 barbell nanowire heterostructures with different compositions are first characterized by scanning electron microscopy (SEM) (Figure 6.1B, C), XRD (Figure 6.1D,E), and energy dispersive X-ray spectroscopy (EDS) (Figure 6.1F,G). Interestingly, both products show nanowire shape observed from SEM studies and both XRD spectra can be readily indexed into PbTe (JCPDS No. 38-1435) and Bi_2Te_3 (JCPDS No. 15-0863) without Te impurity peaks, proving a complete

conversion of Te into PbTe. However, the intensity of the Bi_2Te_3 peaks in the XRD patterns is slightly different. Bi_2Te_3 peaks in the PbTe/Bi_2Te_3 = 27:1 sample spectrum (Figure 6.1E) are almost unidentifiable because of the low Bi_2Te_3 concentration. Meanwhile, the (1 1 0) peak of Bi_2Te_3 grows much higher and those peaks not appearing in the PbTe/Bi_2Te_3 = 27:1 sample spectrum, such as (2 0 5) and (1 2 5), start to arise in the PbTe/Bi_2Te_3 = 2:1 sample spectrum (Figure 6.1D), which clearly indicates an increased amount of Bi_2Te_3 phase. Furthermore, the composition difference between the two samples is further confirmed by EDS (Figure 6.1F,G), which shows that the elements in both samples have stoichiometric ratios with nearly negligible Te redundancy (0.14% for the PbTe/Bi_2Te_3 = 2:1 sample and 0.69% for the PbTe/Bi_2Te_3 = 27:1 sample). The Bi_2Te_3 molar percentage of 33.4% in the PbTe/Bi_2Te_3 = 2:1 sample (theoretical value: 33.3%) and of 3.38% in the PbTe/Bi_2Te_3 = 27:1 sample (theoretical value: 3.57%) were obtained, which proves that our strategy to control over the molar ratio between PbTe and Bi_2Te_3 during the synthesis by adjusting the amount of the initial precursors is quite successful. Notably, these two compositions represent the boundary of a wide tunable range where we can vary the ratio between PbTe and Bi_2Te_3 while still maintaining the nanowire heterostructures; if the PbTe/Bi_2Te_3 ratio is smaller than 2:1, the extra Bi precursor would lead to the random deposition of Bi_2Te_3 on the nanowire body and suppress the selective growth of Bi_2Te_3 plates on the ends of the initial Te nanowires; if the PbTe/Bi_2Te_3 ratio is larger than 27:1, the low concentration of Bi precursor amount would not be enough to form two obvious plates on the two ends of Te nanowire.

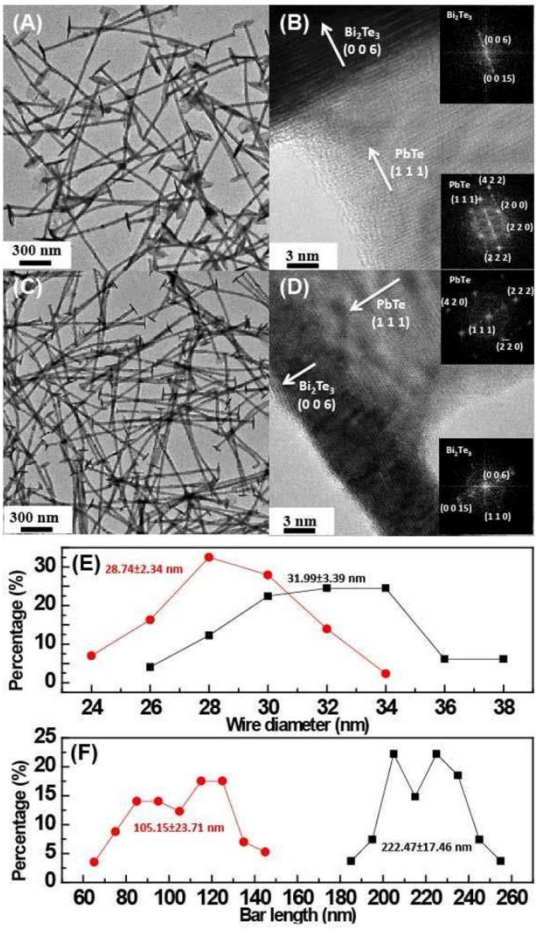

Figure 6.2. (A) and (C) Low-magnification TEM images of the PbTe/Bi_2Te_3 barbell nanowire heterostructures with compositions of PbTe/Bi_2Te_3 = 2:1 and PbTe/Bi_2Te_3 = 27:1. (B) and (D) HRTEM images of the interface between Bi_2Te_3 bar and PbTe nanowire body in the samples with the composition of PbTe/Bi_2Te_3 = 2:1 and PbTe/Bi_2Te_3 = 27:1. (E) and (F) The histogram of the diameter of PbTe nanowire body and the length of Bi_2Te_3bars, respectively. The red curves refer to the sample of PbTe/Bi_2Te_3 = 27:1 and the black curves refer to the sample of PbTe/Bi_2Te_3 = 2:1. [Adapted from reference Fang et al, 2013]

The PbTe/Bi_2Te_3 barbell nanowire heterostructures are further studied by TEM. The low-magnification TEM images of the PbTe/Bi_2Te_3 = 2:1 sample (Figure 6.2A) and the PbTe/Bi_2Te_3 = 27:1 sample (Figure 6.2C) clearly display the uniformity of the barbell morphology with smooth surfaces. The statistical analysis on Figure 6.2A, C shows the

similar average diameters of the PbTe nanowire part (Figure 6.2E) of 28.74 ± 2.34 nm (for the PbTe/Bi_2Te_3 = 2:1 sample) and 31.99 ± 3.39 nm (for the PbTe/Bi_2Te_3 = 27:1). The average lengths of the Bi_2Te_3 bars (Figure 6.2F), however, are quite different in the two samples with of 222.47 ± 17.46 nm in the PbTe/Bi_2Te_3 = 2:1 sample and 105.15 ± 23.71 nm in the PbTe/Bi_2Te_3= 27:1 sample. Such a big difference (~120 nm) is consistent with the disparity of Bi molar concentration in the two samples. Moreover, the HRTEM images taken at the interface of the PbTe nanowires and Bi_2Te_3 bars (Figure 6.2 C, D) reveal several important points: first, the nearly defects-free lattices infer the single crystalline nature of both the nanowire and bar parts; second, the fast Fourier transform (FFT) performed individually on the nanowire and bar parts show the pure PbTe and Bi_2Te_3 phases, respectively; third, the axial direction of PbTe and Bi_2Te_3 is perpendicular to the (1 1 1) and (0 0 6) crystal planes, respectively. There is a 4.01% lattice mismatch at the PbTe/Bi_2Te_3 interface, which is larger than the Te/Bi_2Te_3 interface lattice mismatch (1.62%) but still small enough to tolerate epitaxial growth.

6.4 Powder Consolidation

The rational and reproducible PbTe-Bi_2Te_3 barbell nanowire heterostructures synthesis procedure confirmed by various characterization methods provides us the opportunity to further investigate their bulk thermoelectric properties through mass production. The as-synthesized products are washed with hydrazine to remove the capping ligands on the surfaces of barbell nanowire heterostructures and vacuum-dried at room temperature following the detailed procedures described in our previous paper [Zhang et al, 2012b]. Afterward, the cleaned and dried nanowire powder is hot-pressed at 150 °C and

165 MPa for half an hour and then naturally cooled down to room temperature while the pressure is maintained at 165 MPa. A subsequent annealing at 300 °C for two hours is followed to eliminate unwanted defects created during the hot press and remove retained capping ligands.

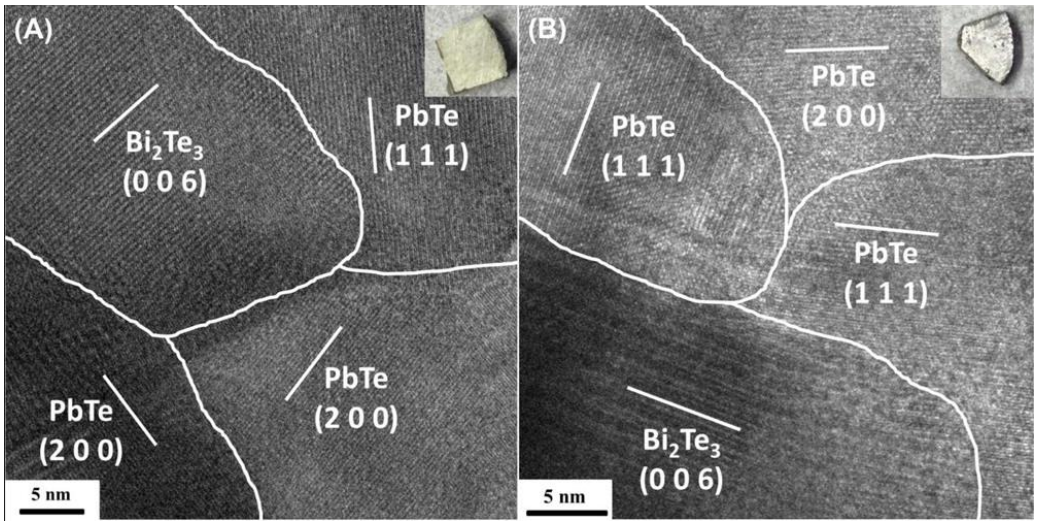

Figure 6.3. (A) and (B) Cross section HRTEM images of the sample PbTe/Bi_2Te_3 = 2:1 and the sample PbTe/Bi_2Te_3 = 27:1 pellets, which clearly show nanoscale PbTe and Bi_2Te_3 crystal domains and preserved grain boundaries inside the nanocomposites. The insets are digital photos of two PbTe-Bi_2Te_3 pellets after hot pressing and subsequent annealing. [Adapted from reference Fang et al, 2013]

Digital photos (insets, Figure 6.3A, B) of the two samples show a slight color variation because of the different compositions. The temperatures for hot pressing and annealing are much lower compared to the alloying temperature shown in the equilibrium diagram of the PbTe and Bi_2Te_3 binary system and the possible ternary compounds ($PbBi_xTe_y$), such as $PbBi_2Te_4$, $PbBi_4Te_7$, or $Pb_3Bi_4Te_9$ can only form at 850 K [Hirai et al, 1967]. The preservation of the compositions (PbTe and Bi_2Te_3 instead of their alloys) and nanoscale

grain boundaries are clearly demonstrated by the HRTEM studies performed on the cross sections of the hot-pressed/annealed samples of $PbTe/Bi_2Te_3$ = 2:1 (Figure 6.3A) and $PbTe/Bi_2Te_3$ = 27:1 (Figure 6.3B) in both of which the different nanoscale grains can be readily identified as PbTe and Bi_2Te_3 phases with random orientations.

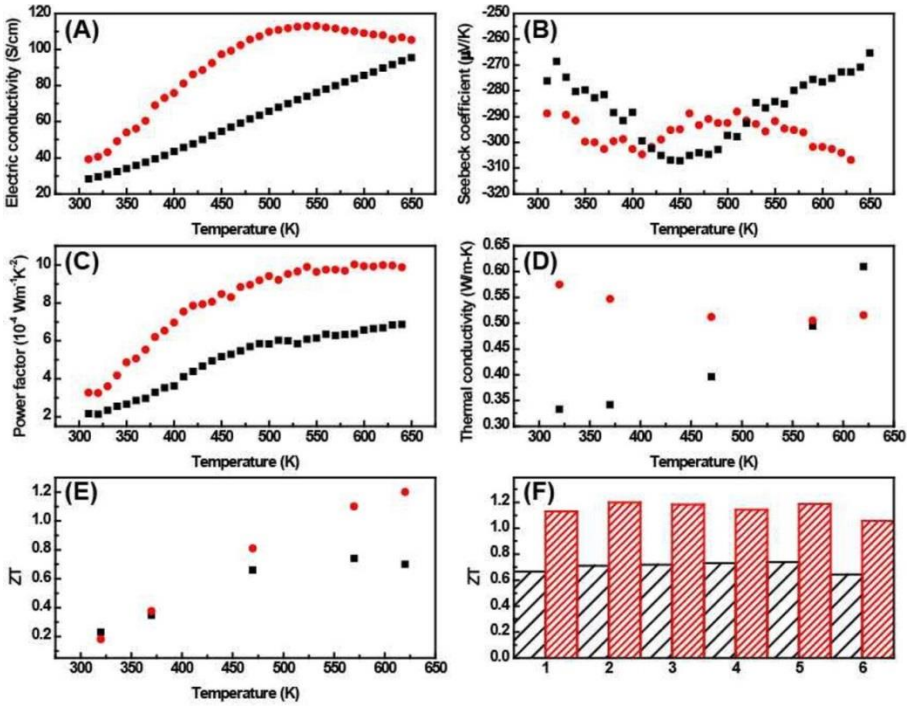

Figure 6.4. Thermoelectric properties of the $PbTe/Bi_2Te_3$ = 2:1 sample and the $PbTe/Bi_2Te_3$ = 27:1 sample made by hot pressing and subsequently annealing the heterostructures. The red dot curves and the red bars stand for the $PbTe/Bi_2Te_3$ = 27:1 sample and the black square curves and the black bars stand for the $PbTe/Bi_2Te_3$ = 2:1 sample. (A) Electrical conductivity, (B) Seebeck coefficient, (C) power factor, (D) thermal conductivity, (E) ZT of a typical sample measured between 300 and 650 K, and (F) the distribution of peak ZT values based on the different Seebeck coefficients measured on six samples from each composition. [Adapted from reference Fang et al, 2013]

6.5 Results of Thermoelectric Properties Measurement

In the temperature range from 310 to 650 K, the electric conductivity of the $PbTe/Bi_2Te_3$ = 2:1 sample increases from 28 to 90 S/cm, while the $PbTe/Bi_2Te_3$ = 27:1

sample has a higher electric conductivity that increases from 39 to 113 S/cm at 550 K and then decreases to 105 S/cm (Figure 6.4A). The different conductivities could be explained in two aspects: first, a larger Bi_2Te_3 composition could lead to more PbTe/Bi_2Te_3 interfaces, which could scatter the electron transport; second, even though the same process was applied to fabricate the two pellets, the relative density of PbTe/Bi_2Te_3 = 27:1 pellet (76.27%) is higher than that of PbTe/Bi_2Te_3 = 2:1 pellet (68.22%). In fact, because of the noticeable porosity in both pellets, the electric conductivities of both samples are much smaller compared to those of bulk Bi_2Te_3 (880 S/cm) [Poudel et al, 2008] and PbTe [LaLonde et al, 2011b]. However, our samples' electric conductivities are still comparable to other PbTe-based nanocomposites at high-temperature range where the optimum ZT occurs, such as PbTe/BaTe (150 S/cm at 750K) [Lo et al, 2012] and PbTe/$PbSnS_2$ (140 S/cm at 500K) [Girard et al, 2012]. Both samples with different composition show n-type behavior as shown by the negative Seebeck coefficients observed with absolute value between 250 μV/K and 310 μV/K (Figure 5.4B), which are slightly improved compared to the bulk Bi_2Te_3 (optimum Seebeck coefficient, 220 μV/K) [Poudel et al, 2008] and the bulk PbTe (optimum Seebeck coefficient, 230 μV/K) [LaLonde et al, 2011b]. The enhanced Seebeck coefficient could partially result from the energy filtering effect at the PbTe/Bi_2Te_3 interface with a band offset around 0.16 eV [Haneman et al, 1959; Green et al, 1968]. The temperature-dependent behavior of the Seebeck coefficient is related with the bipolar effect in which the thermal excited holes have opposite contribution to Seebeck coefficient thereby reducing the absolute value [Snyder et al, 2008]. Such a bipolar effect becomes more obvious with increasing temperature: in both the

$PbTe/Bi_2Te_3$ = 27:1 and the $PbTe/Bi_2Te_3$ = 2:1 samples, the Seebeck coefficients reach to the maximum absolute values between 400 and 450 K and then start to decrease. The only difference between two samples is that in the $PbTe/Bi_2Te_3$ = 27:1 the Seebeck coefficient starts to increase again after 520 K due to the saturation of the electric conductivity while in the $PbTe/Bi_2Te_3$ = 2:1 sample the electrical conductivity keeps increasing (due to enhanced hole transport), thus further decreasing the Seebeck coefficient. The most interesting property of the two samples is the extremely low thermal conductivity (Figure 6.4 D). At temperatures between 310 and 620 K, the thermal conductivity of the $PbTe/Bi_2Te_3$ = 2:1 sample ranges from 0.333 to 0.610 W/m·K which is lower than that of the $PbTe/Bi_2Te_3$ = 27:1 sample (0.575–0.515 W/m·K). The thermal conductivity results highlight a few important points. First, the overall thermal conductivities of both samples are significantly smaller than the lowest thermal conductivity of bulk Bi_2Te_3 (1.4 W/m·K at 345 K) [Poudel et al, 2008] and PbTe (1.4 W/m·K at 720 K) [LaLonde et al, 2011b], as well as other telluride based nanocomposites, such as PbTe/BaTe (0.9 W/m·K at 750 K) [Lo et al, 2012] and $PbTe/PbSnS_2$ (0.9 W/m·K at 500 K) [Girard et al, 2012]; second, the calculated lattice thermal conductivities (Lorenz number = 2.44×10^{-8} $W \cdot S^{1-} \cdot K^{-2}$) of our nanocomposites are from 0.307 to 0.427 W/m·K for the $PbTe/Bi_2Te_3$ = 2:1 sample and from 0.350 to 0.550 W/m·K for the $PbTe/Bi_2Te_3$= 27:1 sample, respectively. The lattice thermal conductivities of both samples are much smaller than bulk Bi_2Te_3 (0.8 W/m·K at 345 K) [Poudel et al, 2008] and PbTe (0.8 W/m·K at 720 K) [LaLonde et al, 2011b], as well as PbTe/BaTe (0.63 W/m·K at 750 K) [Lo et al, 2012] and PbTe–$PbSnS_2$ (0.73 W/m·K at 500 K) [Girard et al, 2012] nanocomposites. On the basis of the measured electrical

conductivities, Seebeck coefficients, and thermal conductivities, we calculate the ZT of the two nanocomposite samples and plot the temperature-dependent curves in Figure 6.4E. The peak ZT of the PbTe/Bi_2Te_3 = 2:1 sample is 0.72 at 570 K, which is smaller than the one of the PbTe/Bi_2Te_3 = 27:1 sample (1.20 at 620 K). Notably, the peak ZT value (1.20 at 620 K) of PbTe/Bi_2Te_3 = 27:1 sample is better than that of the bulk Bi_2Te_3 (1.05 at 320 K) [Poudel et al, 2008] and slightly higher than the ZT (1.19) of the state-of-the-art bulk n-type bulk PbTe at the same temperature of 620 K [LaLonde et al, 2011b].

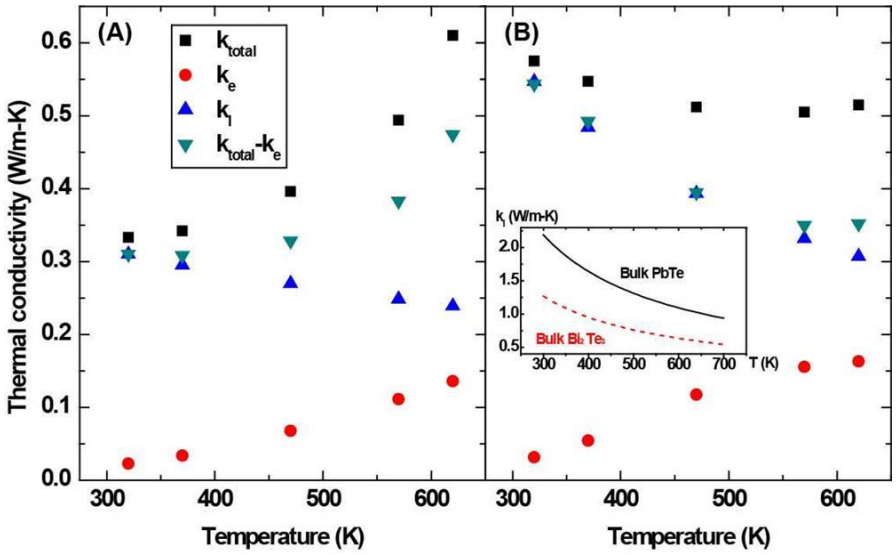

Figure 6.5. Thermal conductivity of the 2:1 (A) and 27:1 (B) PbTe/Bi_2Te_3nanocomposites, including the total thermal conductivity (black squares), electron contribution (red circles), and lattice contribution (upward-pointing triangles). The down-triangular denotes the remaining part after subtracting the electron contribution from the total thermal conductivity. The inset in (B) shows the lattice thermal conductivity of bulk PbTe [Qiu et al, 2012] and bulk Bi_2Te_3 [Satterthwaite et al, 1957; Huang et al, 2008]. [Adapted from reference Fang et al, 2013]

6.6 Analysis on Thermal Conductivity

The enhanced ZT values in our nanowire heterostrutures mainly result from the low thermal conductivities observed in both nanocomposites, however, the measured thermal conductivities of the two nanowire heterostructures with different compositions show completely different temperature dependence, for which we have applied a theoretical analysis of our materials. It has been already known that the total thermal conductivity is contributed by lattice k_l, electronk_e, and bipolar effect $k_{e\text{-}h}$

$$k_{total} = k_l + k_e + k_{e-h} \quad \text{.....(6.1)}$$

The electron part k_e can be estimated by Wiedemann–Franz law $k_e = \sigma(T)L_0T$, $L_0 = 2.44 \times 10^{-8}\text{W}\cdot\text{S}^{-1}\cdot\text{K}^{-2}$, which is approximately applicable for quasicrystals and approximants [Mahan et al, 1999; Maciá et al, 2002] and has been used in many other works [Mahan et al, 1999; Maciá et al, 2002; Toprak et al, 2004]. To understand the remaining part $k_{total} - k_e$, we use the effective medium approximation (EMA) and empirical fitting to find the lattice contribution and finally obtain the bipolar effect contribution. First, existence of the porosity [Bauer, 1993; Raghavan et al, 1998; Yadav et al, 2011] can decease the lattice thermal conductivity according to $k_l = (1 - P)^{3/2}k_f$, where k_f is the lattice thermal conductivity of the imagined fully dense nanocomposites, $P = 1 - \rho/\rho_f$ is the porosity, whose values are 0.316 and 0.2364 for the 2:1 and 27:1 $PbTe/Bi_2Te_3$ nanocomposites, respectively. Second, k_f can be described [Toprak et al, 2004; Evans et al, 2008; Jay, 2006; Yang et al, 2002] as $1/k_f = 1/k_0 + 2R_k/d$, where k_0 is the lattice thermal conductivity of the imagined nonboundary-resistance nanocomposite, R_k is the thermal boundary and interfacial resistance (Kapitza resistance), and d is the average grain diameter. The temperature dependence of Kapitza resistance can be expressed as $R_k \sim T^{\beta}$ where the

value of β can be either positive [Toprak et al, 2004] or negative [Jay, 2006]. Additionally, k_0 can be evaluated from EMA originally done by Bruggemann [Bruggemann, 1935] and developed by Nan et al [Hamilton et al, 1962; Jiajun et al, 2004; Nan et al, 1997].

$$k_0 = k_1 \frac{k_2 + (n-1)k_1 - (n-1)p_1(k_1 - k_2)}{k_2 + (n-1)k_1 + p_2(k_1 - k_2)} \quad \text{.....(6.2)}$$

Where $n = 3/\Psi$ is the shape factor of nanoparticles with sphericity $\Psi \leq 1$, p_2 is the volume fraction of Bi_2Te_3, and k_1 and k_2 are the lattice thermal conductivity [Goldsmid, 1956] of bulk PbTe and bulk Bi_2Te_3, respectively. Finally the lattice thermal conductivity can be expressed by

$$k_l = (1-P)^{3/2}\left(\frac{1}{k_0} + \frac{2R_k}{d}\right)^{-1} \quad \text{.....(6.3)}$$

Considering that the bipolar contribution increases [Völklein et al, 1990] while the lattice contribution decreases with increasing temperature proven by experiment and simulation, [Satterthwaite et al, 1957; Huang et al, 2008] we assume that at low temperature the bipolar contribution is negligible compared to the lattice contribution that is estimated as $k_l = k_{total} - k_e$ that can be used to determine the fitting parameters R_k and n. After that we can use Equation 6.3 to predict the high-temperature range lattice thermal conductivity and finally obtain the contribution of the bipolar effect at the high temperature range with the results shown in Figure 6.5. For the $PbTe/Bi_2Te_3$ = 27:1 sample (Figure 6.5B), the fitting results shows that the Kapitza resistance increases with temperature with an approximately linear dependence ($\beta \approx 1$), which makes the total thermal conductivity decrease with temperature more quickly than both bulk PbTe and

bulk Bi_2Te_3. At temperatures of 300 and 650 K, the values of R_k are approximately 1.04×10^{-8} $m^2 \cdot K \cdot W^{-1}$ and 1.88×10^{-8} $m^2 \cdot K \cdot W^{-1}$ determined by fitting the experimental thermal conductivity data at low temperature, respectively, which are of the same order as the bulk thermal resistance and cannot be neglected, as the phonon mean free path of bulk PbTe and bulk Bi_2Te_3 are of same order as the grain size $d \approx 30$ nm. The total thermal conductivity is mostly contributed by lattice vibration since the PbTe bipolar effect starts at around 600 K. For the PbTe/Bi_2Te_3 = 2:1 sample (Figure 6.5A) that contains more Bi_2Te_3 in which the bipolar effect becomes relevant at about 350 K, the total thermal conductivity increases dramatically with temperature above 350 K. The Kapitza resistance $R_k = 1.89 \times 10^{-8}$ $m^2 \cdot K \cdot W^{-1}$ at 320 K is higher than that of the PbTe/Bi_2Te_3 = 27:1 sample at the same temperature due to the increased fraction of Bi_2Te_3 that leads to the increased amount of compositional interfaces/grain boundaries. In conclusion, the distinct temperature dependence of the two nanowire heterostructure systems is indeed due to the different compositions, which decides the temperature at which the bipolar effect becomes dominant. More importantly, the well-preserved compositional interfaces/grain boundaries in the nanocomposite samples result in the large Kapitza resistance, thus leading to the extremely low thermal conductivity in both samples.

6.7 Conclusion

To summarize, we have developed a rational synthesis of PbTe–Bi_2Te_3 "barbell" nanowire heterostructures through a solution-phase one-pot three-step reaction. Through the control of the ratio between PbTe and Bi_2Te_3, the thermoelectric properties can be

manipulated to achieve a largely reduced thermal conductivity and enhanced thermoelectric figure of merit (ZT) of 1.2 at 620 K.

CHAPTER 7. THERMOELECTRIC PROPERTIES OF SILVER TELLURIDE–BISMUTH TELLURIDE NANOWIRE HETEROSTRUCTURE SYNTHESIZED BY SITE-SELECTIVE CONVERSION

In this chapter, I will introduce the solution-phase synthesis of silver telluride and bismuth telluride nanowire heterostructure using tellurium (Te) nanowire as sacrificial template and site-selective conversion strategy. High-resolution transmission electron microscope studies confirm sharp interface with possible epitaxial growth between silver telluride and bismuth telluride regions. Through tuning the precursor amount (bismuth and silver precursors) during the reaction, the composition between silver telluride and bismuth telluride can be adjusted. Moreover, the mass produced powder of nanowire heterostructure is consolidated into nanocomposite pellets, and thermoelectric properties of the nanocomposite pellets are investigated between 300 and 400 K. Results show that our materials are p-type with reduced lattice thermal conductivity and a ZT of ~0.41 at 400 K, which is the best reported value for p-type silver telluride. The results of this research have been published on Chemistry of Materials in 2014 [Fang et al, 2014a].

7.1 Introduction

Nanowire heterostructures have benefited a tremendous number of emerging areas, such as nanowire transistors [Lauhon et al, 2002; Lu et al, 2005b; Xiang et al, 2006; Li et al,

2006], photon detectors [Borgström et al, 2005; Panev et al, 2003], photovoltaics [Tian et al, 2007; Dong et al, 2009; Garnett et al, 2010], and so on, mainly due to the unique feature that nanowire heterostructures can take advantage of functions of individual components as well as interfaces between them. Thermoelectrics, as an intensively explored field, could potentially benefit from nanowire heterostructures. The well-engineered thermoelectric materials of enhanced ZT (figure of merit) by advanced techniques, such as energy filtering, modulation doping, and all-scale hierarchical nanostructuring for thermal conductivity reduction, are binary-phase systems that could be realized by nanowire heterostructures. Researchers have developed various methods of synthesizing and fabricating nanowire heterostructures [Barth et al, 2010; Buck et al, 2013; Liu et al, 2012; Liu et al, 2013; Hong et al, 2014], which is essential for the research of nanowire heterostructures in thermoelectrics.

Previously, Ag_2Te nanostructures have been synthesized from a variety of methods, such as solvothermal reaction [Zhang et al, 2006; Qin et al, 2007; Li et al, 2008; Jiang et al, 2010; Xiao et al, 2010], electrodeposition [Chen et al, 2002], microwave-assisted solution reaction [Pei et al, 2014], and Te nanowire template assisted synthesis [Mu et al, 2005; Moon et al, 2010]. Our Ag_2Te–Bi_2Te_3 nanowire heterostructure is synthesized by converting the Te part in previously discussed Te–Bi_2Te_3 nanowire heterostructure into Ag_2Te using $AgNO_3$ as precursor in ethylene glycol at room temperature. Suggested by previous reports [Moon et al, 2010; Ayyappan et al, 1996; Jeong et al, 2005], the reaction mechanism is that ethylene glycol reduces Ag^+ to Ag atoms, which then diffuse into the lattice of Te nanowire to form Ag_2Te nanowire. After the synthesis, the Ag_2Te–

Bi_2Te_3 nanowire heterostructures are hot pressed into bulk binary-phase nanocomposites (majority phase, Ag_2Te; minority phase, Bi_2Te_3) for thermoelectric property investigation. As a matter of fact, Ag_2Te has been historically studied as a promising thermoelectric material. Intensive alloying of Ag_2Te with a third element (around 50%), such as Sb (p-type) [Zhang et al, 2011c] and Se (n-type) [Drymiotis et al, 2013], is necessary to obtain decent ZT. Nanostructured materials, especially multiple-phase composite systems, have been proven to be effective for enhancing thermoelectric performance, due to selective filtering of low energy electrons (improved Seebeck coefficient) and enhanced phonon scattering (reduced thermal conductivity) at the interfaces of nanograins. However, to the best of the authors' knowledge, few papers have reported complete thermoelectric properties of Ag_2Te–Bi_2Te_3 nanocomposites or even Ag_2Te nanostructure in the literature [Cadavid et al, 2013]. Therefore, aside from the synthesis strategy, it is still worthwhile to measure the thermoelectric properties and explore potential application of Ag_2Te–Bi_2Te_3 nanowire heterostructure in thermoelectrics, even though carrier concentration optimization has not yet been done at this stage.

7.2 Synthesis Procedure

The synthesis of Ag_2Te–Bi_2Te_3 heterostructure is built on our method of growing Te–Bi_2Te_3 heterostructure with an additional step of converting Te nanowire into Ag_2Te nanowire (Figure 7.1A). Tellurium dioxide (TeO_2, 99%+), ethylene glycol (EG, 99%+), potassium hydroxide (KOH, 90%), polyvinylpyrrolidone (PVP-40, technical grade), hydrazine hydrate solution ($N_2H_4 \cdot H_2O$, 80%), and bismuth nitrate pentahydrate ($Bi(NO_3)_3 \cdot 5H_2O$, 98%)) were purchased from Sigma-Aldrich. Silver nitrate ($AgNO_3$,

99%) was purchased from Alfa-Aesar. All the chemicals are used without further purification. The synthesis is carried out in a standard Schlenk line with nitrogen protection. Heterostructures of two compositions were synthesized in this particular research, in which Bi_2Te_3 molar percentages are 4.4% (BT4) and 15.2% (BT15), respectively. In a typical process, 1.5 mmol of TeO_2, 10 mmol of KOH, and 0.3 g of PVP-40 are dissolved in 15 mL of EG at 98 °C to form a transparent yellow solution. Then 0.15 mL of hydrazine hydrate is injected to trigger Te nanowire growth. After 1 h, the reaction temperature is raised to 110 °C and then 5 mL of 0.02 M (BT4) or 0.12 M (BT15) $Bi(NO_3)_3 \cdot 5H_2O$/EG solution is injected into the reaction slurry. The reaction continues for 1 h (BT4) or 2 h (BT15) before it cools down to room temperature. The Te–Bi_2Te_3 heterostructure is washed with deionized water three times before being redispersed in 30 mL of EG. Afterward, 5 mL of 0.54 M (BT4) or 0.36 M (BT15) $AgNO_3$/EG solution is injected into the Te–Bi_2Te_3/EG slurry dropwisely to convert Te into Ag_2Te nanowires. Notably, 1.5 times more than stoichiometric amount of Ag precursor is added in the synthesis of BT15 in order to achieve stoichiometric molar percentage of Ag, Bi, and Te. Otherwise, a stoichiometric amount of Ag precursor in the synthesis of BT15 gives rich Te by 7.2% in the final product. The reaction is stirred vigorously for 1 h at room temperature, and then the final product is washed with deionized water 3 times and alcohol (190 proof) 2 times.

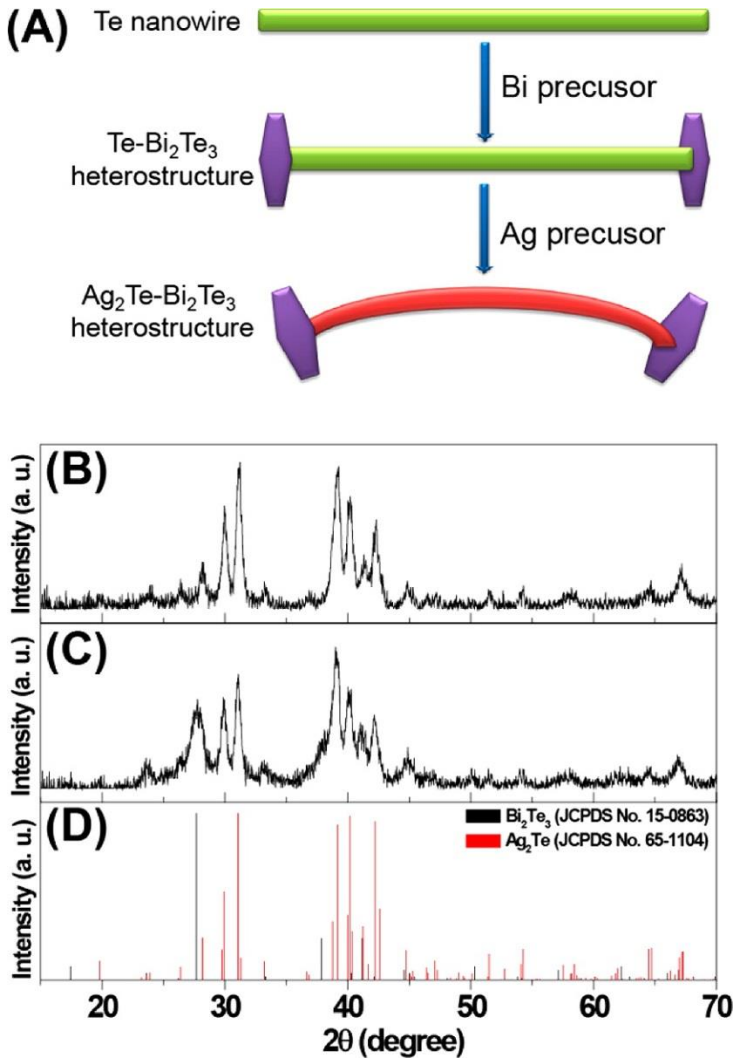

Figure 7.1. (A) Schematic demonstration of the three-step synthesis of Ag_2Te–Bi_2Te_3 nanowire heterostructure. (B) and (C) XRD spectra of Ag_2Te–Bi_2Te_3 heterostructures with Bi_2Te_3 molar percentage of 4.4% and 15.2%, respectively. (D) Standard XRD spectrum of Bi_2Te_3 (black spikes) and Ag_2Te (red spikes). [Adapted from reference Fang et al, 2014a]

7.3 Results of Materials Characterization

The as synthesized Ag_2Te–Bi_2Te_3 heterostructures were first characterized with XRD (Figure 7.1B–D). The spectra of the heterostructures of both compositions can be indexed as Ag_2Te (JCPDS No. 65-1104) and Bi_2Te_3 (JCPDS No. 15-0863) without any impurity

identified, but the (0 1 5) and (1 0 10) peaks of Bi_2Te_3 significantly broaden the peaks at around 27.65° and 39.08°, respectively, in the spectrum of BT15 while the corresponding peaks in the spectrum of BT4 are much narrower due to the Bi_2Te_3 concentration difference in the two samples.

Table 7.1. Molar Percentage of Ag, Te, and Bi

heterostructures	Ag (%)	Te (%)	Bi (%)
BT4	61.1 ± 0.1	36.0 ± 0.1	2.8 ± 0.1
BT15	51.3 ± 0.5	39.4 ± 0.3	9.2 ± 0.2

The molar percentage of Ag, Te, and Bi of BT4 and BT15 was measured by EDS, and the data are shown in Table 7.1. The results show that the elements have a nearly stoichiometric ratio with 1.2 ± 0.1% excessive Te and 0.1 ± 0.2% deficient Te in BT4 and BT15 sample, respectively. According to the molar percentage of elements, the calculated composition of BT4 is 95.6% Ag_2Te and 4.4% Bi_2Te_3 and the calculated composition of BT15 is 84.8% Ag_2Te and 15.2% Bi_2Te_3.

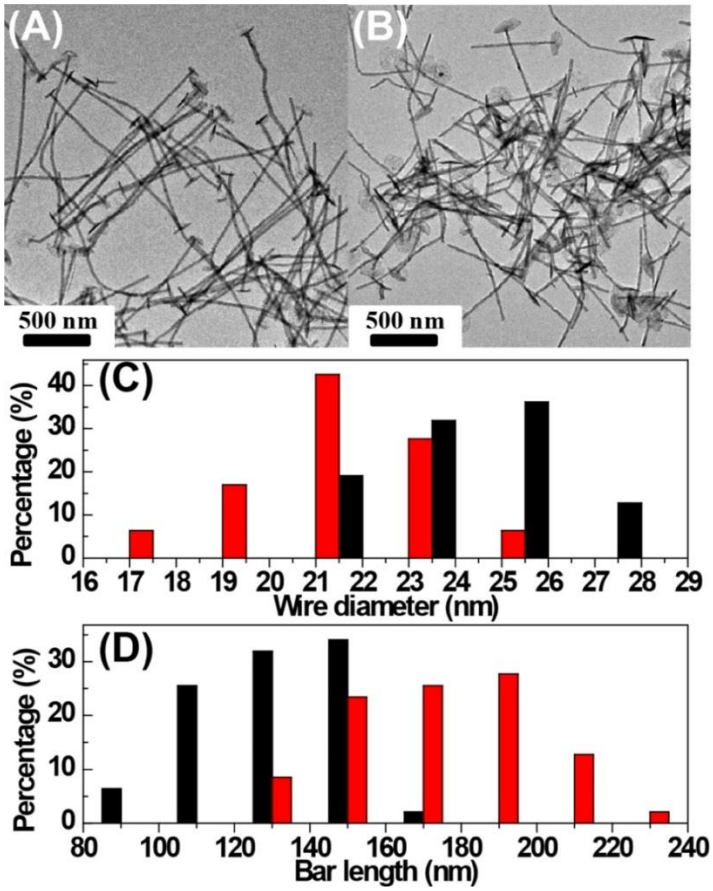

Figure 7.2. (A) and (B) The low magnification transmission electron microscopy (TEM) image of BT4 and BT15, respectively. (C) Ag_2Te wire diameter distribution histogram of BT4 (black columns) and BT15 (red columns). (D) Bi_2Te_3 bar length distribution histogram of BT4 (black columns) and BT15 (red columns). [Adapted from reference Fang et al, 2014a]

The morphology of the Ag_2Te–Bi_2Te_3 heterostructures was studied with TEM (Figure 7.2). At first, the "barbell" morphology of Te–Bi_2Te_3 was preserved after the Te nanowire to Ag_2Te nanowire conversion, but some Ag_2Te nanowires are bent or even broken, which is because of the 98% lattice volume expansion from rhombohedra (Te) to monoclinic (Ag_2Te) during the conversion [Moon et al, 2010]. A similar phenomenon has been observed in previous literature [Mu et al, 2005; Moon et al, 2010]. The statistical

study shows that the Ag_2Te nanowire diameter of BT4 is 24.95 ± 2.01 nm, slightly larger than that of BT15 (21.06 ± 2.10 nm), but the average Bi_2Te_3bar length of BT4 (130.90 ± 18.69 nm) is much smaller than that of BT15 (172.37 ± 29.89 nm). The fact can be explained by the Ag_2Te and Bi_2Te_3 relative composition difference in BT4 and BT15.

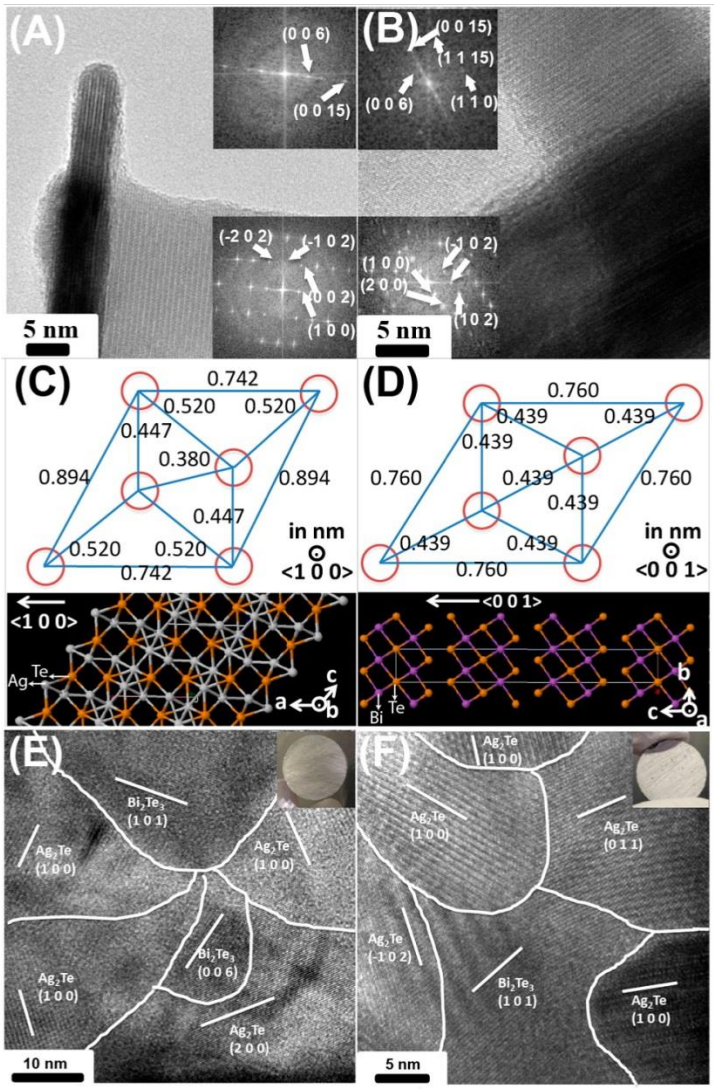

Figure 7.3. (A) and (B) High resolution TEM (HRTEM) images at the Ag_2Te nanowire and Bi_2Te_3 bar interface of BT4 and BT15, respectively. Inlaid pictures are the localized fast Fourier transforms at Bi_2Te_3 and Ag_2Te regions. (C) Te facet projection perpendicular to the longitude direction of Ag_2Te nanowire (top picture) and lattice of Ag_2Te with *b* axis pointing outward bottom picture. (D) Te facet projection perpendicular to the longitude direction of Bi_2Te_3 nanowire (top picture) and lattice of Bi_2Te_3 with *a* axis pointing outward (bottom picture). (E) and (F) HRTEM images of hot pressed pellets of BT4 and BT15, respectively. Insets are photos of the corresponding hot pressed pellets (13 mm in diameter; 2 mm in thickness). [Adapted from reference Fang et al, 2014a]

The "barbell" heterostructures were also studied with HRTEM. The lattice resolved images of BT4 (Figure 7.3A) and BT15 (Figure 7.3B) clearly demonstrated a sharp interface between Ag_2Te nanowire and Bi_2Te_3 bar. Moreover, the fast Fourier transform (FFT) on the HRTEM images (insets of Figure 7.3A,B) confirms the pure phase of Ag_2Te and Bi_2Te_3 and illustrates that the longitude directions of Ag_2Te bar and Bi_2Te_3 are ⟨1 0 0⟩ and ⟨0 0 1⟩, respectively. Based on XRD data, the lattice constants of Ag_2Te (β-phase) and Bi_2Te_3 are a = 8.162 Å, b = 4.467 Å, c = 8.973 Å, α = 90°, β = 124.153°, γ = 90° and a = 4.386 Å, b = 4.386 Å, c= 30.497 Å, α = 90°, β = 90°, γ = 120°. The lattices of Ag_2Te and Bi_2Te_3 are shown in the bottom pictures of Figure 7.3C and Figure 7.3D with b axis and a axis pointing outward, respectively, and the horizontal directions are the longitude directions of Ag_2Te nanowire and Bi_2Te_3 bar. Based on the lattice constants and geometry, one primitive cell of Te facet projections perpendicular to the ⟨1 0 0⟩ direction of Ag_2Te and the ⟨0 0 1⟩ direction of Bi_2Te_3 are drawn out in the top pictures of Figure 7.3C and Figure 7.3D, respectively. Although the HRTEM images suggested a possible epitaxial growth between the two lattices, the lattice mismatch will be as high as 10.57%, which can be calculated from distance discrepancy between the Te atoms in the projections of Ag_2Te and Bi_2Te_3 along the longitude directions. In addition, considering that the Te facets of Ag_2Te tilt for 34.153° along the longitude direction (Figure 7.3C, bottom picture), a larger lattice strain is expected at the interface. The lattice mismatch analysis and 3D images of Ag_2Te and Bi_2Te_3 lattices were finished with the help of Jmol (an open-source Java viewer for chemical structures in 3D; http://www.jmol.org/).

7.4 Results of Thermoelectric Properties Measurement

To investigate the thermoelectric properties of the Ag_2Te–Bi_2Te_3 heterostructures, the as synthesized products were washed with diluted hydrazine to strip off surfactants and then hot pressed into millimeter-thick bulk pellets (inlaid photos, Figure 7.3E,F) at 165 MPa and 150 °C. The density of pellets is calculated from mass and geometry, and the pellets of BT4 and BT15 have relative density of 86.69% and 81.44%, respectively. HRTEM was used to examine the microstructure of hot pressed pellets of BT4 and BT15 (Figure 7.3E,F). Nanoscale grains and boundaries are well preserved after hot press, but the oriented growth between Ag_2Te and Bi_2Te_3 in as synthesized heterostructures disappears and nanograins of Ag_2Te and Bi_2Te_3 illustrate random orientations in the hot pressed pellets. Afterward, thermoelectric properties are measured on the pellets. The Seebeck coefficient (S) is measured by bridging the sample between a heater and heat sink and testing the voltage and temperature difference between the hot and the cold sides. Electrical conductivity (σ) is measured with a standard four-probe Van der Pauw method, and thermal conductivity (κ) is calculated via the equation $\kappa = \alpha\rho C_p$ (ρ is the density). Thermal diffusivity (α) is measured through the laser flush method, and heat capacity (C_p) is taken to be value of the DuLong–Petit limit (0.2164 J/m-K for BT4 and 0.2096 J/m-K for BT15). All the measurements are carried out under vacuum in the temperature range from 300 to 400 K, since the phase change of Ag_2Te at 415 K causes a dramatic volume expansion that damages the structural integrity of the pellets.

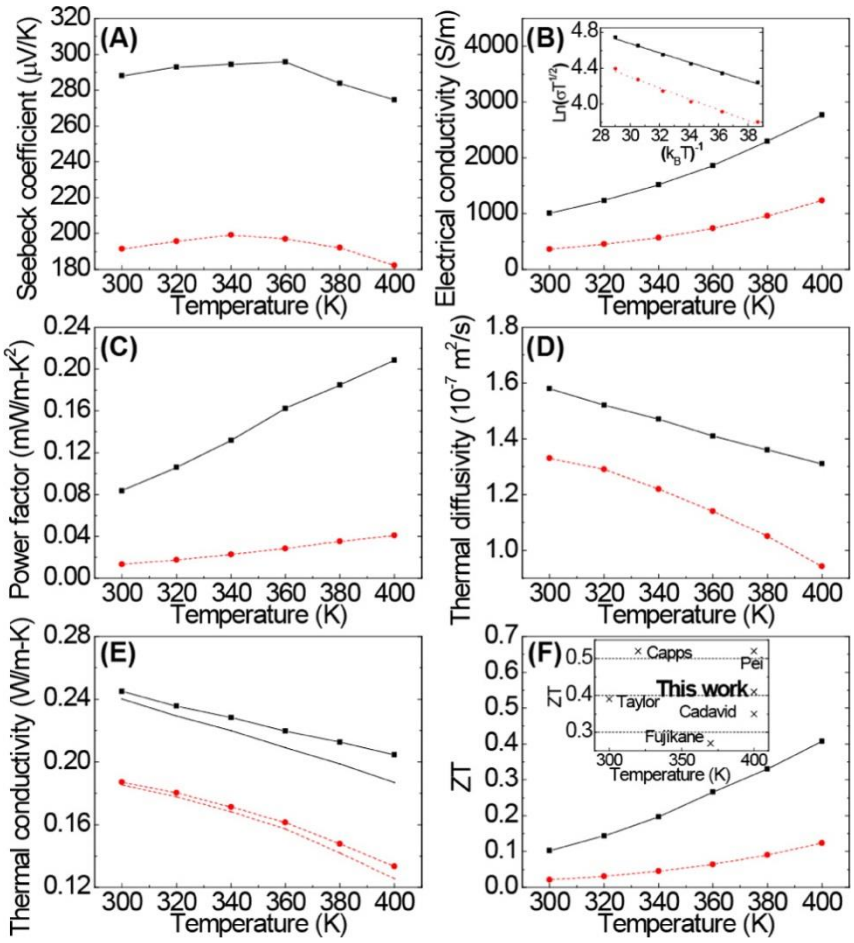

Figure 7.4. Themoelectric properties of hot pressed pellets of BT4 and BT15 between 300 and 400 K. Black squares (solid lines) and red dots (dash lines) stand for BT4 and BT15, respectively. (A) Seebeck coefficient, (B) electrical conductivity and linear fitting of $\ln(\sigma T^{1/2})$ (y) and $(k_B T)^{-1}$ (x) (inset), (C) power factor, (D) thermal diffusivity, (E) thermal conductivity (lines with squares and dots) and lattice contribution (lines without squares and dots), and (F) ZT and comparison with historical values. [Adapted from reference Fang et al, 2014a]

Figure 7.4 shows the thermoelectric properties of hot pressed pellets of BT4 and BT15 between 300 and 400 K. Both pellets show a positive Seebeck coefficient, indicating the p-type nature of our materials. However, BT4 has a larger Seebeck coefficient peaking at 295.65 μV/K (360 K) than that of BT15 peaking at 199.26 μV/K (340 K) (Figure 7.4A). Although the positive Seebeck coefficient indicates that hole transport dominates, the

Seebeck coefficient saturation at relatively low temperature also implies the nondegenerate feature of both pellets. Indeed, β-Ag_2Te (low temperature phase) has a small band gap around 0.04 eV (~$1.5k_BT$ at 300 K) [Pei et al, 2011a; Gottlieb et al, 1960; Das et al, 1983], so the contribution of thermally excited minority carriers (electron in this case) would reduce the Seebeck coefficient at relatively low temperature according to Equation 7.1 [Androulakis et al, 2010], which can explain the Seebeck coefficient temperature dependent behavior.

$$S = \frac{S_h \mu_h n_h + S_e \mu_e n_e}{\mu_h n_h + \mu_e n_e} \quad \text{.....(7.1)}$$

In Equation 7.1, μ and n are mobility and carrier concentration and footnotes h and e stand for hole and electron, respectively. According to the EDS results (Table 7.1), BT4 has 1.2% excessive Te and BT15 has 0.1% deficient Te. Previous literature reported that excessive and deficient Te in Ag_2Te give rise to p-type and n-type conduction, respectively [Pei et al, 2011a; Taylor et al, 1961]. In fact, the mobility (μ) of electron is ~6–7 times larger than that of hole in Ag_2Te [Gottlieb et al, 1960; Taylor et al, 1961], which means that a slight n-type carrier increase would significantly reduce the Seebeck coefficient according to Equation 7.1. The Te deficiency in BT15 increases the n-type carrier and leads to a smaller Seebeck coefficient than BT4. The report on the Seebeck coefficient of p-type Ag_2Te is rare; however, because the effective mass (m^*) of hole is larger than electron in Ag_2Te [Gottlieb et al, 1960; Taylor et al, 1961], it can lead to a larger p-type Seebeck coefficient in BT4 and BT15 according to the Pisarenko formula for a nondegenerate semiconductor [Androulakis et al, 2010], compared to the previously reported Seebeck coefficient of n-type Ag_2Te (between −100 μV/K and −150

μV/K) [Gadavid et al, 2013; Pei et al, 2011a; Taylor et al, 1961; Fujikane et al, 2005a; Capps et al, 2010; Fujikane et al, 2005b].

The electrical conductivity of BT4 monotonically increases from ~1000 S/m at 300 K to ~2800 S/m at 400 K while BT15 has a smaller electrical conductivity also monotonically increasing from ~360 S/m at 300 K to ~1250 S/m at 400 K (Figure 7.4B). In contrast to the electron–phonon scattering mechanism that usually causes a trend of reduced electrical conductivity with elevated temperature, we believe that a different mechanism could possibly dominate our nanocomposite system. The microstructure of the hot pressed pellets (Figure 7.3E, F) shows intensive interfaces between nanograins from Ag_2Te and Bi_2Te_3 that can create an energy barrier for the electron transport considering the band misalignment between two phases, which controls the temperature dependent behavior of electrical conductivity according to Equation 7.2 [Seto et al, 1975; Paul et al, 2010].

$$\sigma = nLe^2\left[\frac{1}{2\pi m^* k_B T}\right]^{1/2}\exp\left(-\frac{E_b}{k_B T}\right) \quad \text{.....(7.2)}$$

In Equation 7.2, L, e, k_B, T, and E_b are Lorenz number, electron charge, Boltzmann constant, temperature, and energy barrier at interfaces, respectively. First, according to Equation 7.2, electrical conductivity increases with temperature due to more electrons gaining energy that can overcome the energy barrier at elevated temperature. Second, since the Bi_2Te_3 concentration in BT15 (15.2%) is significantly larger than that (4.4%) in BT4, more interfaces and energy barriers can be created so that BT15 has a lower electrical conductivity. Assuming a carrier concentration (n) with small variation between

300 and 400 K, linear fitting of $\ln(\sigma T^{1/2})$ (y) and $(k_B T)^{-1}$ (x) (Figure 7.4B inset) gives an energy barrier (E_b) of 52 ± 1.89 meV for BT_4 and 61.19 ± 3.38 meV for BT15, which is consistent with the electrical conductivity relative magnitudes of BT4 and BT15. Based on the Seebeck coefficient and electrical conductivity, the power factor ($S^2\sigma$) of BT4 and BT15 is calculated and plotted in Figure 7.4C. The best power factor (~0.21 mW/m-K^2) is obtained in BT4 at 400 K.

Both pellets possess extremely low thermal conductivity (Figure 7.4E). From 300 to 400 K, the thermal conductivity of BT4 decreases from ~0.24 W/m-K to ~0.20 W/m-K while the thermal conductivity of BT15 decreases from ~0.19 W/m-K to ~0.13 W/m-K, which are much smaller than for bulk Ag_2Te (from ~1 W/m-K to ~0.5 W/m-K) [Cadavid et al, 2013; Pei et al, 2011a; Taylor et al, 1961; Fujikane et al, 2005a; Capps et al, 2010]. Of course, the electron contribution is quite minor because of the small electrical conductivity of both pellets in our case. However, the lattice contribution is actually reduced as well due to the nanostructures in the pellets (Figure 7.3E, F). The lattice contribution is calculated from $k_{total} - k_{electron}$ ($L\sigma T$). Due to the nondegenerate feature of both pellets, 1.59×10^{-8} WΩ/K^2 (L), 65% of the degenerate limit 2.45×10^{-8} WΩ/K^2, is used to calculate electron contribution in order not to underestimate the lattice contribution and close values of L have been used to calculate electron contribution in Ag_2Te as well as other nondegenerate material systems [Girard et al, 2012; Pei et al, 2011a; Johnsen et al, 2011]. The lattice contribution of BT4 ranges from ~0.24 W/m-K to ~0.18 W/m-K while the lattice contribution of BT15 ranges from ~0.19 W/m-K to ~0.13 W/m-K (Figure 7.4E; solid (BT4) and dashed (BT15) lines without squares and

dots), which has the edge over previously reported values (from 0.63 W/m-K to 0.15 W/m-K) [Cadavid et al, 2013; Pei et al, 2011a; Taylor et al, 1961; Fujikane et al, 2005a; Capps et al, 2010]. Comparing BT4 and BT15, the lower thermal conductivity of BT15 can be explained by more Ag_2Te–Bi_2Te_3 interfaces due to higher Bi_2Te_3 concentration.

Finally, ZT (figure of merit) is calculated based on the measured thermoelectric properties and plotted out in Figure 7.4F for BT4 and BT15. Results show that BT4 has better ZT increasing from 0.1 (300 K) to 0.41 (400 K) than BT15 whose ZT ranges between 0.02 (300 K) and 0.12 (400 K). The temperature dependent trend implies better ZT at higher temperature, but the phase transition of Ag_2Te could dramatically damage the structural integrity of the pellets, so the measurement stops at 400 K. The previously reported values of optimal ZT of Ag_2Te between 300 and 400 K have been plotted out in the inset of Figure 7.4F [Cadavid et al, 2013; Pei et al, 2011a; Taylor et al, 1961; Fujikane et al, 2005a; Capps et al, 2010]. Our best ZT (0.41) is well competitive to historical values and just a little bit lower than the best reported values (0.52) [Pei et al, 2011a; Capps et al, 2010], mainly due to the low electrical conductivity, which can be improved in future studies by doping and optimization of consolidation conditions. Notably, all the values reported by previous research in the inset of Figure 7.4F are obtained from n-type Ag_2Te, and our material represents the best results in p-type Ag_2Te.

7.5 Conclusion

In conclusion, we have successfully synthesized Ag_2Te–Bi_2Te_3 nanowire heterostructure through a solution-phase reaction. Nanocomposite pellets were fabricated from mass

produced Ag_2Te–Bi_2Te_3 nanowire heterostructure powder. Thermoelectric properties of the pellets of two compositions have been investigated. The results show that our pellets are p-type thermoelectric materials, and the best ZT achieved is 0.41 at 400 K.

During my graduate research, I mainly developed the general method to synthesize three kinds of heterostructure (Chapter 5, 6 and 7) and evaluated their thermoelectric properties without further optimization. To make use of the full potential the telluride nanowire heterostructures, some future directions are suggested:

1. Optimize the consolidation process to fabricate pellets of higher relative density.
2. Develop a way of effectively doping to optimize the carrier concentration.
3. Develop an advanced method to separately dope each phase to tune the band alignment between two phases in order to take advantages of energy filtering and modulation doping.

In the next chapter, my focus will shift to the research on nanocrystals for thermoelectric energy conversion. The method to synthesize nanocrystals (quantum dots) will not be based on the Te nanowire template assisted conversion discussed above. Since the yield of the nanocrystal synthesis is quite poor, less than 50%, large scale production is not possible, which means consolidating centimeter sized pellets is not realistic. Therefore, we use their solution to coat on other substrates, even flexible, which only requires minimal amount of produce, for potential applications in wearable device to recover body heat. My research is focused on a very specific problem that will be discussed in details in Chapter 8.

CHAPTER 8. EFFECTS OF THE SIZE AND THE DOPING CONCENTRATION ON THE POWER FACTOR OF N-TYPE PbTe NANOCRYSTALS FOR THERMOELECTRIC ENERGY CONVERSION

For the first time, we demonstrate a successful synthesis of colloidal n-type lead telluride nanocrystals doped with iodine. By tuning the reaction time and iodine concentration in the precursor solution, nanocrystals with different sizes and doping concentrations are synthesized. The Seebeck coefficient and electrical conductivity of the nanocrystals are measured on nanocrystal thin films fabricated by dip-coating glass substrates in the nanocrystals solution. Investigations on the influence of size and doping concentration on the electrical properties have been performed. The results show that the size of the nanocrystals significantly influences the electrical conductivity but not the Seebeck coefficient of nanocrystal films, while higher doping concentration leads to lower Seebeck coefficient but higher electrical conductivity in the nanocrystal films. Proof-of-concept thin-film thermoelectric modules are also fabricated using both p-type and n-type PbTe nanocrystals for the conversion of thermal energy into electrical energy. The results of this research have been published on Nano Letters in 2014 [Fang et al, 2014b].

8.1 Introduction

Manipulating the electrical properties of semiconductor nanocrystals benefits many potential applications such as thin film transistors [Talapin et al, 2009] photovoltaic solar cells [Zhang et al, 2011d], laser diodes [Klimov et al, 2007], and so forth. Recently, investigation of the potential applications of nanocrystals as thermoelectric materials [Ko et al, 2011; Urban et al, 2007; Liang et al, 2012] has been initiated due to the possible enhanced power factor σS^2, from the quantum confinement effect [Hicks et al, 1993a; Hicks et al, 1993b] and the reduced thermal conductivity from the interfacial scattering of phonons [Poon et al, 2011; Cahill et al, 2003]. Theoretical studies reveal that the quantum confinement effect, which becomes stronger as the nanocrystal size decreases, can lead to a local increase of electron density of states (DOS) near the Fermi level where the sharp features can enhance the Seebeck coefficient as predicted by the Mott equation [Heremans et al, 2012; Heremans, 2005a]. However, extensive charge hopping at the interfaces among the small nanocrystals could also hinder the electron transport although the individual nanocrystals are single-crystalline [Norris et al, 2008]. In principle, increasing the carrier concentration through doping could improve the electrical conductivity, however, there have not been many successes due to the "self-purification" of impurity in the semiconductor nanocrystals [Dalpian et al, 2006], especially those with small size. In the "self-purification" mechanism, the impurity formation energy in nanocrystals is much higher than in bulk materials. Furthermore from the kinetics perspective, the distance impurities need to travel to reach the surface of the nanocrystals is very small. Both of these facts cause a decrease of solubility of dopant impurities in nanocrystals [Dalpian et al, 2006, Du et al, 2008].

Bulk lead telluride (PbTe) and its alloys have been intensely studied as state-of-art thermoelectric materials at moderate temperature range (500–700 K) [LaLonde et al, 2011a]. Recently, PbTe nanocrystal (p-type) films, which can be fabricated into flexible thermoelectric materials by dip-coating p-type PbTe nanocrystals on flexible fibers, were found to have high Seebeck coefficient (over 1000 μV/K) [Liang et al, 2012]. However, no one has ever synthesized and systematically investigated the thermoelectric properties of n-type PbTe nanocrystals. Bulk n-type PbTe, which is typically doped with iodine (I), has been shown to possess a high ZT of 1.4 around 720 K [LaLonde et al, 2011b]. In the PbTe bulk crystal, iodine replaces tellurium in the lattice and contributes one extra electron to the conduction band of PbTe [LaLonde et al, 2011b]. Successful application of the same iodine dopants to nanocrystal systems greatly depends on the synthetic methods used and including dopant impurities in precursor solutions in colloidal synthesis has proven to be the most effective way [Norris et al, 2008]. Herein, we report a strategy to use a solution-phase reaction to synthesize colloidal I-doped PbTe nanocrystals. We also investigate the effects of the particle size and doping concentration on the Seebeck coefficient, electrical conductivity, and power factor of the nanocrystals by measuring the nanocrystal thin films coated on the glass substrates. In addition, we also demonstrate successful fabrication of thin-film thermoelectric modules using both p-type and n-type PbTe nanocrystals for the conversion of thermal energy into electrical energy.

8.2 Synthesis Procedures

The synthesis procedure of iodine-doped PbTe nanocrystals is a modified version of the method reported in our previous paper [Liang et al, 2012]. The reaction is carried out in an oxygen free environment in a standard Schlenk line setup. The chemicals used in the reactions: 1-octadecene (ODE, 90%), oleic acid (OA, 90%), lead(II) oxide (PbO, 99.9+%), and tellurium powder (99.8%) are purchased from Sigma-Aldrich; tri-n-octylphosphine (TOP, 97%) is purchased from Strem Chemicals. Iodine pellets (I_2, 99.9%) are purchased from EMD Chemicals. All of the chemicals are used as received without further purification. In a typical synthesis, 1 mmol PbO powder is dissolved in 12.7 mL of ODE and 0.75 mL of OA at 105 °C in a three-neck flask. The solution is evacuated for 2 h to remove water and oxygen trapped in the solvent and then the reaction flask is refilled with nitrogen. Meanwhile, 1.5 mmol Te powder and a desired amount of iodine pellets (0.0130 g for lower doping level or 0.0160 g for higher doping level) are dissolved in 4 mL TOP-Te at 60 °C in the glovebox, which changes the color of TOP-Te solution from yellow to orange. The temperature of the Pb precursor solution is raised to 150 or 157 °C and then the TOP-Te/I precursor is hot injected into the Pb precursor solution, which turns into dark brown color immediately. The reaction is kept for 3 min at 150 °C for ~12 nm nanocrystals synthesis, 6 min at 150 °C for ~29 nm nanocrystals synthesis, or 6 min at 157 °C for ~48 nm nanocrystals synthesis. After that, the reaction is quickly quenched by immersing the three-neck flask into a cool water bath. When the temperature reaches room temperature, the product is collected and washed with the hexane and acetone mixture three times.

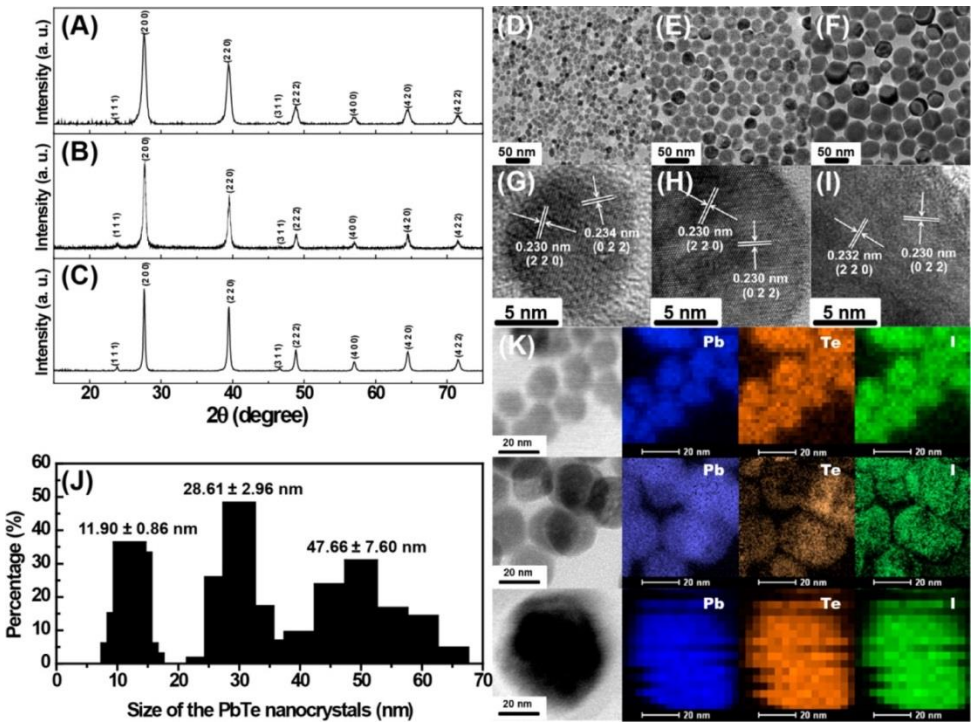

Figure 8.1. XRD patterns of (A) ~12 nm nanocrystals, (B) ~29 nm nanocrystals and (C) ~48 nm nanocrystals. (D–F) Low-magnification TEM images of the ~12, ~29, and ~48 nm nanocrystals, respectively. (G–I) High-resolution TEM images of the ~12, ~29, and ~48 nm nanocrystals, respectively and the lattices can be indexed as PbTe. (J) Histogram of the sizes distribution of the ~12 nm nanocrystals (left), ~29 nm nanocrystals (middle), and ~48 nm nanocrystals (right). (K) Scanning TEM images and elemental mapping of Pb, Te, and I of ~12 nm nanocrystals (upper panels), ~29 nm nanocrystals (middle panels), and ~48 nm nanocrystals (lower panels). [Adapted from reference Fang et al, 2014b]

8.3 Results of Materials Characterization

The as-synthesized nanocrystals with three different sizes are first characterized with XRD (Figure 8.1A–C) and TEM (Figure 8.1D–I). All three XRD spectra can be readily indexed into PbTe (JCPDS No. 38-1435) without any impurity peaks, such as PbI_2. Notably, the full width at half-maximum (fwhm) of the XRD peaks becomes smaller as nanocrystal sizes increase. Low-magnification TEM images (Figure 8.1D–F) taken on the three different batches confirm the nanocrystal morphology as well as the size difference

designed intentionally by the synthetic approach. Statistical analysis (Figure 8.1J) on Figure 8.1D–F shows that the average sizes of the nanocrystals are 11.90 ± 0.86, 28.61 ± 2.96, and 47.66 ± 7.40 nm. Notably, the ~48 nm nanocrystals have a much wider size distribution than the ~12 and ~29 nm ones, which is probably because of the Ostwald ripening as nanocrystals grow larger [Yin et al, 2005; Peng et al, 2001]. Moreover, the HRTEM studies (Figure 8.1G–I) show the lattice-resolved images of the PbTe nanocrystals, which further infer the single crystalline nature of the nanocrystals. In addition, elemental mapping studies (Figure 8.1K) using scanning transmission electron microscopy (STEM) prove that the dopants of iodine are uniformly distributed in the ~12 nm nanocrystals (upper panels; energy dispersive spectroscopy detection result), the ~29 nm nanocrystals (middle panels; electron energy loss spectroscopy detection result) and the ~48 nm nanocrystals (lower panels; energy dispersive spectroscopy detection result) PbTe nanocrystals, which, combined with the missing impurity peaks from PbI_2 in the XRD spectra (Figure 8.1 A-C), demonstrate the effectiveness of the synthesis of doping I into PbTe nanocrystals.

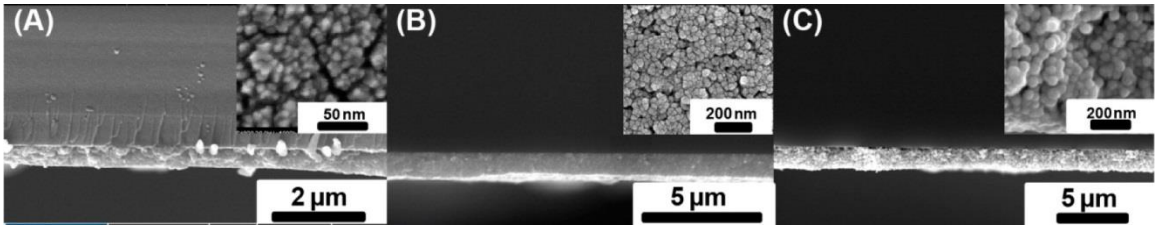

Figure 8.2. Cross section SEM images of the nanocrystal films: (A) ~12 nm nanocrystal film, (B) ~29 nm nanocrystal film, and (C) ~48 nm nanocrystal film. The inset images are high-magnification SEM images of the ~12 nm (A), ~29 nm (B), and ~48 nm (C) nanocrystal films, respectively. [Adapted from reference Fang et al, 2014]

8.4 Thin Film Fabrication

The electrical conductivity and the Seebeck coefficient of the PbTe nanocrystals with different sizes and doping concentrations are studied through the thin film measurements. In a typical process, PbTe nanocrystals from the synthesis are dispersed into chloroform to form a uniform coating solution. Then, cleaned glass slides (1.8 cm by 1.8 cm) are immersed into a nanocrystal solution for 2 min and slowly pulled out and immersed in a hydrazine hydrate aqueous solution (~1% by volume) for 1 min to remove the surface ligands. The glass slides are rinsed with acetonitrile and blow-dried with air flow. The process is repeated for 15 to 20 cycles to achieve the desired PbTe nanocrystal coating thickness. Finally, the glass slides with nanocrystal coatings are annealed at 350 °C for 2 h in forming gas (4% of hydrogen and 96% of nitrogen by volume) in order to completely remove organic ligands on the nanocrystals. The cross sections of the nanocrystal films are examined with SEM studies (Figure 8.2A–C) that show that the films are relatively uniform in thickness while the high-magnification images of the nanocrystal films (Figure 8.2A–C insets) exhibit that the films consist of interconnected nanocrystals with nearly the same sizes as prior to the annealing. EDS (Table 8.1) is used to identify the I concentration in PbTe nanocrystal films. In order to investigate the effects of the size and the I concentration on thermoelectric properties, six different types of nanocrystal thin film samples are prepared: Sample 1, nanocrystal film made from ~12 nm nanocrystals with I concentration of 5.03%; Sample 2, nanocrystal film made from ~12 nm nanocrystals with I concentration of 4.12%; Sample 3, nanocrystal film made from ~29 nm nanocrystals with I concentration of 5.42%; Sample 4, nanocrystal film made from ~29 nm nanocrystals with I concentration of 4.03%; Sample 5, nanocrystal film made

from ~48 nm nanocrystals with I concentration of 5.05%; Sample 6, nanocrystal film made from ~48 nm nanocrystals with I concentration of 3.70%.

Table 8.1. A summary of EDS results and sizes of all the sample identified with numbers from 1 – 6.

Sample ID	Lead (%)	Tellurium (%)	Iodine (%)	Size (nm)
Sample 1	47.90	47.07	5.03	~12
Sample 2	49.53	46.35	4.12	~12
Sample 3	47.24	47.34	5.42	~29
Sample 4	47.02	48.95	4.03	~29
Sample 5	47.60	47.35	5.05	~48
Sample 6	48.15	48.15	3.70	~48

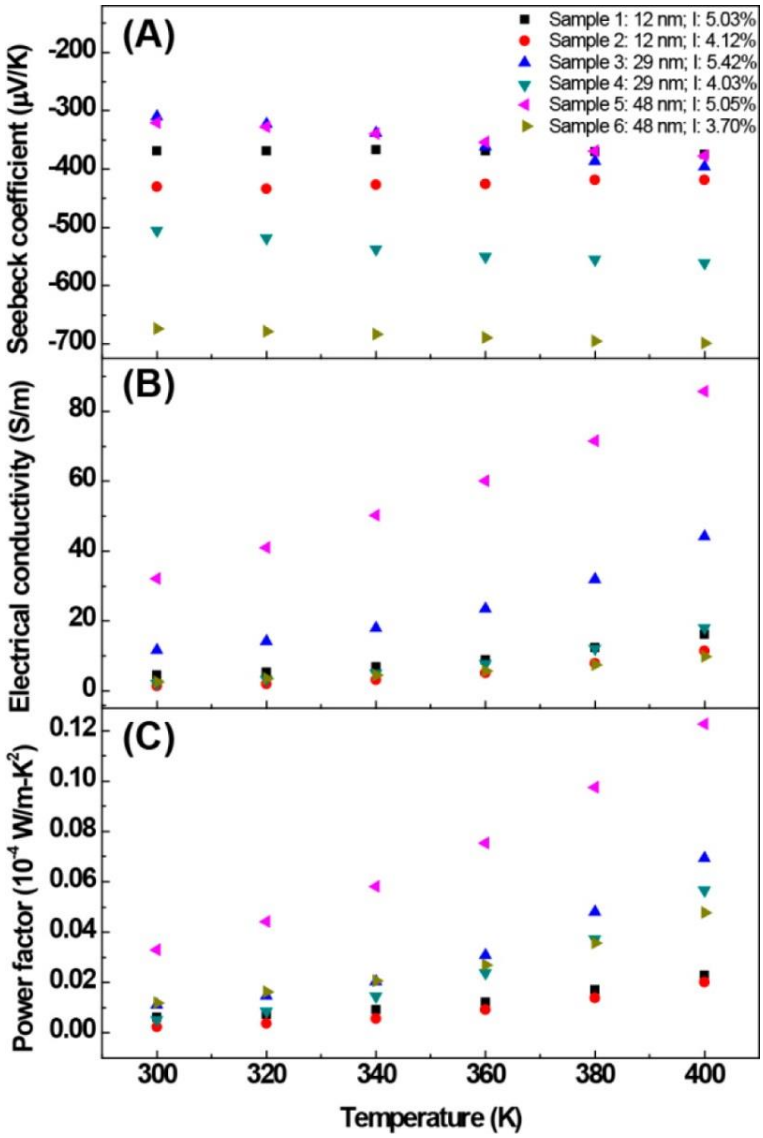

Figure 8.3. Seebeck coefficient (A), electric conductivity (B), and power factor (C) comparison between the ~12 nm nanocrystal films with I concentration of 5.03% (black squares) and 4.12% (red dots), the ~29 nm nanocrystal films with I concentration of 5.42% (blue upwared pointing triangles) and 4.03% (dark cyan downward pointing triangles), and the ~48 nm nanocrystal films with I concentration of 5.05% (Megenta left upwared pointing triangles) and 3.70% (dark yellow right pointing triangles) from 300 to 400 K. [Adapted from reference Fang et al, 2014b]

8.5 Results of Thermoelectric Properties Measurement

Figure 8.3 shows the temperature-dependent electrical conductivity and Seebeck coefficient between 300 and 400 K measured on the six nanocrystals film samples described in Table 8.1. The Seebeck results (Figure 8.3A) reveal a few interesting points: first, all six samples show negative Seebeck coefficients with absolute values between 300 and 700 μV/K, while our previous research on the undoped ~12 nm PbTe nanocrystal film fabricated with the same procedures has a positive Seebeck coefficient [Liang et al, 2012], which proves that indeed the iodine doping has effectively converted the PbTe nanocrystals from p-type into n-type; second, the three films made of ~12 nm (Sample 1), ~29 nm (Sample 3), and ~48 nm (Sample 5) nanocrystals with similar I concentration (around 5%) have nearly the same Seebeck coefficient despite of their size difference. In addition, the absolute value of Seebeck coefficient of Sample 1 is smaller than that of Sample 2, which has a lower iodine concentration (around 4%). The same fact can be found when comparing Sample 3 and Sample 4 or Sample 5 and Sample 6. These results indicate that the Seebeck coefficient is mostly affected by the I concentration of each sample rather than the nanocrystal sizes, which is more clearly demonstrated by Seebeck coefficient v.s. carrier concentration at 300 K in Figure 8.4. This can be explained by the trend found in bulk I doped PbTe [LaLone et al, 2011b; Snyder et al, 2008; Pei et al, 2011b], which is that the Seebeck coefficient decreases with increasing doping concentration.

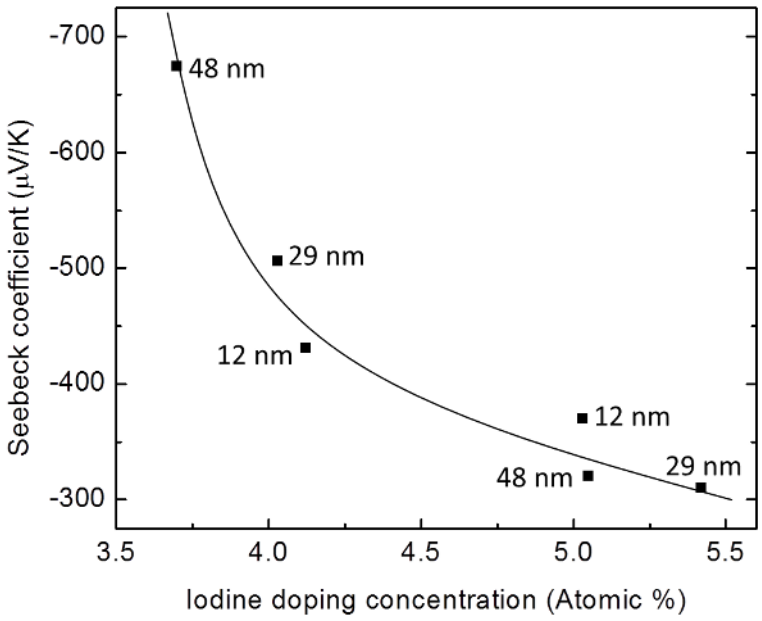

Figure 8.4. The plot of Seebeck coefficient at 300 K against iodine doping concentration.

The electrical conductivity (Figure 8.3B) of the six samples increases with temperature but it is lower than iodine-doped bulk PbTe sample, (130) mainly due to the interparticle gaps in the film identified in SEM picture (Insets, Figure 8.2A–C). Interestingly, by comparing the electrical conductivity of the six samples (Figure 8.3B), one can clearly find that both the I concentration and the size of the nanocrystals play important roles: first, the electrical conductivities of Sample 1, Sample 3, and Sample 5 are larger than those of Sample 2, Sample 4, and Sample 6, respectively, which indicates that the samples made from the nanocrystals of the same size but with a higher doping concentration are more electrically conductive; second, analysis of the data of Sample 1 versus Sample 3 versus Sample 5 indicates that for similar doping concentration the

samples made from larger nanocrystals are more conductive than those made from smaller nanocrystals, which could be explained by less charge hopping per unit distance in thin films made from large nanocrystals. The two conclusions can be more clearly drawn based on electrical conductivity v.s. crystal sizes at 300 K in Figure 8.5.

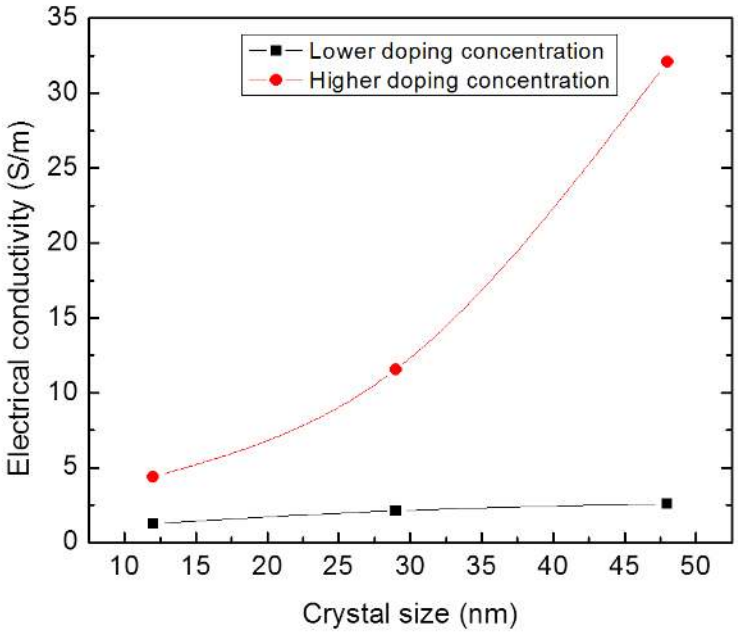

Figure 8.5. The plot of electrical conductivity at 300 K against crystal size at two iodine doping level.

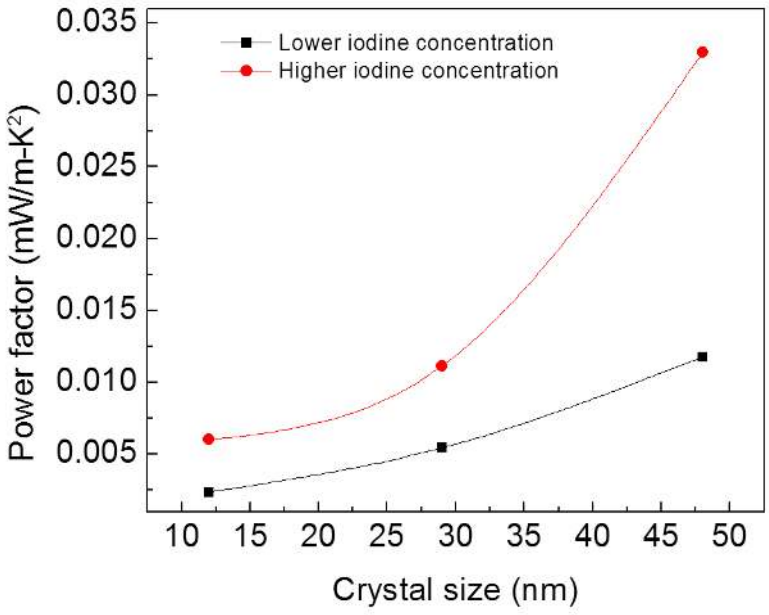

Figure 8.6. The plot of power factor at 300 K against crystal size at two iodine doping level.

The power factor of the four films are calculated and plotted in Figure 8.3C. The power factor at 300 K is plotted out against crystal size in Figure 8.6. Two conclusions can be drawn here. First, as the films made of the same size are considered, the films with a higher I concentration have higher power factor (Sample 1 versus Sample 2, Sample 3 versus Sample 4 and Sample 5 versus Sample 6); second, as the films made of nanocrystals of different sizes but with similar I concentration are considered, the films made of larger nanocrystals have higher power factor (Sample 1 versus Sample 3 versus Sample 5). The best power factor (~48 nm nanocrystal; 5.05% of I concentration) achieved here reaches 0.012 mW/m-K^2 at 400 K.

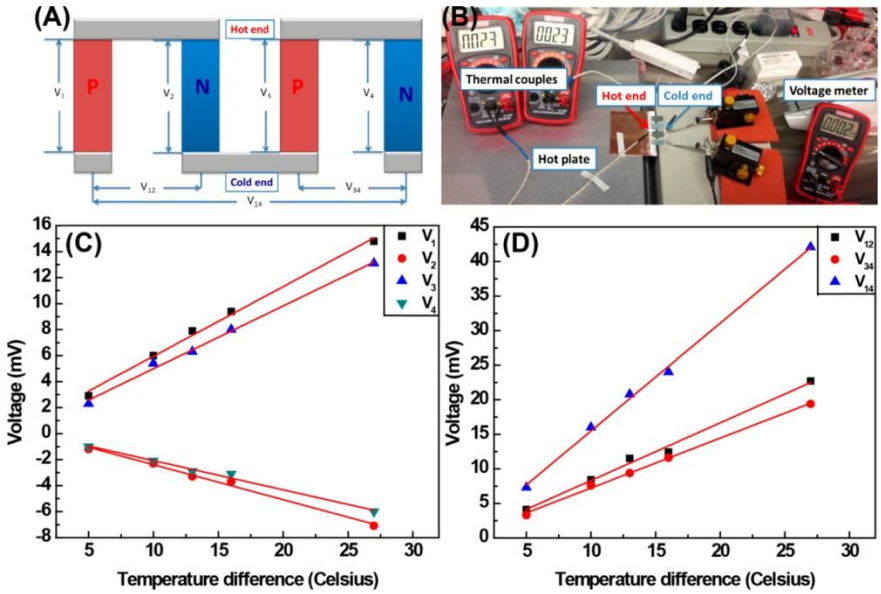

Figure 8.7. (A) Scheme of two-dimensional thermoelectric module: P and N refer to p-type and n-type nanocrystal thin film strips, respectively. V_1, V_2,V_3, and V_4 are the Seebeck voltage measured on each four strips. V_{12}, V_{34}, and V_{14} are the voltages between strips 1 and 2, strips 3 and 4, and strips 1 and 4. (B) Digital picture of the setup for measuring the temperatures and voltages of our module. (C) Seebeck voltages of the individual p-type strips (1, 3) and n-type strips (2, 4) at various temperature differences. Because the positive and the negative electrodes of the voltage meter are connected on the cold and hot ends of the strips, the p-type and the n-type strips have positive and negative voltages, respectively. (D) The voltages between strips 1 and 2, strips 3 and 4, and strips 1 and 4 at various temperature differences. [Adapted from reference Fang et al, 2014b]

8.6 Thin Film Thermoelectric Module Demonstration

The capability to rationally control the doping in PbTe nanocrystals enables us to build pure nanocrystal-based thin film thermoelectric module to convert thermal energy into electrical energy. The module is built by alternatively patterning individual thin film strips containing either p-type or n-type PbTe nanocrystals onto glass substrate and connecting the p-type and n-type strips using conductive silver paste (Figure 8.7A). The p-type nanocrystals are synthesized according to our previous report (119) and the n-type

nanocrystals are synthesized using the recipe described in this paper with size of ~48 nm nanocrystals and 4.94% I doping concentration. The nanocrystals are coated onto glass substrates by dip-coating and each strip has a dimension of ~0.9 × 1.8 cm. One end of the glass substrate is attached to a piece of copper that is heated on a hot plate in order to create temperature difference between the two ends. The temperature difference and voltage are measured by two thermocouples on the hot and cold ends and one voltage meter, respectively (Figure 8.7B). The Seebeck voltage of each strip (Figure 8.7C) and voltage between strips (Figure 8.7D) are measured at various temperature differences with the positive and the negative electrodes of the voltmeter being connected to the cold and the hot ends of the individual strip respectively. The p-type and the n-type strips have positive and negative voltages (Figure 8.7C) and they increase linearly with the temperature difference, which gives Seebeck coefficient of 535.5 μV/K (S_1) and 482.6 μV/K (S_3) for the p-type strips 1 and 3 and −269.1 μV/K (S_2) and −224.8 μV/K (S_4) for the n-type strips 2 and 4. The Seebeck coefficients measured here are smaller than the previous measurement due to the overestimation of the temperature difference because of the unoptimized thermal interface with large thermal resistances at the contacts. The voltages between p-n pairs 1–2, 3–4, and 1–4 also increase linearly with the temperature difference. The voltages produced per Kelvin are 834.9 μV/K (S_{12}), 722.5 μV/K (S_{34}), and 1561.2 μV/K (S_{14}), which are close to S_1–S_2 (804.6 μV/K), S_3–S_4 (707.4 μV/K), and S_1–S_2 + S_3–S_4 (1512 μV/K), respectively, indicating that the whole thermoelectric module functions properly and provides a proof-of-concept design for using both p-type and n-type PbTe nanocrystals for the fabrication of low-cost and flexible thermoelectric modules.

8.7 Conclusion

In conclusion, I-doped n-type PbTe nanocrystals have been successfully synthesized with tunable sizes and I doping concentration for the first time in the literature. The investigation on the effect of nanocrystal size and I concentration on Seebeck coefficient and electric conductivity of the nanocrystal films reveals that the Seebeck coefficient of the films is mainly decided by the I concentration whereas the electrical conductivity is influenced by both the size and the I concentration of nanocrystals. The general trends are that higher I concentration leads to higher electrical conductivity but lower Seebeck coefficient and larger crystal size results in higher electrical conductivity. The n-type and the p-type PbTe nanocrystal thin films with well-controlled electrical properties have been assembled into a fully functional proof-of-concept thermoelectric module for thermal energy harvesting.

CHAPTER 9. CONCLUSION AND FUTURE OUTLOOK

9.1 Conclusion

Thermoelectrics is a unique technique that can directly convert thermal energy to electricity or vice versa. Its potential applications include waste heat recovery and solid state cooling. Of course, the most fundamental aspect of thermoelectrics is to synthesize new materials with high efficiency of converting thermal energy to electricity. The entire thesis has been serving this sole purpose.

In Chapter 1, we derived the thermoelectric generation efficiency and coefficient of performance, and introduced the very import figure of merit, *ZT,* which was related by three intrinsic properties of materials: Seebeck coefficient, electrical conductivity and thermal conductivity. Except for the temperature difference, *ZT* is the only factor that decides the device efficiency and higher *ZT* gives better efficiency, which requires higher Seebeck coefficient and electrical conductivity but low thermal conductivity. In this chapter, we separately discussed three intrinsic materials properties and the factors that can influence them from fundamental perspectives in solid state physics. We also discussed the internal relations between those three intrinsic properties. Most importantly, the general principles for thermoelectric materials are summarized in the Chapter 1.6:

high electron mobility, low lattice thermal conductivity, large effective mass and optimized carrier concentration (Figure 1.13). Meanwhile, the knowledge conveyed in this chapter is also extensively used in my thesis research and can help the readers to understand the following chapters.

In Chapter 2, we used most of the chapter to discuss the benefits the nanostructured materials can bring to thermoelectric field. Several popular theories have been reviewed, including quantum confinement, energy filtering, modulation doping and thermal conductivity reduction. As a matter of fact, up to now, the well accepted reason for the *ZT* enhancement in nanostructured materials is the thermal conductivity reduction while maintaining relative high electron mobility. We also reviewed popular ways of synthesizing and fabricating nanostructured materials, which brought up the motivation of my thesis work: producing these thermoelectric nanomaterials in an economical yet scalable way while designing new nanostructured materials for better thermoelectric performance.

In Chapter 3, following the motivation introduced in the second chapter, we introduced our simple and flexible method of synthesizing telluride nanowires and nanowire heterostructure using Te nanowires as templates. A demonstration of scalability of our method is demonstrated by the large-scale production of Bi_2Te_3 nanowires.

In Chapter 4, we discussed our strategy of optimizing the thermoelectric performance of Bi_2Te_3 nanocomposites made from Bi_2Te_3 nanowires by doping the material system with

Se. Experiment was conducted to investigate the doping mechanism and the influence of Se doping concentration on thermoelectric properties. Theoretical calculation was also done to explain the data. Finally, enhanced thermoelectric performance was obtained and especially the power factor was improved by 60%.

In Chapter 5, 6 and 7, we discussed the synthesis method and thermoelectric properties of the innovative telluride nanowire heterostructures: Te-Bi_2Te_3, PbTe-Bi_2Te_3 and Ag_2Te-Bi_2Te_3. The synthesis is through site-selectively converting one single Te nanowire nanowire into two distinct tellurides. The binary phase nanocomposites made from the heterostructures possess extremely small thermal conductivity which leads to decent *ZT*. What makes it even more appealing is the flexibility of synthesis. By using different cation precursors during the conversion from Te template to tellurides, a whole new group of telluride nanowire heterostructures can be made with almost the same synthesis protocol. The telluride nanowire heterostructure provides a completely new platform to study not only phonon scattering but also electron transport behaviors at the interfaces of two phases that are predicted to be beneficial for thermoelectric performance, such as energy filtering and modulation doping. The two cases studied here are PbTe-Bi_2Te_3 and Ag_2Te-Bi_2Te_3. The PbTe-Bi_2Te_3 pellet has 76 % reduction compared to bulk PbTe and the Ag_2Te-Bi_2Te_3 has 62 % reduction compared to bulk Ag_2Te. Because of the low thermal conductivity of both nanocomposite pellets, competitive ZT of 1.2 is obtained at 620 K for the PbTe-Bi_2Te_3 and ZT of 0.41 is obtained at 400 K for Ag_2Te-Bi_2Te_3.

In Chapter 8, this chapter is about another nanostructure synthesized by a different method from those in previous chapters. An import aspect of this research is to obtain n-type PbTe nanocrystals; it can be coupled with as-synthesized p-type PbTe nanocrystals to compose a real thermoelectric module. We are the first one to successfully dope iodine to p-type PbTe nanocrystals and converted them into n-type. Our research proves that direct doping PbTe nanocrystal is possible with solution-phase reaction and a systematic study of the effect of size and doping concentration of nanocrystals on power factor was also conducted, which contributes to the fundamental understanding of nanocrystal thermoelectrics.

9.2 Future Outlook

Our nanocomposites synthesized from solution phase reactions have already achieved extremely low thermal conductivity, but there is still much room for optimization of electrical properties and the power factor. As discussed in the introduction, the most direct way to optimize the power factor is through tuning the carrier concentration by intentional doping. As demonstrated in Se doped Bi_2Te_3 nanocomposite research, the carrier concentration optimization can be very effective to improve thermoelectric performance of solution synthesized materials. By applying a similar strategy we hope to alter the carrier concentration in the nanowire heterostructures: PbTe-Bi_2Te_3 and Ag_2Te-Bi_2Te_3 in order to further optimize the power factor.

Another challenge is to improve the relative density and maintain an appropriate amount of nanostructuring of our nanocomposites, which is directly related to the electron

mobility. Lan recently reviewed the consolidation methods used in nanostructured bulk materials and the best materials have a relative density of 95–100% [Lan et al, 2010] which is higher than the relative density of our nanocomposites (70–80%). Controlling the amount of nanostructuring or grain sizes is also important. Too much nanostructuring leads to a small mobility that limits the electrical conductivity while too little nanostructuring leads to a high lattice thermal conductivity. Therefore, an optimized amount of nanostructuring should be obtained in order for the best thermoelectric performance. Experimentally, investigations of the influence of pressure and temperature during the pressing or sintering on the properties of nanocomposites are of major importance and we expect that optimizing the consolidation conditions will play a significant role in future improvement of thermoelectric performance.

Furthermore, we can also design our telluride heterostructures more delicately to take advantage of the interesting effects discussed in Chapter 2 for power factor improvement, such as energy filtering and modulation doping. Both effects involve two phases in the nanocomposites, which make nanowire heterostructures ideal for such investigation. Instead of worrying about the mixing uniformity of the two-phase mixture, nanowire heterostructures can provide great homogeneity in nanocomposites according to our experience. More importantly, by taking advantage of the flexibility of our material synthesis, optimization of those effects is feasible. Band alignment between two phases is very important in both effects. In energy filtering, the power factor increases first and then decreases with increasing energy barrier height generated by the band offset. In modulation doping, the doped phase should have a higher conduction band edge or lower

valence band edge for n-type or p-type doping to favor carrier movement to the matrix phase. Two telluride phases in the heterostructure can be carefully chosen or selectively doped to satisfy the requirements. The relative amounts of the two phases can also play an important role. In energy filtering, the power factor also first increases and then decreases with the concentration of the minority phase. In modulation doping, the concentration of the doped minority phase decides the carrier concentration that directly relates to power factor optimization. The composition of our heterostructures can be tuned by adjusting the ratio between precursors as demonstrated in PbTe–Bi_2Te_3 heterostructures. The flexibility of our heterostructures gives us opportunities to systematically study and optimize the energy filtering or modulation doping effects for thermoelectrics. In addition to nanowire heterostructures, metallic nanocrystals acting as nanoinclusions can also be introduced to a single-phase nanowire matrix, which provides another method for energy filtering or modulation doping studies.

All in all, the solution synthesized nanostructured materials, in spite of its unique advantages, still have much room for improvement with traditional methods. At the same time, new opportunities await in applying advance theories for further improvement of thermoelectric performance.

LIST OF REFERENCES

LIST OF REFERENCES

Lawrence Livermore National Laboratory. Energy Flow: US Energy Flow 1960. https://flowcharts.llnl.gov/ (accessed on 10/24/14).

Lawrence Livermore National Laboratory. Energy Flow: US Energy Flow 2011. https://flowcharts.llnl.gov/ (accessed on 10/24/14).

Mahan, G.; Sales, B.; Sharp, J., Thermoelectric materials: New approaches to an old problem. *Phys. Today* **1997,** *50* (3), 42-47.

Bell, L. E., Cooling, Heating, Generating Power, and Recovering Waste Heat with Thermoelectric Systems. *Science* **2008,** *321* (5895), 1457-1461.

Leonov, V.; Vullers, R. J. M., Wearable Thermoelectric Generators for Body-Powered Devices. *Journal of Electronic Materials* **2009,** *38* (7), 1491-1498.

Yang, J.; Caillat, T., Thermoelectric Materials for Space and Automotive Power Generation. *MRS Bulletin* **2006,** *31* (03), 224-229.

Kumar, S.; Heister, S.; Xu, X.; Salvador, J.; Meisner, G., Thermoelectric Generators for Automotive Waste Heat Recovery Systems Part I: Numerical Modeling and Baseline Model Analysis. *Journal of Electronic Materials* **2013,** *42* (4), 665-674.

DiSalvo, F. J., Thermoelectric Cooling and Power Generation. *Science* **1999,** *285* (5428), 703-706.

Rowe, D. M.; Bhandari, C. M. Thermoelectric Coefficients in *Modern Thermoelectrics* **1983a**, Reston Publishing Company, INC., Reston, Virginia.

Borrego, J. M., Lynden, H. M. and Blair, J. The Efficiency of Thermoelectric Generators. **1958**, WADC Technical Note 58-200, M.I.T. Industrial Liaison Office, Cambridge, Massachusetts

Rowe, D. M.; Bhandari, C. M. Generating Efficiency and the Figure of Merit in *Modern Thermoelectrics* **1983b**, Reston Publishing Company, INC., Reston, Virginia.

Penn, A. W. Small electrical power sources. *Physics in Technology* **1974,** *5* (2), 115.

Grosso, G.; Parravicini, G. P. Transport in Intrinsic and Homogeneously Doped Semiconductors in *Solid State Physics*, Academic Press: **2000**.

Goldsmid, J. H.; Thermoelectric Properties of Metals and Semiconductors in *Introduction to Themoelectricity*, Springer: **2010a**.

Cutler, M.; Mott, N. F., Observation of Anderson Localization in an Electron Gas. *Physical Review* **1969,** *181* (3), 1336-1340.

Heremans, J. P., Low-dimensional thermoelectricity. *Acta Physica Polonica A* **2005a,** *108* (4), 609-634.

Shakouri, A., Recent Developments in Semiconductor Thermoelectric Physics and Materials. *Annual Review of Materials Research* **2011,** *41* (1), 399-431.

Goldsmid, J. H. Thermoelectric Properties of Semiconductors in *Applications of Thermoelectricicity*, Methuen: **1960**.

Bhandari, C. M.; Rowe, D. M., Boundary scattering of phonons. *Journal of Physics C: Solid State Physics* **1978,** *11* (9), 1787.

Goldsmid, J. H.; Optimisation and Selection of Semiconductor Thermoelements in *Introduction to Themoelectricity*, Springer: **2010b**.

Keyes, R. W., High-Temperature Thermal Conductivity of Insulating Crystals: Relationship to the Melting Point. *Physical Review* **1959,** *115* (3), 564-567.

Rowe, D. M.; Bhandari, C. M. Elementary solid state theory and thermoelectric transport equations in *Modern Thermoelectrics* **1983c**, Reston Publishing Company, INC., Reston, Virginia.

Goldsmid, H. J., The Thermal Conductivity of Bismuth Telluride. *Proceedings of the Physical Society. Section B* **1956,** *69* (2), 203.

Chasmar, R. P.; Stratton, R., The Thermoelectric Figure of Merit and its Relation to Thermoelectric Generators†. *Journal of Electronics and Control* **1959,** *7* (1), 52-72.

Rowe, D. M.; Bhandari, C. M. Optimization of the thermoelectric figure of merit – theoretical consideration in *Modern Thermoelectrics* **1983d**, Reston Publishing Company, INC., Reston, Virginia.

Hicks, L. D.; Dresselhaus, M. S., Effect of quantum-well structures on the thermoelectric figure of merit. *Physical Review B* **1993a,** *47* (19), 12727-12731.

Hicks, L. D.; Dresselhaus, M. S., Thermoelectric figure of merit of a one-dimensional conductor. *Physical Review B* **1993b,** *47* (24), 16631-16634.

Heremans, J. P.; Wiendlocha, B.; Chamoire, A. M., Resonant levels in bulk thermoelectric semiconductors. *Energy & Environmental Science* **2012,** *5* (2), 5510-5530.

Pichanusakorn, P.; Bandaru, P., Nanostructured thermoelectrics. *Materials Science and Engineering: R: Reports* **2010,** *67* (2–4), 19-63.

Kuno, M. Introductory Nanoscience, 1st edition; Garland Science: USA, **2011**.

Heremans, J. P.; Dresselhaus, M. S., Recent Developments in Low-Dimensional Thermoelectric Materials. In *Thermoelectrics Handbook*, CRC Press: **2005b**; pp 39-1-39-24.

Heremans, J. P.; Thrush, C. M.; Morelli, D. T., Thermopower enhancement in lead telluride nanostructures. *Physical Review B* **2004,** *70* (11), 115334.

Hicks, L. D.; Harman, T. C.; Dresselhaus, M. S., Use of quantum-well superlattices to obtain a high figure of merit from nonconventional thermoelectric materials. *Applied Physics Letters* **1993c,** *63* (23), 3230-3232.

Lin, Y.-M.; Sun, X.; Dresselhaus, M. S., Theoretical investigation of thermoelectric transport properties of cylindrical Bi nanowires. *Physical Review B* **2000,** *62* (7), 4610-4623.

Lin, Y.-M.; Rabin, O.; Cronin, S. B.; Ying, J. Y.; Dresselhaus, M. S., Semimetal–semiconductor transition in Bi1−xSbx alloy nanowires and their thermoelectric properties. *Applied Physics Letters* **2002,** *81* (13), 2403-2405.

Hicks, L. D.; Harman, T. C.; Sun, X.; Dresselhaus, M. S., Experimental study of the effect of quantum-well structures on the thermoelectric figure of merit. *Physical Review B* **1996,** *53* (16), R10493-R10496.

Harman, T. C.; Taylor, P. J.; Walsh, M. P.; LaForge, B. E., Quantum Dot Superlattice Thermoelectric Materials and Devices. *Science* **2002,** *297* (5590), 2229-2232.

Balandin, A. A.; Lazarenkova, O. L., Mechanism for thermoelectric figure-of-merit enhancement in regimented quantum dot superlattices. *Applied Physics Letters* **2003,** *82* (3), 415-417.

Lin, Y.-M.; Dresselhaus, M. S., Thermoelectric properties of superlattice nanowires. *Physical Review B* **2003,** *68* (7), 075304.

Faleev, S. V.; Léonard, F., Theory of enhancement of thermoelectric properties of materials with nanoinclusions. *Physical Review B* **2008,** *77* (21), 214304.

Zebarjadi, M.; Esfarjani, K.; Shakouri, A.; Bahk, J.-H.; Bian, Z.; Zeng, G.; Bowers, J.; Lu, H.; Zide, J.; Gossard, A., Effect of nanoparticle scattering on thermoelectric power factor. *Applied Physics Letters* **2009,** *94* (20), 202105.

Zeng, G.; Zide, J. M. O.; Kim, W.; Bowers, J. E.; Gossard, A. C.; Bian, Z.; Zhang, Y.; Shakouri, A.; Singer, S. L.; Majumdar, A., Cross-plane Seebeck coefficient of ErAs:InGaAs/InGaAlAs superlattices. *Journal of Applied Physics* **2007,** *101* (3), 034502.

Heremans, J. P.; Thrush, C. M.; Morelli, D. T., Thermopower enhancement in PbTe with Pb precipitates. *Journal of Applied Physics* **2005c,** *98* (6), 063703.

Ko, D.-K.; Kang, Y.; Murray, C. B., Enhanced Thermopower via Carrier Energy Filtering in Solution-Processable Pt–Sb2Te3 Nanocomposites. *Nano Letters* **2011,** *11* (7), 2841-2844.

Sumithra, S.; Takas, N. J.; Misra, D. K.; Nolting, W. M.; Poudeu, P. F. P.; Stokes, K. L., Enhancement in Thermoelectric Figure of Merit in Nanostructured Bi2Te3 with Semimetal Nanoinclusions. *Advanced Energy Materials* **2011,** *1* (6), 1141-1147.

Zhang, Y.; Bahk, J.-H.; Lee, J.; Birkel, C. S.; Snedaker, M. L.; Liu, D.; Zeng, H.; Moskovits, M.; Shakouri, A.; Stucky, G. D., Hot Carrier Filtering in Solution Processed Heterostructures: A Paradigm for Improving Thermoelectric Efficiency. *Advanced Materials* **2014,** *26* (17), 2755-2761.

Dingle, R.; Störmer, H. L.; Gossard, A. C.; Wiegmann, W., Electron mobilities in modulation-doped semiconductor heterojunction superlattices. *Applied Physics Letters* **1978,** *33* (7), 665-667.

Friedrich, S., High-mobility Si and Ge structures. *Semiconductor Science and Technology* **1997,** *12* (12), 1515.

Zebarjadi, M.; Joshi, G.; Zhu, G.; Yu, B.; Minnich, A.; Lan, Y.; Wang, X.; Dresselhaus, M.; Ren, Z.; Chen, G., Power Factor Enhancement by Modulation Doping in Bulk Nanocomposites. *Nano Letters* **2011,** *11* (6), 2225-2230.

Yu, B.; Zebarjadi, M.; Wang, H.; Lukas, K.; Wang, H.; Wang, D.; Opeil, C.; Dresselhaus, M.; Chen, G.; Ren, Z., Enhancement of Thermoelectric Properties by Modulation-Doping in Silicon Germanium Alloy Nanocomposites. *Nano Letters* **2012,** *12* (4), 2077-2082.

Bhandari, C. M., Size Effects on Thermal Transport. In *Thermoelectrics Handbook*, CRC Press: **2005**; pp 14-1-14-15.

Chen, G.; Dames, C., Thermal Conductivity of Nanostructured Thermoelectric Materials. In *Thermoelectrics Handbook*, CRC Press: **2005**; pp 42-1-42-16.

Li, D.; Wu, Y.; Kim, P.; Shi, L.; Yang, P.; Majumdar, A., Thermal conductivity of individual silicon nanowires. *Applied Physics Letters* **2003a,** *83* (14), 2934-2936.

Dames, C.; Chen, G., Theoretical phonon thermal conductivity of Si/Ge superlattice nanowires. *Journal of Applied Physics* **2004,** *95* (2), 682-693.

Scherrer, S.; Scherrer, H., Bismuth Telluride, Antimony Telluride, and Their Solid Solutions. In *CRC Handbook of Thermoelectrics*, CRC Press: **1995**.

Venkatasubramanian, R., Lattice thermal conductivity reduction and phonon localizationlike behavior in superlattice structures. *Physical Review B* **2000,** *61* (4), 3091-3097.

Venkatasubramanian, R.; Siivola, E.; Colpitts, T.; O'Quinn, B., Thin-film thermoelectric devices with high room-temperature figures of merit. *Nature* **2001,** *413* (6856), 597-602.

Goldsmid, J. H.; Review of Thermoelectric Materials in *Introduction to Themoelectricity*, Springer: **2010c**.

Harman, T. C.; Taylor, P. J.; Spears, D. L.; Walsh, M. P., Thermoelectric quantum-dot superlattices with high ZT. *Journal of Electronic Materials* **2000,** *29* (1), L1-L2.

Li, D.; Wu, Y.; Fan, R.; Yang, P.; Majumdar, A., Thermal conductivity of Si/SiGe superlattice nanowires. *Applied Physics Letters* **2003b,** *83* (15), 3186-3188.

Hsu, K. F.; Loo, S.; Guo, F.; Chen, W.; Dyck, J. S.; Uher, C.; Hogan, T.; Polychroniadis, E. K.; Kanatzidis, M. G., Cubic AgPbmSbTe2+m: Bulk Thermoelectric Materials with High Figure of Merit. *Science* **2004,** *303* (5659), 818-821.

Poudel, B.; Hao, Q.; Ma, Y.; Lan, Y.; Minnich, A.; Yu, B.; Yan, X.; Wang, D.; Muto, A.; Vashaee, D.; Chen, X.; Liu, J.; Dresselhaus, M. S.; Chen, G.; Ren, Z., High-Thermoelectric Performance of Nanostructured Bismuth Antimony Telluride Bulk Alloys. *Science* **2008,** *320* (5876), 634-638.

Biswas, K.; He, J.; Blum, I. D.; Wu, C.-I.; Hogan, T. P.; Seidman, D. N.; Dravid, V. P.; Kanatzidis, M. G., High-performance bulk thermoelectrics with all-scale hierarchical architectures. *Nature* **2012,** *489* (7416), 414-418.

Böttner, H.; Chen, G.; Venkatasubramanian, R., Aspects of Thin-Film Superlattice Thermoelectric Materials, Devices, and Applications. *MRS Bulletin* **2006,** *31* (03), 211-217.

Mzerd, A.; Sayah, D.; Brun, G.; Tedenac, J. C.; Boyer, A., Crystal growth and sticking coefficient of Bi2Te3 thin films on Si(1 1 1) substrate. *Journal of Materials Science Letters* **1995,** *14* (3), 194-197.

Mzerd, A.; Sayah, D.; Tedenac, J. C.; Boyer, A., Crystal growth of Bi2Te3 on single-crystal substrate Sb2Te3 by molecular beam epitaxy. *International Journal of Electronics* **1994,** *77* (3), 291-300.

Beyer, H.; Nurnus, J.; Böttner, H.; Lambrecht, A.; Wagner, E.; Bauer, G., High thermoelectric figure of merit ZT in PbTe and Bi2Te3-based superlattices by a reduction of the thermal conductivity. *Physica E: Low-dimensional Systems and Nanostructures* **2002,** *13* (2–4), 965-968.

Venkatasubramanian, R.; Colpitts, T.; O'Quinn, B.; Liu, S.; El-Masry, N.; Lamvik, M., Low-temperature organometallic epitaxy and its application to superlattice structures in thermoelectrics. *Applied Physics Letters* **1999,** *75* (8), 1104-1106.

Völklein, F.; Baier, V.; Dillner, U.; Kessler, E., Transport properties of flash-evaporated (Bi1 − xSbx)2Te3 films I: Optimization of film properties. *Thin Solid Films* **1990,** *187* (2), 253-262.

Foucaran, A.; Sackda, A.; Giani, A.; Pascal-Delannoy, F.; Boyer, A., Flash evaporated layers of (Bi2Te3–Bi2Se3)(N) and (Bi2Te3–Sb2Te3)(P). *Materials Science and Engineering: B* **1998,** *52* (2–3), 154-161.

McCray, W. P., MBE deserves a place in the history books. *Nature Nanotechnology* **2007,** *2* (5), 259-261.

Chowdhury, I.; Prasher, R.; Lofgreen, K.; Chrysler, G.; Narasimhan, S.; Mahajan, R.; Koester, D.; Alley, R.; Venkatasubramanian, R., On-chip cooling by superlattice-based thin-film thermoelectrics . *Nature Nanotechnology* **2009,** *4* (4), 235-238.

Harringa, J. L.; Cook, B. A., Solid-State Synthesis of Thermoelectric Materials. In *Thermoelectrics Handbook*, CRC Press: **2005**; pp 19-1-19-18.

Suryanarayana, C., Mechanical alloying and milling. *Progress in Materials Science* **2001,** *46* (1–2), 1-184.

Joshi, G.; Lee, H.; Lan, Y.; Wang, X.; Zhu, G.; Wang, D.; Gould, R. W.; Cuff, D. C.; Tang, M. Y.; Dresselhaus, M. S.; Chen, G.; Ren, Z., Enhanced Thermoelectric Figure-of-Merit in Nanostructured p-type Silicon Germanium Bulk Alloys. *Nano Letters* **2008,** *8* (12), 4670-4674.

Ma, Y.; Hao, Q.; Poudel, B.; Lan, Y.; Yu, B.; Wang, D.; Chen, G.; Ren, Z., Enhanced Thermoelectric Figure-of-Merit in p-Type Nanostructured Bismuth Antimony Tellurium Alloys Made from Elemental Chunks. *Nano Letters* **2008,** *8* (8), 2580-2584.

Lan, Y.; Minnich, A. J.; Chen, G.; Ren, Z., Enhancement of Thermoelectric Figure-of-Merit by a Bulk Nanostructuring Approach. *Advanced Functional Materials* **2010,** *20* (3), 357-376.

Lan, Y.; Poudel, B.; Ma, Y.; Wang, D.; Dresselhaus, M. S.; Chen, G.; Ren, Z., Structure Study of Bulk Nanograined Thermoelectric Bismuth Antimony Telluride. *Nano Letters* **2009,** *9* (4), 1419-1422.

Zhao, L.-D.; Dravid, V. P.; Kanatzidis, M. G., The panoscopic approach to high performance thermoelectrics. *Energy & Environmental Science* **2014,** *7* (1), 251-268.

Biswas, K.; He, J.; Zhang, Q.; Wang, G.; Uher, C.; Dravid, V. P.; Kanatzidis, M. G., Strained endotaxial nanostructures with high thermoelectric figure of merit. *Nature Chemistry* **2011a,** *3* (2), 160-166.

Ahn, K.; Han, M.-K.; He, J.; Androulakis, J.; Ballikaya, S.; Uher, C.; Dravid, V. P.; Kanatzidis, M. G., Exploring Resonance Levels and Nanostructuring in the PbTe−CdTe System and Enhancement of the Thermoelectric Figure of Merit. *Journal of the American Chemical Society* **2010,** *132* (14), 5227-5235.

Biswas, K.; He, J.; Wang, G.; Lo, S.-H.; Uher, C.; Dravid, V. P.; Kanatzidis, M. G., High thermoelectric figure of merit in nanostructured p-type PbTe-MTe (M = Ca, Ba). *Energy & Environmental Science* **2011b,** *4* (11), 4675-4684.

Zhao, L.-D.; Hao, S.; Lo, S.-H.; Wu, C.-I.; Zhou, X.; Lee, Y.; Li, H.; Biswas, K.; Hogan, T. P.; Uher, C.; Wolverton, C.; Dravid, V. P.; Kanatzidis, M. G., High Thermoelectric Performance via Hierarchical Compositionally Alloyed Nanostructures. *Journal of the American Chemical Society* **2013,** *135* (19), 7364-7370.

Lee, Y.; Lo, S.-H.; Androulakis, J.; Wu, C.-I.; Zhao, L.-D.; Chung, D.-Y.; Hogan, T. P.; Dravid, V. P.; Kanatzidis, M. G., High-Performance Tellurium-Free Thermoelectrics: All-Scale Hierarchical Structuring of p-Type PbSe–MSe Systems (M = Ca, Sr, Ba). *Journal of the American Chemical Society* **2013,** *135* (13), 5152-5160.

Zhao, L.-D.; He, J.; Hao, S.; Wu, C.-I.; Hogan, T. P.; Wolverton, C.; Dravid, V. P.; Kanatzidis, M. G., Raising the Thermoelectric Performance of p-Type PbS with Endotaxial Nanostructuring and Valence-Band Offset Engineering Using CdS and ZnS. *Journal of the American Chemical Society* **2012a,** *134* (39), 16327-16336.

Zhao, L.-D.; Lo, S.-H.; He, J.; Li, H.; Biswas, K.; Androulakis, J.; Wu, C.-I.; Hogan, T. P.; Chung, D.-Y.; Dravid, V. P.; Kanatzidis, M. G., High Performance Thermoelectrics from Earth-Abundant Materials: Enhanced Figure of Merit in PbS by Second Phase Nanostructures. *Journal of the American Chemical Society* **2011a,** *133* (50), 20476-20487.

Zhao, L.-D.; He, J.; Wu, C.-I.; Hogan, T. P.; Zhou, X.; Uher, C.; Dravid, V. P.; Kanatzidis, M. G., Thermoelectrics with Earth Abundant Elements: High Performance p-type PbS Nanostructured with SrS and CaS. *Journal of the American Chemical Society* **2012b,** *134* (18), 7902-7912.

Zhao, Y.; Dyck, J. S.; Burda, C., Toward high-performance nanostructured thermoelectric materials: the progress of bottom-up solution chemistry approaches. *Journal of Materials Chemistry* **2011b,** *21* (43), 17049-17058.

Wang, W. Z.; Poudel, B.; Wang, D. Z.; Ren, Z. F., Synthesis of PbTe Nanoboxes Using a Solvothermal Technique. *Advanced Materials* **2005a,** *17* (17), 2110-2114.

Wang, W.; Poudel, B.; Yang, J.; Wang, D. Z.; Ren, Z. F., High-Yield Synthesis of Single-Crystalline Antimony Telluride Hexagonal Nanoplates Using a Solvothermal Approach. *Journal of the American Chemical Society* **2005b,** *127* (40), 13792-13793.

Mi, J. L.; Zhao, X. B.; Zhu, T. J.; Tu, J. P., Improved thermoelectric figure of merit in n-type CoSb3 based nanocomposites. *Applied Physics Letters* **2007,** *91* (17), 172116.

Martín-González, M.; Snyder, G. J.; Prieto, A. L.; Gronsky, R.; Sands, T.; Stacy, A. M., Direct Electrodeposition of Highly Dense 50 nm Bi2Te3-ySey Nanowire Arrays. *Nano Letters* **2003,** *3* (7), 973-977.

Wu, Y.; Fan, R.; Yang, P., Block-by-Block Growth of Single-Crystalline Si/SiGe Superlattice Nanowires. *Nano Letters* **2002,** *2* (2), 83-86.

Zhang, G.; Yu, Q.; Wang, W.; Li, X., Nanostructures for Thermoelectric Applications: Synthesis, Growth Mechanism, and Property Studies. *Advanced Materials* **2010,** *22* (17), 1959-1962.

Zhao, X. B., Solvothermal Synthesis of Nanostructured Thermoelectric Materials. In *Thermoelectrics Handbook*, CRC Press: **2005**; pp 25-1-25-10.

Foos, E. E.; Stroud, R. M.; Berry, A. D., Synthesis and Characterization of Nanocrystalline Bismuth Telluride. *Nano Letters* **2001,** *1* (12), 693-695.

Kovalenko, M. V.; Spokoyny, B.; Lee, J.-S.; Scheele, M.; Weber, A.; Perera, S.; Landry, D.; Talapin, D. V., Semiconductor Nanocrystals Functionalized with Antimony Telluride Zintl Ions for Nanostructured Thermoelectrics. *Journal of the American Chemical Society* **2010,** *132* (19), 6686-6695.

Urban, J. J.; Talapin, D. V.; Shevchenko, E. V.; Kagan, C. R.; Murray, C. B., Synergism in binary nanocrystal superlattices leads to enhanced p-type conductivity in self-assembled PbTe/Ag2Te thin films. *Nature Materials* **2007,** *6* (2), 115-121.

LaLonde, A. D.; Pei, Y.; Wang, H.; Jeffrey Snyder, G., Lead telluride alloy thermoelectrics. *Materials Today* **2011a,** *14* (11), 526-532.

Finefrock, S. W.; Fang, H.; Yang, H.; Darsono, H.; Wu, Y., Large-scale solution-phase production of Bi2Te3 and PbTe nanowires using Te nanowire templates. *Nanoscale* **2014a,** *6* (14), 7872-7876.

Wang, K.; Liang, H.-W.; Yao, W.-T.; Yu, S.-H., Templating synthesis of uniform Bi2Te3 nanowires with high aspect ratio in triethylene glycol (TEG) and their thermoelectric performance. *Journal of Materials Chemistry* **2011,** *21* (38), 15057-15062.

Song, J.-M.; Lin, Y.-Z.; Zhan, Y.-J.; Tian, Y.-C.; Liu, G.; Yu, S.-H., Superlong High-Quality Tellurium Nanotubes: Synthesis, Characterization, and Optical Property. *Crystal Growth & Design* **2008,** *8* (6), 1902-1908.

Ying-Jie, Z.; Xian-Luo, H.; Wei-Wei, W., Poly(vinylpyrrolidone): a new reductant for preparation of tellurium nanorods, nanowires, and tubes from TeO2. *Nanotechnology* **2006,** *17* (3), 645.

Qian, H.-S.; Yu, S.-H.; Gong, J.-Y.; Luo, L.-B.; Fei, L.-f., High-Quality Luminescent Tellurium Nanowires of Several Nanometers in Diameter and High Aspect Ratio Synthesized by a Poly (Vinyl Pyrrolidone)-Assisted Hydrothermal Process. *Langmuir* **2006,** *22* (8), 3830-3835.

Zhang, G.; Fang, H.; Yang, H.; Jauregui, L. A.; Chen, Y. P.; Wu, Y., Design Principle of Telluride-Based Nanowire Heterostructures for Potential Thermoelectric Applications. *Nano Letters* **2012b,** *12* (7), 3627-3633.

Zhang, G.; Kirk, B.; Jauregui, L. A.; Yang, H.; Xu, X.; Chen, Y. P.; Wu, Y., Rational Synthesis of Ultrathin n-Type Bi2Te3 Nanowires with Enhanced Thermoelectric Properties. *Nano Letters* **2011b,** *12* (1), 56-60.

Yang, H.; Bahk, J.-H.; Day, T.; Mohammed, A. M. S.; Min, B.; Snyder, G. J.; Shakouri, A.; Wu, Y., Composition Modulation of Ag2Te Nanowires for Tunable Electrical and Thermal Properties. *Nano Letters* **2014,** *14* (9), 5398-5404.

Fang, H.; Feng, T.; Yang, H.; Ruan, X.; Wu, Y., Synthesis and Thermoelectric Properties of Compositional-Modulated Lead Telluride–Bismuth Telluride Nanowire Heterostructures. *Nano Letters* **2013,** *13* (5), 2058-2063.

Fang, H.; Yang, H.; Wu, Y., Thermoelectric Properties of Silver Telluride–Bismuth Telluride Nanowire Heterostructure Synthesized by Site-Selective Conversion. *Chemistry of Materials* **2014a,** *26* (10), 3322-3327.

Yim, W. M.; Rosi, F. D., Compound tellurides and their alloys for Peltier cooling – review. *Solid-State Electron.* **1972,** *15* (10), 1121.

Carle, M.; Pierrat, P.; Lahallegravier, C.; Scherrer, S.; Scherrer, H., Transport-properties of n-type Bi2(Te1-xSex)3 single-crystal solid-solutions (x less than or equal to 0.05). *Journal of Physics and Chemistry of Solids* **1995,** *56* (2), 201-209.

Yamashita, O.; Tomiyoshi, S.; Makita, K., Bismuth telluride compounds with high thermoelectric figures of merit. *Journal of Applied Physics* **2003,** *93* (1), 368-374.

Mehta, R. J.; Zhang, Y. L.; Karthik, C.; Singh, B.; Siegel, R. W.; Borca-Tasciuc, T.; Ramanath, G., A new class of doped nanobulk high-figure-of-merit thermoelectrics by scalable bottom-up assembly. *Nature Materials* **2012,** *11* (3), 233-240.

Drabble, J. R.; Goodman, C. H. L., Chemical bonding in bismuth telluride. *Journal of Physics and Chemistry of Solids* **1958,** *5* (1-2), 142-144.

Mishra, S. K.; Satpathy, S.; Jepsen, O., Electronic structure and thermoelectric properties of bismuth telluride and bismuth selenide. *Journal of Physics: Condensed Matter* **1997,** *9* (2), 461.

Liu, W.-S.; Zhang, Q.; Lan, Y.; Chen, S.; Yan, X.; Zhang, Q.; Wang, H.; Wang, D.; Chen, G.; Ren, Z., Thermoelectric Property Studies on Cu-Doped n-type CuxBi2Te2.7Se0.3 Nanocomposites. *Advanced Energy Materials* **2011,** *1* (4), 577-587.

Schultz, J. M.; McHugh, J. P.; Tiller, W. A., Effects of Heavy Deformation and Annealing on the Electrical Properties of Bi2Te3. *Journal of Applied Physics* **1962,** *33* (8), 2443-2450.

Hyun, D.-B.; Hwang, J.-S.; Shim, J.-D.; Oh, T., Thermoelectric properties of (Bi0.25Sb0.75)2Te3 alloys fabricated by hot-pressing method. *Journal of Materials Science* **2001,** *36* (5), 1285-1291.

Jiang, J.; Chen, L.; Bai, S.; Yao, Q.; Wang, Q., Fabrication and thermoelectric performance of textured n-type Bi2(Te,Se)3 by spark plasma sintering. *Materials Science and Engineering: B* **2005,** *117* (3), 334-338.

Scanlon, D. O.; King, P. D. C.; Singh, R. P.; de la Torre, A.; Walker, S. M.; Balakrishnan, G.; Baumberger, F.; Catlow, C. R. A., Controlling Bulk Conductivity in Topological Insulators: Key Role of Anti-Site Defects. *Advanced Materials* **2012,** *24* (16), 2154-2158.

Starý, Z.; Horák, J.; Stordeur, M.; Stölzer, M., Antisite defects in Sb2−xBixTe3 mixed crystals. *Journal of Physics and Chemistry of Solids* **1988,** *49* (1), 29-34.

Jia, S.; Ji, H.; Climent-Pascual, E.; Fuccillo, M. K.; Charles, M. E.; Xiong, J.; Ong, N. P.; Cava, R. J., Low-carrier-concentration crystals of the topological insulator Bi2Te2Se. *Physical Review B* **2011,** *84* (23), 235206.

Fuccillo, M. K.; Jia, S.; Charles, M. E.; Cava, R. J., Thermoelectric Properties of Bi2Te2Se Compensated by Native Defects and Sn Doping. *Journal of Electronic Materials* **2013,** *42* (6), 1246-1253.

Jia, S.; Beidenkopf, H.; Drozdov, I.; Fuccillo, M. K.; Seo, J.; Xiong, J.; Ong, N. P.; Yazdani, A.; Cava, R. J., Defects and high bulk resistivities in the Bi-rich tetradymite topological insulator Bi2+xTe2-xSe. *Physical Review B* **2012,** *86* (16), 165119.

Mavrokefalos, A.; Moore, A. L.; Pettes, M. T.; Shi, L.; Wang, W.; Li, X., Thermoelectric and structural characterizations of individual electrodeposited bismuth telluride nanowires. *Journal of Applied Physics* **2009,** *105* (10), 104318.

Chen, C. L.; Chen, Y. Y.; Lin, S. J.; Ho, J. C.; Lee, P. C.; Chen, C. D.; Harutyunyan, S. R., Fabrication and Characterization of Electrodeposited Bismuth Telluride Films and Nanowires. *Journal of Physical Chemistry C* **2010,** *114* (8), 3385-3389.

Shin, H. S.; Jeon, S. G.; Yu, J.; Kim, Y. S.; Park, H. M.; Song, J. Y., Twin-driven thermoelectric figure-of-merit enhancement of Bi2Te3 nanowires. *Nanoscale* **2014,** *6* (11), 6158-6165.

Neuberger, M. *The BiTe-BiSe system data sheet, Airforce Mater. Res. Lab*, **1966**.

Son, J. S.; Choi, M. K.; Han, M.-K.; Park, K.; Kim, J.-Y.; Lim, S. J.; Oh, M.; Kuk, Y.; Park, C.; Kim, S.-J.; Hyeon, T., n-Type Nanostructured Thermoelectric Materials Prepared from Chemically Synthesized Ultrathin Bi2Te3 Nanoplates. *Nano Letters* **2012,** *12* (2), 640-647.

Zhao, Y.; Dyck, J. S.; Hernandez, B. M.; Burda, C., Improving Thermoelectric Properties of Chemically Synthesized Bi2Te3-Based Nanocrystals by Annealing. *The Journal of Physical Chemistry C* **2010,** *114* (26), 11607-11613.

Soni, A.; Yanyuan, Z.; Ligen, Y.; Aik, M. K. K.; Dresselhaus, M. S.; Xiong, Q., Enhanced Thermoelectric Properties of Solution Grown Bi2Te3–xSex Nanoplatelet Composites. *Nano Letters* **2012,** *12* (3), 1203-1209.

Yoo, B. Y.; Huang, C. K.; Lim, J. R.; Herman, J.; Ryan, M. A.; Fleurial, J. P.; Myung, N. V., Electrochemically deposited thermoelectric n-type Bi2Te3 thin films. *Electrochimica Acta* **2005,** *50* (22), 4371-4377.

Kim, D.-H.; Byon, E.; Lee, G.-H.; Cho, S., Effect of deposition temperature on the structural and thermoelectric properties of bismuth telluride thin films grown by co-sputtering. *Thin Solid Films* **2006,** *510* (1–2), 148-153.

Boulouz, A.; Giani, A.; Pascal-Delannoy, F.; Boulouz, M.; Foucaran, A.; Boyer, A., Preparation and characterization of MOCVD bismuth telluride thin films. *Journal of Crystal Growth* **1998,** *194* (3–4), 336-341.

Yang, J. Y.; Aizawa, T.; Yamamoto, A.; Ohta, T., Thermoelectric properties of n-type (Bi2Se3)x(Bi2Te3)1−x prepared by bulk mechanical alloying and hot pressing. *Journal of Alloys and Compounds* **2000,** *312* (1–2), 326-330.

Li, D.; Qin, X. Y.; Liu, Y. F.; Wang, N. N.; Song, C. J.; Sun, R. R., Improved thermoelectric properties for solution grown Bi2Te3-xSex nanoplatelet composites. *RSC Advances* **2013,** *3* (8), 2632-2638.

Kim, C.; Kim, D. H.; Kim, H.; Chung, J. S., Significant Enhancement in the Thermoelectric Performance of a Bismuth Telluride Nanocompound through Brief Fabrication Procedures. *ACS Applied Materials & Interfaces* **2012,** *4* (6), 2949-2954.

Stavila, V.; Robinson, D. B.; Hekmaty, M. A.; Nishimoto, R.; Medlin, D. L.; Zhu, S.; Tritt, T. M.; Sharma, P. A., Wet-Chemical Synthesis and Consolidation of Stoichiometric Bismuth Telluride Nanoparticles for Improving the Thermoelectric Figure-of-Merit. *ACS Applied Materials & Interfaces* **2013,** *5* (14), 6678-6686.

Kim, K. T.; Choi, S. Y.; Shin, E. H.; Moon, K. S.; Koo, H. Y.; Lee, G.-G.; Ha, G. H., The influence of CNTs on the thermoelectric properties of a CNT/Bi2Te3 composite. *Carbon* **2013,** *52* (0), 541-549.

Ibáñez, M.; Zamani, R.; Gorsse, S.; Fan, J.; Ortega, S.; Cadavid, D.; Morante, J. R.; Arbiol, J.; Cabot, A., Core–Shell Nanoparticles As Building Blocks for the Bottom-Up Production of Functional Nanocomposites: PbTe–PbS Thermoelectric Properties. *ACS Nano* **2013,** *7* (3), 2573-2586.

Dong, J.; Liu, W.; Li, H.; Su, X.; Tang, X.; Uher, C., In situ synthesis and thermoelectric properties of PbTe-graphene nanocomposites by utilizing a facile and novel wet chemical method. *Journal of Materials Chemistry A* **2013,** *1* (40), 12503-12511.

Finefrock, S. W.; Zhang, G.; Bahk, J.-H.; Fang, H.; Yang, H.; Shakouri, A.; Wu, Y., Structure and Thermoelectric Properties of Spark Plasma Sintered Ultrathin PbTe Nanowires. *Nano Letters* **2014b,** *14* (6), 3466-3473.

Jin, R.; Chen, G.; Pei, J.; Sun, J.; Wang, Q., Controllable synthesis and thermoelectric transport properties of binary-phased PbTe/PbSe nanocrystals. *CrystEngComm* **2012,** *14* (13), 4461-4466.

Scheele, M.; Oeschler, N.; Veremchuk, I.; Peters, S.-O.; Littig, A.; Kornowski, A.; Klinke, C.; Weller, H., Thermoelectric Properties of Lead Chalcogenide Core–Shell Nanostructures. *ACS Nano* **2011,** *5* (11), 8541-8551.

Zhang, Y.; Wang, H.; Kräemer, S.; Shi, Y.; Zhang, F.; Snedaker, M.; Ding, K.; Moskovits, M.; Snyder, G. J.; Stucky, G. D., Surfactant-Free Synthesis of Bi2Te3−Te Micro−Nano Heterostructure with Enhanced Thermoelectric Figure of Merit. *ACS Nano* **2011a,** *5* (4), 3158-3165.

Min, Y.; Roh, J. W.; Yang, H.; Park, M.; Kim, S. I.; Hwang, S.; Lee, S. M.; Lee, K. H.; Jeong, U., Surfactant-Free Scalable Synthesis of Bi2Te3 and Bi2Se3 Nanoflakes and Enhanced Thermoelectric Properties of Their Nanocomposites. *Advanced Materials* **2013,** *25* (10), 1425-1429.

Zhang, Y.; Snedaker, M. L.; Birkel, C. S.; Mubeen, S.; Ji, X.; Shi, Y.; Liu, D.; Liu, X.; Moskovits, M.; Stucky, G. D., Silver-Based Intermetallic Heterostructures in Sb2Te3 Thick Films with Enhanced Thermoelectric Power Factors. *Nano Letters* **2012a,** *12* (2), 1075-1080.

Kulbachinskii, V. A.; Kytin, V. G.; Popov, M. Y.; Buga, S. G.; Stepanov, P. B.; Blank, V. D., Composites of Bi2–xSbxTe3 nanocrystals and fullerene molecules for thermoelectricity. *Journal of Solid State Chemistry* **2012,** *193* (0), 64-70.

Zhou, W.; Zhu, J.; Li, D.; Hng, H. H.; Boey, F. Y. C.; Ma, J.; Zhang, H.; Yan, Q., Binary-Phased Nanoparticles for Enhanced Thermoelectric Properties. *Advanced Materials* **2009,** *21* (31), 3196-3200.

Hochbaum, A. I.; Chen, R.; Delgado, R. D.; Liang, W.; Garnett, E. C.; Najarian, M.; Majumdar, A.; Yang, P., Enhanced thermoelectric performance of rough silicon nanowires. *Nature* **2008,** *451* (7175), 163-167.

Zhou, J.; Jin, C.; Seol, J. H.; Li, X.; Shi, L., Thermoelectric properties of individual electrodeposited bismuth telluride nanowires. *Applied Physics Letters* **2005,** *87* (13), 133109.

Wu, Y.; Xiang, J.; Yang, C.; Lu, W.; Lieber, C. M., Single-crystal metallic nanowires and metal/semiconductor nanowire heterostructures. *Nature* **2004,** *430* (6995), 61-65.

Gudiksen, M. S.; Lauhon, L. J.; Wang, J.; Smith, D. C.; Lieber, C. M., Growth of nanowire superlattice structures for nanoscale photonics and electronics. *Nature* **2002,** *415* (6872), 617-620.

Wang, W.; Lu, X.; Zhang, T.; Zhang, G.; Jiang, W.; Li, X., Bi2Te3/Te Multiple Heterostructure Nanowire Arrays Formed by Confined Precipitation. *Journal of the American Chemical Society* **2007,** *129* (21), 6702-6703.

Wang, W.; Zhang, G.; Li, X., Manipulating Growth of Thermoelectric Bi2Te3/Sb Multilayered Nanowire Arrays. *The Journal of Physical Chemistry C* **2008,** *112* (39), 15190-15194.

Ouyang, L.; Maher, K. N.; Yu, C. L.; McCarty, J.; Park, H., Catalyst-Assisted Solution−Liquid−Solid Synthesis of CdS/CdSe Nanorod Heterostructures. *Journal of the American Chemical Society* **2006,** *129* (1), 133-138.

Jin, C.; Zhang, G.; Qian, T.; Li, X.; Yao, Z., Large-Area Sb2Te3 Nanowire Arrays. *The Journal of Physical Chemistry B* **2005,** *109* (4), 1430-1432.

Lu, W.; Ding, Y.; Chen, Y.; Wang, Z. L.; Fang, J., Bismuth Telluride Hexagonal Nanoplatelets and Their Two-Step Epitaxial Growth. *Journal of the American Chemical Society* **2005a,** *127* (28), 10112-10116.

Wang, W.; Goebl, J.; He, L.; Aloni, S.; Hu, Y.; Zhen, L.; Yin, Y., Epitaxial Growth of Shape-Controlled Bi2Te3−Te Heterogeneous Nanostructures. *Journal of the American Chemical Society* **2010,** *132* (48), 17316-17324.

Tang, Z.; Wang, Y.; Sun, K.; Kotov, N. A., Spontaneous Transformation of Stabilizer-Depleted Binary Semiconductor Nanoparticles into Selenium and Tellurium Nanowires. *Advanced Materials* **2005,** *17* (3), 358-363.

Zhang, B.; Hou, W.; Ye, X.; Fu, S.; Xie, Y., 1D Tellurium Nanostructures: Photothermally Assisted Morphology-Controlled Synthesis and Applications in Preparing Functional Nanoscale Materials. *Advanced Functional Materials* **2007,** *17* (3), 486-492.

Habas, S. E.; Lee, H.; Radmilovic, V.; Somorjai, G. A.; Yang, P., Shaping binary metal nanocrystals through epitaxial seeded growth. *Nature Materials* **2007,** *6* (9), 692-697.

Sadtler, B.; Demchenko, D. O.; Zheng, H.; Hughes, S. M.; Merkle, M. G.; Dahmen, U.; Wang, L.-W.; Alivisatos, A. P., Selective Facet Reactivity during Cation Exchange in Cadmium Sulfide Nanorods. *Journal of the American Chemical Society* **2009,** *131* (14), 5285-5293.

Saunders, A. E.; Popov, I.; Banin, U., Synthesis of Hybrid CdS−Au Colloidal Nanostructures. *The Journal of Physical Chemistry B* **2006,** *110* (50), 25421-25429.

Xu, T.; Cao, Z.-Q.; Fang, J.-H., Quantization rules for low dimensional quantum dots. *Chinese Physics B* **2008,** *17* (12), 4378.

Robinson, R. D.; Sadtler, B.; Demchenko, D. O.; Erdonmez, C. K.; Wang, L.-W.; Alivisatos, A. P., Spontaneous Superlattice Formation in Nanorods Through Partial Cation Exchange. *Science* **2007,** *317* (5836), 355-358.

See, K. C.; Feser, J. P.; Chen, C. E.; Majumdar, A.; Urban, J. J.; Segalman, R. A., Water-Processable Polymer−Nanocrystal Hybrids for Thermoelectrics. *Nano Letters* **2010,** *10* (11), 4664-4667.

Haneman, D., Photoelectric emission and work functions of InSb, GaAs, Bi2Te3 and germanium. *Journal of Physics and Chemistry Solids* **1959,** *11* (3–4), 205-214.

Vashaee, D.; Shakouri, A., Improved Thermoelectric Power Factor in Metal-Based Superlattices. *Physical Review Letters* **2004,** *92* (10), 106103.

Lo, S.-H.; He, J.; Biswas, K.; Kanatzidis, M. G.; Dravid, V. P., Phonon Scattering and Thermal Conductivity in p-Type Nanostructured PbTe-BaTe Bulk Thermoelectric Materials. *Advanced Functional Materials* **2012,** *22* (24), 5175-5184.

Girard, S. N.; Chasapis, T. C.; He, J.; Zhou, X.; Hatzikraniotis, E.; Uher, C.; Paraskevopoulos, K. M.; Dravid, V. P.; Kanatzidis, M. G., PbTe-PbSnS2 thermoelectric composites: low lattice thermal conductivity from large microstructures. *Energy & Environmental Science* **2012,** *5* (9), 8716-8725.

Oh, T.-S., Thermoelectric Characteristics of p-Type (Bi,Sb)2Te3/(Pb,Sn)Te Functional Gradient Materials with Variation of the Segment Ratio. *Journal of Electronic Materials* **2009,** *38* (7), 1041-1047.

Su, T.; Zhu, P.; Ma, H.; Ren, G.; Chen, L.; Guo, W.; Iami, Y.; Jia, X., Electrical transport and high thermoelectric properties of PbTe doped with Bi2Te3 prepared by HPHT. *Solid State Communications* **2006,** *138* (12), 580-584.

Zhu, P.; Imai, Y.; Isoda, Y.; Shinohara, Y.; Jia, X.; Zou, G., Composition-Dependent Thermoelectric Properties of (PbTe)100_x(Bi2Te3-Sb2Te3)x (0.1<x<5). *Materials Transactions* **2005,** *46* (4), 761-764.

Hirai, T.; Takeda, Y.; Kurata, K., The pseudo-binary V2VI3-IV·VI compounds systems, Bi2Te3-PbTe, Bi2Te3-SnTe, Sb2Te3-PbTe, Sb2Te3-SnTe and Bi2Se3-SnSe. *Journal of the Less Common Metals* **1967,** *13* (3), 352-356.

LaLonde, A. D.; Pei, Y.; Snyder, G. J., Reevaluation of PbTe1-xIx as high performance n-type thermoelectric material. *Energy & Environmental Science* **2011b,** *4* (6), 2090-2096.

Green, M.; Lee, M. J.; Miles, R. E., Work function of lead telluride. *Surface Science* **1968,** *12* (2), 403-404.

Snyder, G. J.; Toberer, E. S., Complex thermoelectric materials. *Nature Materials* **2008,** *7* (2), 105-114.

Mahan, G. D.; Bartkowiak, M., Wiedemann–Franz law at boundaries. *Applied Physics Letters* **1999,** *74* (7), 953-954.

Maciá, E., Do quasicrystals follow Wiedemann–Franz's law? *Applied Physics Letters* **2002,** *81* (1), 88-90.

Toprak, M. S.; Stiewe, C.; Platzek, D.; Williams, S.; Bertini, L.; Müller, E.; Gatti, C.; Zhang, Y.; Rowe, M.; Muhammed, M., The Impact of Nanostructuring on the Thermal Conductivity of Thermoelectric CoSb3. *Advanced Functional Materials* **2004,** *14* (12), 1189-1196.

Bauer, T. H., A general analytical approach toward the thermal conductivity of porous media. *International Journal of Heat and Mass Transfer* **1993,** *36* (17), 4181-4191.

Raghavan, S.; Wang, H.; Dinwiddie, R. B.; Porter, W. D.; Mayo, M. J., The effect of grain size, porosity and yttria content on the thermal conductivity of nanocrystalline zirconia. *Scripta Materialia* **1998,** *39* (8), 1119-1125.

Yadav, G. G.; Zhang, G.; Qiu, B.; Susoreny, J. A.; Ruan, X.; Wu, Y., Self-templated synthesis and thermal conductivity investigation for ultrathin perovskite oxide nanowires. *Nanoscale* **2011,** *3* (10), 4078-4081.

Evans, W.; Prasher, R.; Fish, J.; Meakin, P.; Phelan, P.; Keblinski, P., Effect of aggregation and interfacial thermal resistance on thermal conductivity of nanocomposites and colloidal nanofluids. *International Journal of Heat and Mass Transfer* **2008,** *51* (5–6), 1431-1438.

Jay, A., Grain boundary Kapitza resistance and grain-arrangement induced anisotropy in the thermal conductivity of polycrystalline niobium at low temperatures. *Journal of Physics D: Applied Physics* **2006,** *39* (20), 4472.

Yang, H.-S.; Bai, G. R.; Thompson, L. J.; Eastman, J. A., Interfacial thermal resistance in nanocrystalline yttria-stabilized zirconia. *Acta Materialia* **2002,** *50* (9), 2309-2317.

Bruggeman, D. A. G., Berechnung verschiedener physikalischer Konstanten von heterogenen Substanzen. I. Dielektrizitätskonstanten und Leitfähigkeiten der Mischkörper aus isotropen Substanzen. *Annalen der Physik* **1935,** *416* (7), 636-664.

Hamilton, R. L.; Crosser, O. K., Thermal Conductivity of Heterogeneous Two-Component Systems. *Industrial & Engineering Chemistry Fundamentals* **1962,** *1* (3), 187-191.

Jiajun, W.; Xiao-Su, Y., Effects of interfacial thermal barrier resistance and particle shape and size on the thermal conductivity of AlN/PI composites. *Composites Science and Technology* **2004,** *64* (10–11), 1623-1628.

Nan, C.-W.; Birringer, R.; Clarke, D. R.; Gleiter, H., Effective thermal conductivity of particulate composites with interfacial thermal resistance. *Journal of Applied Physics* **1997,** *81* (10), 6692-6699.

Goldsmid, H. J., The Thermal Conductivity of Bismuth Telluride. *Proceedings of the Physical Society. Section B* **1956,** *69* (2), 203.

Völklein, F.; Kessler, E., Thermal Conductivity and Thermoelectric Figure of Merit of Thin Antimony Films. *physica status solidi (b)* **1990,** *158* (2), 521-529.

Satterthwaite, C. B.; Ure, R. W., Electrical and Thermal Properties of Bi2Te3. *Physical Review* **1957,** *108* (5), 1164-1170.

Huang, B.-L.; Kaviany, M., Ab initio and molecular dynamics predictions for electron and phonon transport in bismuth telluride. *Physical Review B* **2008,** *77* (12), 125209.

Qiu, B.; Bao, H.; Zhang, G.; Wu, Y.; Ruan, X., Molecular dynamics simulations of lattice thermal conductivity and spectral phonon mean free path of PbTe: Bulk and nanostructures. *Computational Materials Science* **2012,** *53* (1), 278-285.

Lauhon, L. J.; Gudiksen, M. S.; Wang, D.; Lieber, C. M., Epitaxial core-shell and core-multishell nanowire heterostructures. *Nature* **2002,** *420* (6911), 57-61.

Lu, W.; Xiang, J.; Timko, B. P.; Wu, Y.; Lieber, C. M., One-dimensional hole gas in germanium/silicon nanowire heterostructures. *Proceedings of the National Academy of Sciences of the United States of America* **2005b,** *102* (29), 10046-10051.

Xiang, J.; Lu, W.; Hu, Y.; Wu, Y.; Yan, H.; Lieber, C. M., Ge/Si nanowire heterostructures as high-performance field-effect transistors. *Nature* **2006,** *441* (7092), 489-493.

Li, Y.; Xiang, J.; Qian, F.; Gradečak, S.; Wu, Y.; Yan, H.; Blom, D. A.; Lieber, C. M., Dopant-Free GaN/AlN/AlGaN Radial Nanowire Heterostructures as High Electron Mobility Transistors. *Nano Letters* **2006,** *6* (7), 1468-1473.

Borgström, M. T.; Zwiller, V.; Müller, E.; Imamoglu, A., Optically Bright Quantum Dots in Single Nanowires. *Nano Letters* **2005,** *5* (7), 1439-1443.

Panev, N.; Persson, A. I.; Sköld, N.; Samuelson, L., Sharp exciton emission from single InAs quantum dots in GaAs nanowires. *Applied Physics Letters* **2003,** *83* (11), 2238-2240.

Tian, B.; Zheng, X.; Kempa, T. J.; Fang, Y.; Yu, N.; Yu, G.; Huang, J.; Lieber, C. M., Coaxial silicon nanowires as solar cells and nanoelectronic power sources. *Nature* **2007,** *449* (7164), 885-889.

Dong, Y.; Tian, B.; Kempa, T. J.; Lieber, C. M., Coaxial Group III−Nitride Nanowire Photovoltaics. *Nano Letters* **2009,** *9* (5), 2183-2187.

Garnett, E.; Yang, P., Light Trapping in Silicon Nanowire Solar Cells. *Nano Letters* **2010,** *10* (3), 1082-1087.

Barth, S.; Hernandez-Ramirez, F.; Holmes, J. D.; Romano-Rodriguez, A., Synthesis and applications of one-dimensional semiconductors. *Progress in Materials Science* **2010,** *55* (6), 563-627.

Buck, M. R.; Schaak, R. E., Emerging Strategies for the Total Synthesis of Inorganic Nanostructures. *Angewandte Chemie International Edition* **2013,** *52* (24), 6154-6178.

Liu, J.-W.; Xu, J.; Liang, H.-W.; Wang, K.; Yu, S.-H., Macroscale Ordered Ultrathin Telluride Nanowire Films, and Tellurium/Telluride Hetero-Nanowire Films. *Angewandte Chemie International Edition* **2012,** *51* (30), 7420-7425.

Liu, J.-W.; Huang, W.-R.; Gong, M.; Zhang, M.; Wang, J.-L.; Zheng, J.; Yu, S.-H., Flexible Electronics: Ultrathin Hetero-Nanowire-Based Flexible Electronics with Tunable Conductivity (Adv. Mater. 41/2013). *Advanced Materials* **2013,** *25* (41), 5909-5909.

Hong, X.; Yin, Z.; Fan, Z.; Tay, Y.-Y.; Chen, J.; Du, Y.; Xue, C.; Chen, H.; Zhang, H., Periodic AuAg-Ag2S Heterostructured Nanowires. *Small* **2014,** *10* (3), 479-482.

Zhang, L.; Ai, Z.; Jia, F.; Liu, L.; Hu, X.; Yu, J. C., Controlled Hydrothermal Synthesis and Growth Mechanism of Various Nanostructured Films of Copper and Silver Tellurides. *Chemistry – A European Journal* **2006,** *12* (15), 4185-4190.

Qin, A.; Fang, Y.; Tao, P.; Zhang, J.; Su, C., Silver Telluride Nanotubes Prepared by the Hydrothermal Method. *Inorganic Chemistry* **2007,** *46* (18), 7403-7409.

Li, F.; Hu, C.; Xiong, Y.; Wan, B.; Yan, W.; Zhang, M., Phase-Transition-Dependent Conductivity and Thermoelectric Property of Silver Telluride Nanowires. *The Journal of Physical Chemistry C* **2008,** *112* (41), 16130-16133.

Jiang, L.; Zhu, Y.-J., A General Solvothermal Route to the Synthesis of CoTe, Ag2Te/Ag, and CdTe Nanostructures with Varied Morphologies. *European Journal of Inorganic Chemistry* **2010,** *2010* (8), 1238-1243.

Xiao, F.; Chen, G.; Wang, Q.; Wang, L.; Pei, J.; Zhou, N., Simple synthesis of ultra-long Ag2Te nanowires through solvothermal co-reduction method. *Journal of Solid State Chemistry* **2010,** *183* (10), 2382-2388.

Chen, R.; Xu, D.; Guo, G.; Gui, L., Silver telluride nanowires prepared by dc electrodeposition in porous anodic alumina templates. *Journal of Materials Chemistry* **2002,** *12* (8), 2435-2438.

Pei, J.; Chen, G.; Jia, D.; Yu, Y.; Sun, J.; Xu, H.; Qiu, Z., Crooked Ag2Te nanowires with rough surfaces: facile microwave-assisted solution synthesis, growth mechanism, and electrical performances. *New Journal of Chemistry* **2014,** *38* (1), 59-62.

Mu, L.; Wan, J.; Ma, D.; Zhang, R.; Yu, W.; Qian, Y., A Room Temperature Self-sacrificing Template Route to Ag2Te Fibers. *Chemistry Letters* **2005,** *34* (1), 52-53.

Moon, G. D.; Ko, S.; Xia, Y.; Jeong, U., Chemical Transformations in Ultrathin Chalcogenide Nanowires. *ACS Nano* **2010,** *4* (4), 2307-2319.

Ayyappan, S.; Subbanna, G. N.; Gopalan, R. S.; Rao, C. N. R., Nanoparticles of nickel and silver produced by the polyol reduction of the metal salts intercalated in montmorillonite. *Solid State Ionics* **1996,** *84* (3–4), 271-281.

Jeong, U.; Xia, Y., Photonic Crystals with Thermally Switchable Stop Bands Fabricated from Se@Ag2Se Spherical Colloids. *Angewandte Chemie International Edition* **2005,** *44* (20), 3099-3103.

Zhang, S.-n.; Jiang, G.-y.; Zhu, T.-j.; Zhao, X.-b.; Yang, S.-h., Doping effect on thermoelectric properties of nonstoichiometric AgSbTe2 compounds. *International Journal of Minerals, Metallurgy, and Materials* **2011c,** *18* (3), 352-356.

Drymiotis, F.; Day, T. W.; Brown, D. R.; Heinz, N. A.; Jeffrey Snyder, G., Enhanced thermoelectric performance in the very low thermal conductivity Ag2Se0.5Te0.5. *Applied Physics Letters* **2013,** *103* (14), 143906.

Cadavid, D.; Ibanez, M.; Shavel, A.; Dura, O. J.; Lopez de la Torre, M. A.; Cabot, A., Organic ligand displacement by metal salts to enhance nanoparticle functionality: thermoelectric properties of Ag2Te. *Journal of Materials Chemistry A* **2013,** *1* (15), 4864-4870.

Pei, Y.; Heinz, N. A.; Snyder, G. J., Alloying to increase the band gap for improving thermoelectric properties of Ag2Te. *Journal of Materials Chemistry* **2011a,** *21* (45), 18256-18260.

Gottlieb, G. E.; Kane, W. M.; Walsh, J. F.; Wood, C., Electrical properties of Ag2Te. *Journal of Physics and Chemistry of Solids* **1960,** *15* (1–2), 183-185.

Das, V. D.; Karunakaran, D., Semiconducting behavior of Ag2Te thin films and the dependence of band gap on thickness. *Journal of Applied Physics* **1983,** *54* (9), 5252-5255.

Androulakis, J.; Todorov, I.; Chung, D.-Y.; Ballikaya, S.; Wang, G.; Uher, C.; Kanatzidis, M., Thermoelectric enhancement in PbTe with K or Na codoping from tuning the interaction of the light- and heavy-hole valence bands. *Physical Review B* **2010,** *82* (11), 115209.

Taylor, P. F.; Wood, C., Thermoelectric Properties of Ag2Te. *Journal of Applied Physics* **1961,** *32* (1), 1-3.

Fujikane, M.; Kurosaki, K.; Muta, H.; Yamanaka, S., Thermoelectric properties of α- and β-Ag2Te. *Journal of Alloys and Compounds* **2005a,** *393* (1–2), 299-301.

Capps, J.; Drymiotis, F.; Lindsey, S.; Tritt, T. M., Significant enhancement of the dimensionless thermoelectric figure of merit of the binary Ag2Te. *Philosophical Magazine Letters* **2010,** *90* (9), 677-681.

Fujikane, M.; Kurosaki, K.; Muta, H.; Yamanaka, S., Electrical properties of α- and β-Ag2Te. *Journal of Alloys and Compounds* **2005b,** *387* (1–2), 297-299.

Seto, J. Y. W., The electrical properties of polycrystalline silicon films. *Journal of Applied Physics* **1975,** *46* (12), 5247-5254.

Paul, B.; V, A. K.; Banerji, P., Embedded Ag-rich nanodots in PbTe: Enhancement of thermoelectric properties through energy filtering of the carriers. *Journal of Applied Physics* **2010,** *108* (6), 064322.

Johnsen, S.; He, J.; Androulakis, J.; Dravid, V. P.; Todorov, I.; Chung, D. Y.; Kanatzidis, M. G., Nanostructures Boost the Thermoelectric Performance of PbS. *Journal of the American Chemical Society* **2011,** *133* (10), 3460-3470.

Fang, H.; Luo, Z.; Yang, H.; Wu, Y., The Effects of the Size and the Doping Concentration on the Power Factor of n-type Lead Telluride Nanocrystals for Thermoelectric Energy Conversion. *Nano Letters* **2014b,** *14* (3), 1153-1157.

Talapin, D. V.; Lee, J.-S.; Kovalenko, M. V.; Shevchenko, E. V., Prospects of Colloidal Nanocrystals for Electronic and Optoelectronic Applications. *Chemical Reviews* **2009,** *110* (1), 389-458.

Zhang, G.; Finefrock, S.; Liang, D.; Yadav, G. G.; Yang, H.; Fang, H.; Wu, Y., Semiconductor nanostructure-based photovoltaic solar cells. *Nanoscale* **2011d,** *3* (6), 2430-2443.

Klimov, V. I.; Ivanov, S. A.; Nanda, J.; Achermann, M.; Bezel, I.; McGuire, J. A.; Piryatinski, A., Single-exciton optical gain in semiconductor nanocrystals. *Nature* **2007,** *447* (7143), 441-446.

Liang, D.; Yang, H.; Finefrock, S. W.; Wu, Y., Flexible Nanocrystal-Coated Glass Fibers for High-Performance Thermoelectric Energy Harvesting. *Nano Letters* **2012,** *12* (4), 2140-2145.

Poon, S. J.; Limtragool, K., Nanostructure model of thermal conductivity for high thermoelectric performance. *Journal of Applied Physics* **2011,** *110* (11), 114306.

Cahill, D. G.; Ford, W. K.; Goodson, K. E.; Mahan, G. D.; Majumdar, A.; Maris, H. J.; Merlin, R.; Phillpot, S. R., Nanoscale thermal transport. *Journal of Applied Physics* **2003,** *93* (2), 793-818.

Norris, D. J.; Efros, A. L.; Erwin, S. C., Doped Nanocrystals. *Science* **2008,** *319* (5871), 1776-1779.

Dalpian, G. M.; Chelikowsky, J. R., Self-Purification in Semiconductor Nanocrystals. *Physical Review Letters* **2006,** *96* (22), 226802.

Du, M. H.; Erwin, S. C.; Efros, A. L.; Norris, D. J., Comment on "Self-Purification in Semiconductor Nanocrystals". *Physical Review Letters* **2008,** *100* (17), 179702.

Yin, Y.; Alivisatos, A. P., Colloidal nanocrystal synthesis and the organic-inorganic interface. *Nature* **2005,** *437* (7059), 664-670.

Peng, Z. A.; Peng, X., Mechanisms of the Shape Evolution of CdSe Nanocrystals. *Journal of the American Chemical Society* **2001,** *123* (7), 1389-1395.

Pei, Y.; LaLonde, A.; Iwanaga, S.; Snyder, G. J., High thermoelectric figure of merit in heavy hole dominated PbTe. *Energy & Environmental Science* **2011b,** *4* (6), 2085-2089.

VITA

VITA

Haiyu Fang received her BS degree from the Department of Materials Science and Engineering at University of Science and Technology of China in 2010. He is currently a graduate student, working as a research assistant in Prof. Yue Wu's group, in School of Chemical Engineering at Purdue University. His research includes synthesizing advanced nanostructured materials with efficient solution phase reaction as well as optimizing the thermoelectric performance of nanocomposites and thin films made from solution synthesized nanoparticles. The following is a list of publications that he has published.

PUBLICATIONS

PUBLICATIONS

Fang, H.; Bahk, J. –H.; Mohammed, A.; Gao, T.; Shakouri, A.; Wu, Y. "An Investigation of Se Doping Effect on Thermoelectric Property of Bi_2Te_3 Nanocomposite" In preparation, 2014.

Finefrock, S. W.; Yang, H.; **Fang, H.**; Wu, Y. "Thermoelectric Properties of Solution Synthesized Nanostructured Materials" *Annu. Rev. Chem. Biomol. Eng.*, Invited Review, 2014.

Fang, H.; Yang, H.; Wu, Y. "Thermoelectric Properties of Silver Telluride-Bismuth Telluride Nanowire Heterostructure Synthesized by Site-Selective Conversion" *Chem. Mater.*, 2014, 26, 3322

Finefrock, S. W.; **Fang, H. (*equal contribution*)**; Yang, H.; Darsono, H.; Wu, Y. "Large-scale solution-phase synthesis of Bi_2Te_3 and PbTe nanowires using Te nanowire templates" *Nanoscale*, 2014, 6, 7872

Fang, H.; Luo, Z.; Yang H.; Wu, Y. "Effect of Size and Doping concentration on the Power Factor of n-type Lead Telluride Nanocrystals for Thermoelectric Energy Conversion" *Nano Lett.,* 2014, 14, 1153

Fang, H.; Wu, Y. "Telluride Nanowire and Nanowire Heterostructure-Based Thermoelectric Energy Harvesting" *J. Mater. Chem. A,* 2014, 2, 6004

Finefrock, S. W.; Zhang, G.; Bahk, J. H.; **Fang, H.**; Yang, H.; Shakouri, A.; Wu, Y. "Structure and Thermoelectric Properties of Spark Plasma Sintered Ultrathin PbTe Nanowires" *Nano Lett.*, 2014, 14, 3466

Finefrock, S. W.; Wan, Y.; Ferguson, J. B.; Ward, J. V.; **Fang, H.**; Pfluger, J. E.; Dudis, D. S.; Ruan, X.; Wu, Y. "Measurement of Thermal Conductivity of PbTe Nanocrystal Coated Glass Fibers by the 3ω Method" *Nano Lett.*, 2013, 13, 5006

Fang, H.; Feng, T.; Yang, H.; Ruan, X.; Wu, Y. "Synthesis and Thermoelectric Properties of Compositional-Modulated Lead Telluride–Bismuth Telluride Nanowire Heterostructures" *Nano Lett.,* 2013, 13, 2058

Zhang, G.; **Fang, H. (*equal contribution*)**; Yang, H.; Jauregui, L. A.; Chen, P. Y.; Wu, Y. "Design Principle of Telluride-Based Nanowire Heterostructures for Potential Thermoelectric Applications" *Nano Lett.,* 2012, 12, 3627

Zhang, G.; Finefrock, S.; Liang, D.; Yadav, G.; Yang, H.; Fang, H.; Wu, Y. "Semiconductor Nanostructure-Based Photovoltaic Solar Cells" *Nanoscale*, 2011, 3, 2430

Yao, H.; **Fang, H.**; Wang, X.; Yu, S. "Hierarchical Assembly of Micro-/Nano- Building Blocks: Bio-Inspired Rigid Structural Functional Materials" *Chem. Soc. Rev.* 2011,40, 3764

Yao, H.; **Fang, H.**; Tan, Z.; Wu, L.; Yu, S. "Bio-Inspired, Strong, Transparent and Functional Layered Organic-Inorganic Hybrid Films" *Angew. Chem. Int. Ed.* 2010, 49, 2140

Yao,H.; Tan, Z.; **Fang, H.**; Yu, S. "Artificial Nacre-like Bionanocomposite Films from the Self-Assembly of Chitosan–Montmorillonite Hybrid Building Blocks" *Angew. Chem. Int. Ed.* 2010, 49, 10127

Yao, H.; Wu, L.; Cui, C.; **Fang, H.**; Yu, S. "Direct Fabrication of Photoconductive Patterns on LBL Assembled Graphene Oxide/PDDA/Titania Hybrid Films by Photothermal and Photocatalytic Reduction" *J. Mater. Chem.* 2010, 20, 5190